

UNCLASSIFIED

SECURITY CLASSIFICATION OF THIS PAGE

REPORT DOCUMENTATION PAGE

Form Approved
OMB No. 0704-0188

| | | | | | |
|--|-------|---|---|---|----------------------------|
| 1a. REPORT SECURITY CLASSIFICATION UNCLASSIFIED | | | 1b. RESTRICTIVE MARKINGS AFOSR-TR 97-0385 | | |
| 2a. SECURITY CLASSIFICATION AUTHORITY | | | 3. DISTRIBUTION / AVAILABILITY OF REPORT Approved for public release: distribution unlimited | | |
| 2b. DECLASSIFICATION / DOWNGRADING SCHEDULE | | | | | |
| 4. PERFORMING ORGANIZATION REPORT NUMBER(S) OSU-WOS-97-1 | | | 5. MONITORING ORGANIZATION REPORT NUMBER(S) F49620-94-1-0107DEF | | |
| 6a. NAME OF PERFORMING ORGANIZATION Ohio State University | | 6b. OFFICE SYMBOL (if applicable) | 7a. NAME OF MONITORING ORGANIZATION Air Force Office of Scientific Research | | |
| 6c. ADDRESS (City, State, and ZIP Code) 477 Watts Hall-2041 College Road Columbus, OH 43210 | | | 7b. ADDRESS (City, State, and ZIP Code) Department of the Air Force-Bolling A.F.B. Washington, D.C. 20332 | | |
| 8a. NAME OF FUNDING / SPONSORING ORGANIZATION AFOSR | | 8b. OFFICE SYMBOL (if applicable) NA | 9. PROCUREMENT INSTRUMENT IDENTIFICATION NUMBER | | |
| 8c. ADDRESS (City, State, and ZIP Code) Department of the Air Force-Bolling A.F.B. Washington, D.C. 20332 | | | 10. SOURCE OF FUNDING NUMBERS | | |
| | | | PROGRAM ELEMENT NO. | PROJECT NO. | TASK NO. |
| | | | | | WORK UNIT ACCESSION NO. |
| 11. TITLE (Include Security Classification) Synergistic Toughening of MoSi ₂ | | | 19971003 064 | | |
| 12. PERSONAL AUTHOR(S) W.O. Soboyejo, G-Y. Lu and F-Ye | | | | | |
| 13a. TYPE OF REPORT Final | | 13b. TIME COVERED FROM 1/1/94 TO 6/30/97 | | 14. DATE OF REPORT (Year, Month, Day) 97/06/30 | |
| 15. PAGE COUNT 105 | | | | | |
| 16. SUPPLEMENTARY NOTATION | | | | | |
| 17. COSATI CODES | | | 18. SUBJECT TERMS (Continue on reverse if necessary and identify by block number) | | |
| FIELD | GROUP | SUB-GROUP | Molybdenum disilicide, intermetallics, transformation toughening, fracture, toughness | | |
| | | | | | |
| | | | | | |
| 19. ABSTRACT (Continue on reverse if necessary and identify by block number) | | | | | |
| <p>Research during the past three years has focused on the study of individual transformation toughening and crack bridging mechanisms in molybdenum disilicide composites reinforced with partially stabilized zirconia and thermodynamically compatible Nb, Mo and W phases. The primary objective in the initial studies was to study the fatigue and fracture mechanisms in model composite systems prior to a focused research effort aimed at developing synergistically toughened hybrid composites reinforced with zirconia particles and ductile/brittle bridging reinforcements. The hybrid composites were described as synergistically toughened composites due to anticipated interactions between crack bridging and stress-induced phase transformations. Such interactions may promote higher toughening levels than those expected from the sum of the individual toughening components, i.e., bridging and transformation toughening.</p> <p>(continue on reverse)</p> | | | | | |
| 20. DISTRIBUTION / AVAILABILITY OF ABSTRACT <input checked="" type="checkbox"/> UNCLASSIFIED/UNLIMITED <input type="checkbox"/> SAME AS RPT. <input type="checkbox"/> DTIC USERS | | | 21. ABSTRACT SECURITY CLASSIFICATION UNCLASSIFIED | | |
| 22a. NAME OF RESPONSIBLE INDIVIDUAL DR SPENCER WU | | | 22b. TELEPHONE (Include Area Code) 202-767-4989 | | 22c. OFFICE SYMBOL |

UNCLASSIFIED

Room-temperature fatigue and fracture behavior was studied in the transformation toughened and ductile phase toughened composites during the first and second year of the project. Following the careful study of room-temperature fatigue and fracture mechanisms, elevated-temperature fatigue and fracture mechanisms were studied in MoSi_2 , zirconia particle-reinforced MoSi_2 , and silicon carbide whisker-reinforced MoSi_2 in the third year of the project. Crack-tip scanning and transmission electron microscopy studies were performed to determine the failure mechanisms at elevated-temperature. The studies showed clearly that elevated-temperature crack growth in MoSi_2 and MoSi_2 composite occurs by a combination of mechanical fatigue and creep crack growth (viscous flow of amorphous glass phase and microvoid nucleation) mechanisms. A model was also proposed for creep-fatigue crack growth at elevated-temperature. Relatively fast elevated-temperature cyclic crack growth rates were thus explained by considering the combined effects of creep and fatigue crack growth components.

Finally, the possible synergistic interactions between crack bridging and transformation toughening were studied during the fourth year of the program. Synergistic toughening was studied in model MoSi_2 composites reinforced with 2 mole % yttria partially stabilized zirconia particles, and Nb layers. Synergistic toughening was shown to occur in these composites due to additional transformations that were induced as a result of higher interfacial stresses. However, the overall level of transformation toughening was limited. Nevertheless, a synergistically toughened MoSi_2 composite with a toughness of $\sim 20.5 \pm 1.0 \text{ MPa}\sqrt{\text{m}}$ was produced by hybrid reinforcement with Nb layers and 2 mole % yttria-stabilized zirconia particles.

TABLE OF CONTENTS

| | |
|---|----------|
| Program Summary | (iii) |
| Program Personal | (iv) |
| List of Figures | (v) |
| List of Tables | (vii) |
| 1. Effect of Reinforcement Morphology on the Fatigue and Fracture on MoSi ₂ /Nb Composites | (1) |
| 1.1. Introduction | (1) |
| 1.2. Experimental Procedure | (2) |
| 1.2.1 Materials | (2) |
| 1.2.2 Bend Strength | (5) |
| 1.2.3 Fracture Toughness | (5) |
| 1.2.4 Resistance Curve Behavior | (6) |
| 1.2.5 Fatigue Crack Growth | (6) |
| 1.3. Bend Strength | (7) |
| 1.4. Fracture | (9) |
| 1.4.1 Particulate-Reinforced Composites | (9) |
| 1.4.2 Fiber-Reinforced Composites | (11) |
| 1.4.3 Laminated Composites | (18) |
| 1.5. Resistance Curve Behavior | (20) |
| 1.6. Fatigue Crack Growth | (23) |
| 1.6.1 Particulate-Reinforced Composites | (23) |
| 1.6.2 Fiber-Reinforced Composites | (23) |
| 1.6.3 Laminated Composites | (27) |
| 1.7. Conclusions | (28) |
| 2. Transformation Toughening in MoSi ₂ | (30) |
| 2.1. Introduction | (30) |
| 2.2. Micromechanical Modeling | (31) |
| 2.2.1 Transformation Toughening | (31) |
| 2.2.2 Residual Stress Analysis | (34) |
| 2.3. Experimental Procedures | (40) |
| 2.3.1 Material and Microstructures | (40) |
| 2.3.2 X-ray Diffraction Analysis | (42) |
| 2.3.3 Laser Raman Spectroscopy | (43) |
| 2.3.4 Mechanical Properties | (44) |
| 2.3.5 Transformation Zone Analysis | (45) |

| | |
|---|-------|
| 2.4. RESULTS AND DISCUSSION | (46) |
| 2.4.1 Microstructure | (46) |
| 2.4.2 X-ray Calibration | (49) |
| 2.4.3 Laser Raman Spectroscopy | (53) |
| 2.4.4 Residual Stress | (53) |
| 2.4.5 Compression Strength | (60) |
| 2.4.6 Fracture and Toughening Mechanisms | (62) |
| 2.5. CONCLUSIONS | (68) |
| 3. Synergistic Toughening | (69) |
| 3.1. Introduction | (69) |
| 3.2. Experimental | (69) |
| 3.2.1 Material | (69) |
| 3.2.2 Fracture Toughness | (70) |
| 3.2.3 Fatigue Crack Growth | (73) |
| 3.3. Conclusions | (74) |
| 4. Fatigue and Fracture of Brittle-Reinforced Molybdenum Disilicide Composites at Elevated Temperature | (80) |
| 4.1. Introduction | (80) |
| 4.2. Experimental Procedure | (81) |
| 4.2.1 Material Processing and Microstructures | (81) |
| 4.2.2 Cyclic Fatigue Crack Growth at 1200°C | (81) |
| 4.2.3 Fracture Toughness at 1200°C | (82) |
| 4.3. Results And Discussion | (83) |
| 4.3.1 Microstructures and Substructure | (83) |
| 4.3.2 Fracture Toughness | (83) |
| 4.3.3 Fatigue crack Growth Mechanism | (88) |
| 4.3.4 Fracture Modes | (88) |
| 4.3.5 Crack-Tip Deformation Mechanisms | (96) |
| 4.4. Conclusions | (96) |
| 5. References | (100) |
| 6. Publications | (103) |
| 7. Presentations | (104) |
| 8. Honors | (105) |

PROGRAM SUMMARY

Research during the past three years has focused on the study of individual transformation toughening and crack bridging mechanisms in molybdenum disilicide composites reinforced with partially stabilized zirconia and thermodynamically compatible Nb, Mo and W phases. The primary objective in the initial studies was to study the fatigue and fracture mechanisms in model composite systems prior to a focused research effort aimed at developing synergistically toughened hybrid composites reinforced with zirconia particles and ductile/brittle bridging reinforcements. The hybrid composites were described as synergistically toughened composites due to anticipated interactions between crack bridging and stress-induced phase transformations. Such interactions may promote higher toughening levels than those expected from the sum of the individual toughening components, i.e., bridging and transformation toughening.

Room-temperature fatigue and fracture behavior was studied in the transformation toughened and ductile phase toughened composites during the first and second year of the project. Following the careful study of room-temperature fatigue and fracture mechanisms, elevated-temperature fatigue and fracture mechanisms were studied in MoSi_2 , zirconia particle-reinforced MoSi_2 , and silicon carbide whisker-reinforced MoSi_2 in the third year of the project. Crack-tip scanning and transmission electron microscopy studies were performed to determine the failure mechanisms at elevated-temperature. The studies showed clearly that elevated-temperature crack growth in MoSi_2 and MoSi_2 composite occurs by a combination of mechanical fatigue and creep crack growth (viscous flow of amorphous glass phase and microvoid nucleation) mechanisms. A model was also proposed for creep-fatigue crack growth at elevated-temperature. Relatively fast elevated-temperature cyclic crack growth rates were thus explained by considering the combined effects of creep and fatigue crack growth components.

Finally, the possible synergistic interactions between crack bridging and transformation toughening were studied during the fourth year of the program. Synergistic toughening was studied in model MoSi_2 composites reinforced with 2 mole % yttria partially stabilized zirconia particles, and Nb layers. Synergistic toughening was shown to occur in these composites due to additional transformations that were induced as a result of higher interfacial stresses. However, the overall level of transformation toughening was limited. Nevertheless, a synergistically toughened MoSi_2 composite with a toughness of $\sim 20.5 \pm 1.0 \text{ MPa}\sqrt{\text{m}}$ was produced by hybrid reinforcement with Nb layers and 2 mole % yttria-stabilized zirconia particles

PROGRAM PERSONNEL

Dr. W.O. Soboyejo, Associate Professor

Mr. Fan Ye, Graduate Research Assistant

Mr. Ned Bahtishi, Graduate Research Associate

Dr. Gui-Ying Lu, Research Associate

Dr. You-Lin Li, Research Associate

Dr. Long-Ching Chen, Research Associate

Ms. Sarah Reeve, Undergraduate Research Assitant

LIST OF FIGURE CAPTIONS

- Fig. 1.1 Microstructure of Particulate MoSi₂/Nb Composites:
(a) Particle Distribution, (b) Particle/matrix interface
- Fig. 1.2 Microstructures of Nb Fiber-Reinforced MoSi₂/Nb Composites
(a,b) 250 μm Diameter Fiber Composite (c,d) 750 μm Diameter Fiber Composite
- Fig. 1.3 Microstructures of Laminated MoSi₂/Nb Composites.
(a) Laminate Distribution (b) Laminate/Matrix Interface
- Fig. 1.4 Effects of Temperature on Bend Strength
- Fig. 1.5 Comparisons of Fracture Toughness Data
- Fig. 1.6 Fracture Surface Morphologies of MoSi₂ + 20 vol.% Nb Composite.
(a) Mixed Cleavage + intergranular Fracture in Matrix,
(b) Matrix Fracture,
(c) Dimples Resulting From Decohesion and Pull Out of Particles From Matrix,
(d) Cleavage Across Nb Particle
- Fig. 1.7 Typical Fracture Modes in Fiber-Reinforced Composites Under Monotonic Loading
(a, b) 250 μm Nb Fiber Composite
(c, d) 750 μm Nb Fiber Composite
- Fig. 1.8 Crack Interactions With Composite Microstructure In Double Notched Specimens.
(a) 250 μm Diameter Fiber Composite (b) 750 μm Diameter Fiber Composite
- Fig. 1.9 Typical Deformation and Fracture Modes in Laminated Composites.
(a) Ductile Dimpled Fracture of Nb Layer
(b) Extensive Plastic Stretching of Nb Layers
(c) Multiple Matrix Cracking
(d) Crack Bridging and Crack-Tip Blunting By Nb Layers.
- Fig. 1.10 Resistance Curve Behavior (Experimental vs. Prediction)
- Fig. 1.11 Schematic Illustration of Crack Growth Sequence in a 250 μm Nb Fiber-Reinforced MoSi₂ Composite.
- Fig. 1.12 Summary of Fatigue Crack Growth Rate Data
- Fig. 1.13 Interactions of Fatigue Cracks With Microstructure
(a) Compression Pre-Crack in Monolithic MoSi₂
(b) Deflection in Particulate-Reinforced Composites
(c) Bridging and Blunting in Fiber Composite
(d) Multiple Cracks in Laminated Composite
- Fig. 1.14 Typical Fatigue Fracture Modes
(a,b) Particulate-Reinforced Composites
(c) 250 μm Diameter Fiber Composite
(d) 750 μm Diameter Fiber
(e,f) 200 μm Laminated Composite
- Fig. 2.1 Schematic Illustration of Transformation Toughening
- Fig. 2.2 Schematic Illustration of Random Particle Configuration in Particulate Reinforced Composites

- Fig. 2.3 Optical Micrographs of MoSi₂/PSZ Composites
(a) TZ-0Y, (b) TZ-2Y, (c) TZ-4Y and (d) TZ-6Y
- Fig. 2.4 Transmission Electron Micrographs of MoSi₂/PSZ Composites
(a) TZ-0Y, (b) TZ-0Y, (c) TZ-2Y and (d) TZ-4Y
- Fig. 2.5 X-ray Diffraction Calibration
(a) Plot of Intensity Ratio versus Volume Fraction of Monoclinic Phase
(b) Comparison of Predicted and Actual Monoclinic Phase Content
- Fig. 2.6 Plots of Effective Coefficient versus
(a) Particle Volume Fraction (b) Number of Particles
- Fig. 2.7 Summary of Predicted Residual Stresses
(a) Plot of Normalized Residual Stress versus Particle Volume Fraction
(b) Effect of Yttria Content on Residual Stresses
- Fig. 2.8 Typical Fracture Surface Morphologies of Fracture Toughness Specimens
(a) TZ-0Y and (b) TZ-2Y (c) TZ-4Y (d) TZ-6Y
- Fig. 2.9 Volume Fraction of Monoclinic Zirconia as a Function of Distance from the Crack-Tip in MoSi₂ + 20 vol. % TZ-2Y Composite
- Fig. 2.10 Typical Optical Interference Micrograph Showing Fringes Near the Fracture Surfaces of TZ-2Y Composite
- Fig. 3.1 Microstructure of Synergistically Toughened Composite MoSi₂+20 Vol. % Nb₁+20 Vol. % TZ-2Y_p:
- Fig. 3.2 Fracture Toughness Data
- Fig. 3.3 Typical Fracture Mode of Fracture Toughness Specimens
- Fig. 3.4 Typical Raman Spectrum Observed
(a) Deformed (b) Undeformed
- Fig. 3.5 Volume Percentage of Monoclinic Phase
- Fig. 3.6 Summary of Fatigue Crack Growth Rate Data
- Fig. 3.7 Typical Fatigue Fracture Mode
- Fig. 4.1 SEM Photomicrographs Showing Microstructural Features of MoSi₂ and Brittle Reinforced MoSi₂ Composites
(a) MoSi₂; (b) MoSi₂ + 20 vol.% SiC_w, and (c) MoSi₂ + 20 vol.%TZ-2Y
- Fig. 4.2 TEM Photomicrographs of MoSi₂ and Brittle Reinforced MoSi₂ Composites
(a) MoSi₂ (1200 °C/0.5h/AC); (b) MoSi₂ (1200 °C/0.5h/AC);
(c) MoSi₂ + 20 vol.% SiC_w (1200 °C/0.5h/AC);
(d) MoSi₂ + 20 vol.% SiC_w (1200 °C/0.5h/AC);
(e) MoSi₂ + 20 vol.%TZ-2Y (1200 °C/0.5h/AC);
(f) MoSi₂ + 20 vol.%TZ-2Y (1200 °C/0.5h/AC)
- Fig. 4.3 Plot of Fatigue Crack Growth Rate vs Stress Intensity Factor Range
- Fig. 4.4 Typical Fracture Surface Morphologies of MoSi₂ and Brittle Reinforced MoSi₂ Composites at Room Temperature
(a) MoSi₂; (b) MoSi₂ + 20 vol.% SiC_w, and (c) MoSi₂ + 20 vol.%TZ-2Y

- Fig. 4.5 Typical Fracture Surface Morphologies of MoSi_2 and Brittle Reinforced MoSi_2 Composites at 1200 °C
(a) MoSi_2 ; (b) $\text{MoSi}_2 + 20 \text{ vol.}\% \text{ SiC}_w$, and (c) $\text{MoSi}_2 + 20 \text{ vol.}\% \text{ TZ-2Y}$
- Fig. 4.6 Fatigue Fracture Surface Morphologies of MoSi_2 and Brittle Reinforced MoSi_2 Composites at 1200 °C
(a) MoSi_2 ; (b) $\text{MoSi}_2 + 20 \text{ vol.}\% \text{ SiC}_w$, and (c) $\text{MoSi}_2 + 20 \text{ vol.}\% \text{ TZ-2Y}$
- Fig. 4.7 Typical TEM Images of Crack Tip Regions of MoSi_2 and Brittle Reinforced MoSi_2 Composites Deformed Under Cyclic Loading at 1200 °C
(a) MoSi_2 ; (b) MoSi_2 ; (c) $\text{MoSi}_2 + 20 \text{ vol.}\% \text{ SiC}_w$; (d) $\text{MoSi}_2 + 20 \text{ vol.}\% \text{ SiC}_w$;
(e) $\text{MoSi}_2 + 20 \text{ vol.}\% \text{ TZ-2Y}$, and (f) $\text{MoSi}_2 + 20 \text{ vol.}\% \text{ TZ-2Y}$;

LIST OF TABLE CAPTIONS

- Table 1.1 Summary of Crack Bridging Parameters
- Table 1.2 Summary of Crack-Tip Blunting Parameters
- Table 1.3 Summary of Overall Toughening Parameters
- Table 2.1 Summary of Mechanical and Thermal Properties
- Table 2.2 Summary of Mechanical Properties
- Table 3.1 Summary of Fracture Toughness Data
- Table 3.2 Fatigue Crack Growth Parameters at 1200 °C (n=10 Hz, R=0.2)

Chapter 1

Effects of Reinforcement Morphology on the Fatigue and Fracture Behavior of MoSi₂/Nb Composites

1.1. Introduction

The concept of ductile phase toughening of brittle materials is not new. It was proposed originally by Kristic [1-3] as a means of increasing the energy dissipation (by plastic stretching of ductile materials) in brittle materials. Since the original work by Kristic [1-3], there have been considerable efforts to improve the fracture toughness of brittle materials by the incorporation of ductile phases [4-26]. Unfortunately, however, very few of these studies have considered the role of reinforcement morphology [22-25] and cyclic loading [12,19,24,25] on the damage tolerance of ductile phase toughened composites. Our current understanding of the effects of reinforcement geometry is therefore insufficient for the design of composites with the desired combinations of fracture toughness and fatigue resistance.

Furthermore, the current interest in the development of hypersonic vehicles has stimulated the need for light weight, high temperature, structural materials that can be used at elevated temperatures up to 1300°C [12,13]. MoSi₂ has been considered for potential structural use in this regime due to its attractive combinations of elevated temperature strength and oxidation resistance [12,13]. However, the potential application of MoSi₂ has been limited by its low fracture toughness and fatigue crack growth resistance [19-25]. There is therefore a need for toughening strategies to improve the room-temperature damage tolerance of MoSi₂.

Ductile phase toughening strategies that result in MoSi₂ composites with comparable fracture toughness to structural Al alloys (18-24 MPa√m) are identified in this report by careful evaluation of fracture modes in composites reinforced with ductile particles, fibers and laminates. However, these composites are also shown to have low initiation fracture toughness, in spite of their significant levels of crack growth resistance. The toughening mechanisms (crack-tip blunting, crack bridging and crack deflection) are modeled and the micromechanisms of crack growth are elucidated for crack growth under monotonic and cyclic loading.

The effects of particulate, fiber and laminate reinforcement geometries on the fatigue crack growth and fracture behavior of model MoSi₂/Nb composites are discussed in this chapter of the report. This chapter is divided into seven sections. The material processing and composite microstructures are discussed in Section 1.2. This is followed by Section 1.3 in which the experimental techniques are described. Elevated-temperature bend strength data are then presented in Section 1.4 prior to a discussion on fracture and toughening mechanisms in Section 1.5. Micromechanisms of fatigue crack growth are elucidated in Section 1.6 before summarizing

the salient conclusions arising from this study in Section 1.7. The report highlights the potential importance of reinforcement morphology in the development of composites with improved fatigue and fracture resistance.

1.2. Experimental Procedure

1.2.1 Materials

The particulate-reinforced composites were prepared from MoSi₂ and Nb powders. The -325 mesh (approx. 44 μm average diameter) MoSi₂ powder employed in this study was procured from Cerac, Milwaukee, WI. Nb reinforcements were procured from Nuclear Metals, Henderson, NV. These included: powders with an average diameter of 200 μm and 750 μm ; and foils with an average thickness of 200 μm . Particulate-reinforced composites were fabricated by hot isostatic pressing (HIPing) under 207 MPa pressure, at 1700°C for 4h, after dry phase blending for 24h. This resulted in a uniform distribution of Nb particles in the matrix of MoSi₂ (Figure 1.1a). A layered interfacial region was also observed in the particulate-reinforced MoSi₂ (Figure 1.1b). This was shown via energy dispersive X-ray analysis to consist of layers of Mo₅Si₃ and (Mo, Nb)₅Si₃ [9]. The MoSi₂ matrix also contained some silica particles (light regions in Figure 1.2b) and 1-2% porosity (dark regions in Figure 1.2b).

The microstructures of the Nb fiber reinforced composite are presented in Figures 1.2a-1.2d. The fiber-reinforced composites were produced by manual lay-up of 250 or 750 μm diameter fibers on a Nb wire frame, prior to HIPing in an evacuated (10^{-4} Pa) Nb can at 1400°C. The Nb wires were procured from G&S Titanium, Wooster, OH. The cross-section microstructural features of the fiber-reinforced composites were similar to those of the particulate-reinforced composites. However, the layered interfacial reaction zones were much smaller in the fiber-reinforced composites, presumably as a result of the lower consolidation temperature. Similarly, the laminated composites had relatively small reaction zones after HIPing in evacuated (10^{-4} Pa) Nb cans at 1400°C (Figures 1.3a and 1.3b). The laminated composites were produced by the consolidation of MoSi₂ powder and 200 μm thick Nb foils that were arranged manually prior to HIPing. All the composites, which contained 20 volume percent Nb reinforcement, were fabricated at McDonnell Douglas, St. Louis, MO.

Some effort was made to study the fatigue crack growth behavior in pure Nb produced from powder that was supplied by Nuclear Metals, Henderson, NV. The powders were poured into Nb cans, and electron beam welded after evacuating the cans. The cans were then HIPed under the same processing conditions that were used for the processing of the fiber-reinforced and laminated composites. The same processing conditions were used for the fabrication of the

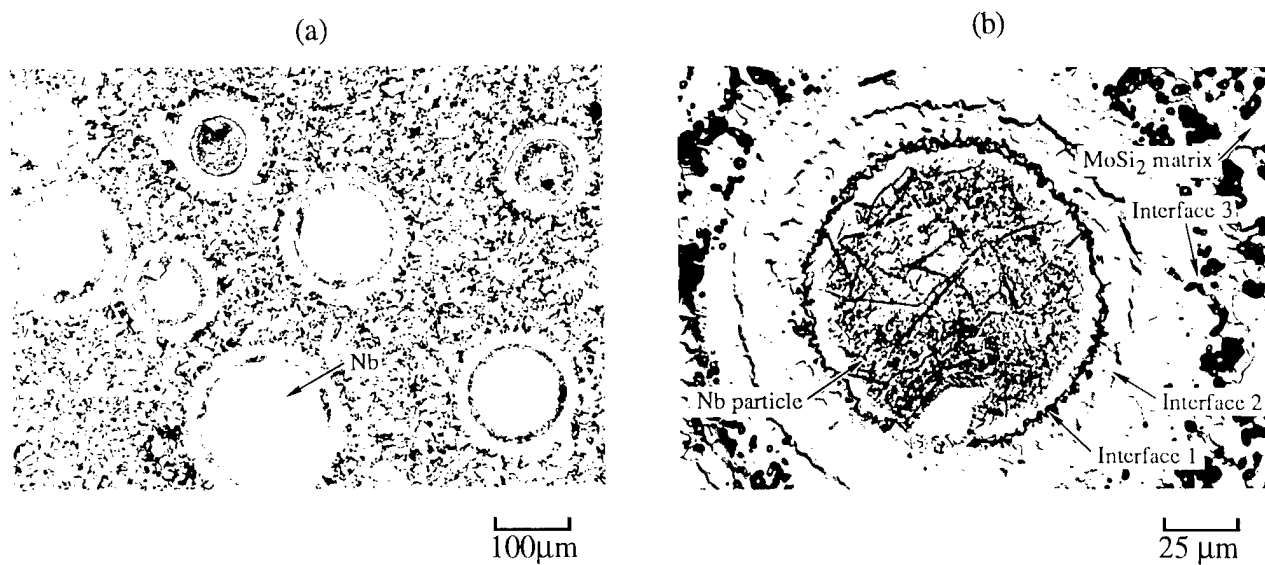


Figure 1.1 Microstructure of Particulate MoSi_2/Nb Composites:
(a) Particle Distribution, (b) Particle/matrix interface

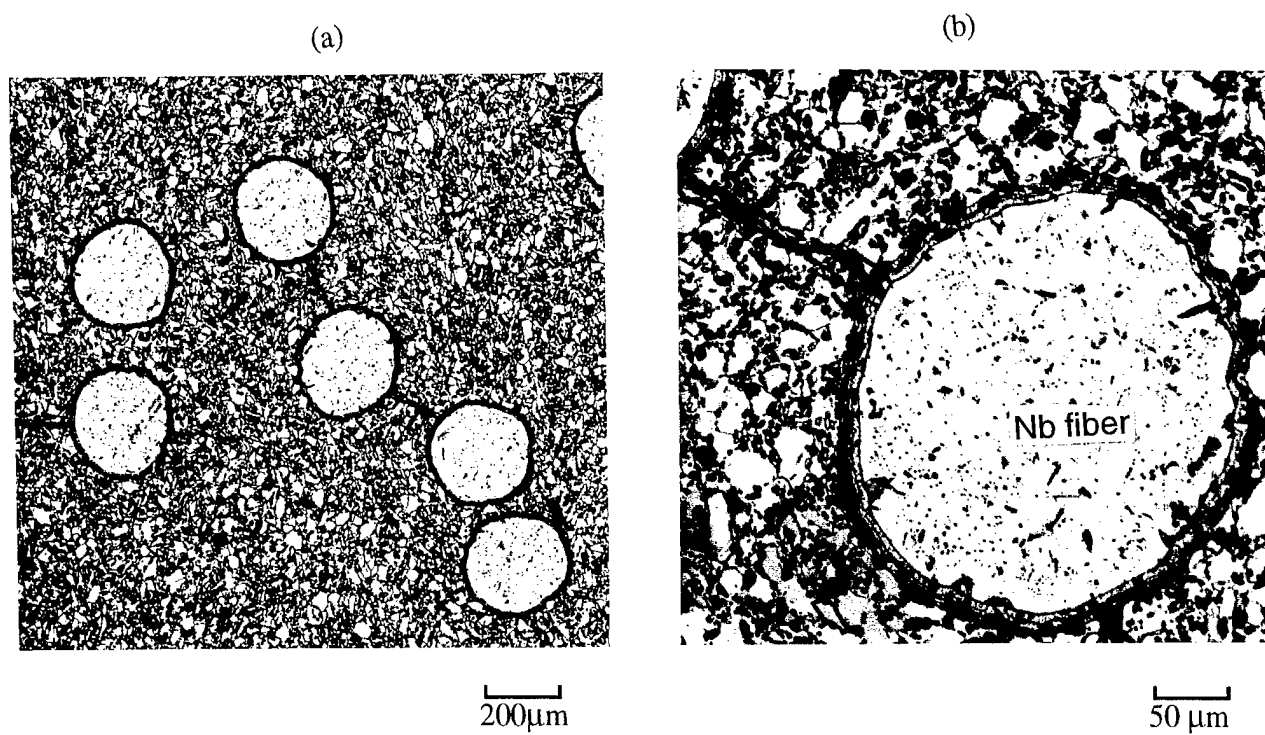


Figure 1.2 Microstructures of Nb Fiber-Reinforced MoSi_2/Nb Composites
(a,b) 250 μm Diameter Fiber Composite

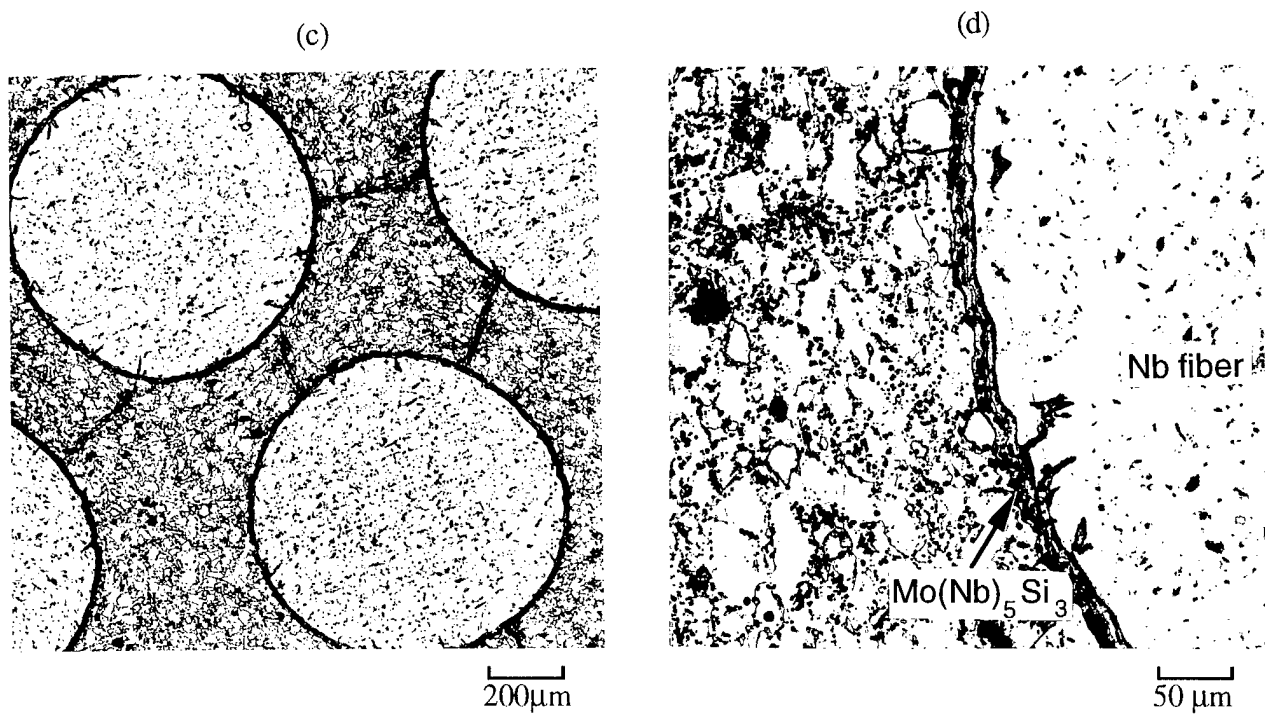


Figure 1.2 (c,d) 750 μm Diameter Fiber Composite

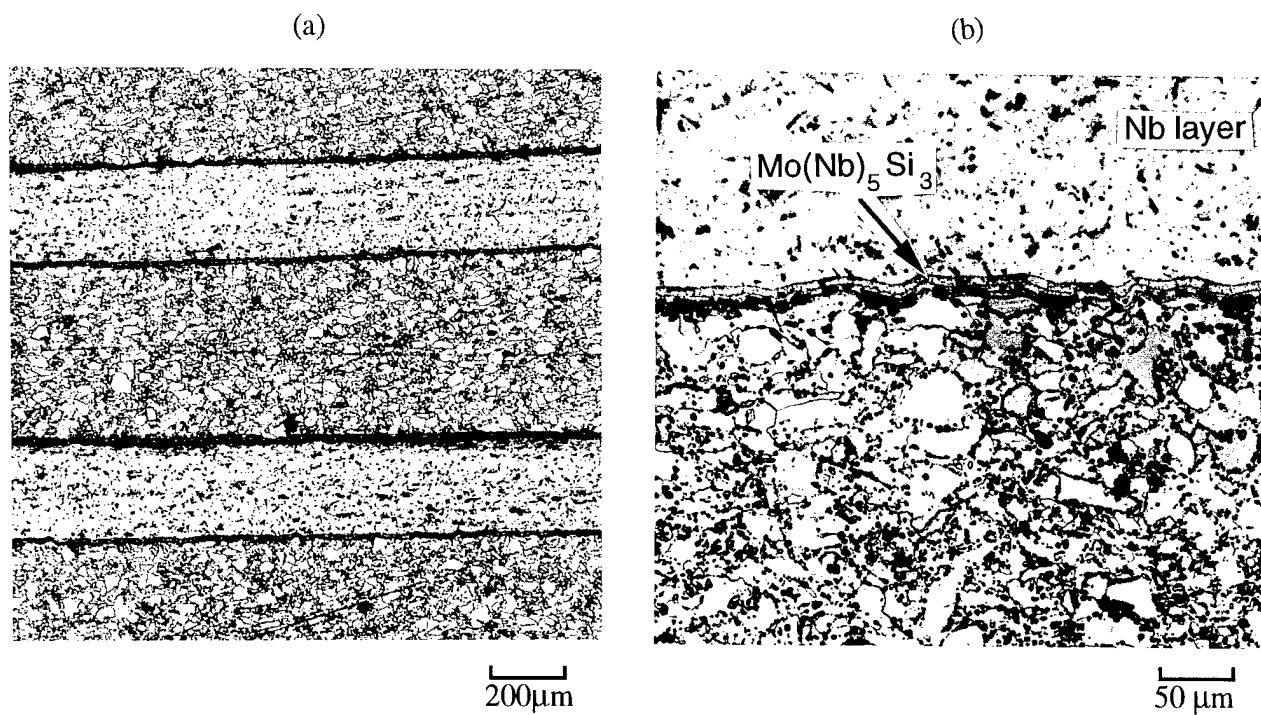


Figure 1.3 Microstructures of Laminated MoSi_2/Nb Composites.
(a) Laminate Distribution (b) Laminate/Matrix Interface

composites and monolithic materials in an attempt to ensure that the interstitial contents of the fiber/laminated MoSi₂/Nb composites were similar to those in the monolithic Nb compacts.

1.2.2. Bend Strength

Duplicate four-point (pure) bend tests were carried out in vacuum (10^{-6} Pa) on 25.4 mm long composite bars with square cross sections (0.25 mm x 0.25 mm). The tests were conducted in vacuum (approx. 10^{-6} Pa) due to the susceptibility of Nb reinforcements to interstitial pick-up and oxidation at elevated temperature. The bend tests were carried out at temperatures between 1000 and 1500°C. The specimens were soaked at temperature for 30 minutes prior to bend testing at a maximum flexural strain rate of approx. $5 \times 10^{-4} \text{ s}^{-1}$. The initial flexural loading axis was parallel to the fiber direction, and the specimens were mounted on SiC rollers. Ultimate tensile strengths were determined from the peak loads when the specimens did not exhibit any plastic strains prior to failure. However, 0.2% offset yield stresses were estimated for the specimens that exhibited at least 0.2% plastic strain prior to failure.

1.2.3. Fracture Toughness

Duplicate fracture toughness tests were performed on single edge notched (SEN) specimens. The tests on single edge notched (SEN) bend specimens were conducted on specimens with relatively deep notches (notch-to-width ratios of 0.4). The specimens were pre-cracked under far-field compression loading [12] prior to monotonic loading to failure under four-point (pure) bending. A ramp rate corresponding to a stress intensity factor increase rate of $1 \text{ MPa}\sqrt{\text{m}} \text{ s}^{-1}$ was employed during monotonic loading. The failure modes in the fractured specimens were then examined using scanning electron microscopy (SEM) techniques.

Similar fracture toughness tests were performed on the double edge notched (DEN) bend specimens with two nominally identical notches. The two notches were located (on the same side) between the two inner rollers within the four-point bend loading configuration that was used. The notches, therefore, experienced the same nominal stress intensity factors during monotonic loading. However, in most cases, small local differences between the notches, induced as a result of machining and local microstructural features, typically resulted in the onset of unstable crack growth/catastrophic failure from one of the two notches. Such failure normally occurred after an initial phase of almost identical stable crack growth from both notches. The remaining unfractured halves of the double notched bend specimens therefore retained useful information on the extent stable crack growth and crack bridging prior to the onset of catastrophic failure.

Attempts were also made to estimate the degree of hardening due to the constrained yielding of the ductile phase reinforcements. This was done by measuring the Vickers microhardness

values at several points along fibers in undeformed specimens, and within the fibers in the unfractured halves of the double edge notched specimens that were examined after monotonic loading to failure. Average values of the reinforcement microhardness were thus obtained from undeformed and deformed fibers using 20 measurements per fiber. The ratios of the average microhardness values in the deformed composites to those in the undeformed composites were used as estimates of the constraint parameter, α , which is given by :

$$\alpha = \frac{H_{vd}}{H_u} = \frac{\sigma_{yd}}{\sigma_{yu}} \quad (1.1)$$

where H is the hardness, σ_y is the yield stress, and subscripts d and u denote deformed and undeformed reinforcements, respectively.

1.2.4 Resistance Curve

An R-curve is a continuous record of toughness development in terms of K_{Ic} plotted against crack extension in the material as a crack is driven under a continuously increased stress intensity factor, K [75]. R-curves characterize the resistance to crack growth in materials subjected to monotonic loading. R-curve behavior is an indication of plastic work or energy dissipation due to crack-tip shielding processes.

R-curve may therefore result from crack bridging or/and blunting when a crack intercepts a second phase. The fracture toughness value is the value of K_{Ic} at instability condition. In this study, R-curve tests were performed on Single Edge Notched (SEN) bend test samples. The specimens were initially pre-cracked under far-field compression loading [87] to produce a sharp pre-crack. A load corresponding to lower stress intensity factor (below the initiation toughness) was applied and quickly removed. The specimen was then examined under an optical microscope. The applied loads were increased in steps of 5 % if no crack growth was detected.

1.2.5 Fatigue Crack Growth

Duplicate fatigue crack growth tests were performed on composite specimens and the pure monolithic Nb compacts. The tests were conducted on SEN specimens with initial notch-to-width ratios of 0.25. The other dimensions of the SEN specimens were the same as those in the specimens used for fracture toughness testing. The fatigue crack growth specimens were pre-cracked under far-field compression. They were then subjected to constant amplitude cyclic

loading at a stress ratio, $R = K_{\min}/K_{\max}$, of 0.1. A cyclic loading frequency of 10 Hz was employed in the tests. Low initial stress ranges, $\Delta\sigma = \sigma_{\max} - \sigma_{\min}$, corresponding to a stress intensity factor range of about $1 \text{ MPa}\sqrt{\text{m}}$ were applied initially for incremental loading stages of 10^6 cycles. The stress ranges were increased in incremental stages of 10% until crack growth was detected after 10^6 cycles with the high resolution ($2.5 \text{ }\mu\text{m}$) telescope that was used to monitor crack growth.

Upon the detection of crack growth, the stress amplitudes were subsequently maintained constant, except in cases where the cracks stopped growing at the reinforcement/matrix interface(s). Load increments between 5 and 10% were typically needed for continued crack growth in such cases. The interaction of the cracks with the underlying composite microstructure was also monitored by removing the samples from the servohydraulic test machine, and examining the specimens under an optical microscope. Both sides of the specimens were examined since the cracks were not always observed to have the same lengths on both sides of the specimens. Average crack lengths (of the two sides) were therefore used in the stress intensity factor and fatigue crack growth rate calculations. The fatigue tests were continued until the crack length-to-width ratios were approx. 0.65. The specimens were then deformed to failure under monotonic loading, and the fracture mechanisms in all the specimens were studied using SEM techniques.

1.3. Bend Strength

The bend strengths of the different composites are compared in Figure 1.4. The room-temperature strength of the Nb laminates was much higher than that of all the other systems. However, the Nb laminates had greater strengths than those of the other materials elevated temperature. The results presented in Figure 1.4 show that the strengths of the fiber-reinforced composites were generally lower than those of monolithic MoSi_2 at elevated-temperature, presumably as a result of the lower strengths of the Nb reinforcements at elevated temperature. The larger diameter fiber-reinforced composite also had lower bend strengths than the small diameter fiber-reinforced composite at temperatures below 1100°C , although it was stronger at higher temperatures. A significant rise in bend strength was typically observed in MoSi_2 and its composites with increasing temperature, and the strengths of all the composites decreased with increasing temperature, at temperatures above 1100°C .

Reasons for the trends in the bend strength data with increasing temperature are difficult to identify due to the extreme flaw sensitivity of the materials. Nevertheless, it is interesting to note that the bend strength data is generally not predicted by constant strain simple rule-of-mixtures. The significant deviation from simple rule-of-mixtures may be attributed partly to the high flaw sensitivity (low fracture toughness) and the presence of a relatively high density of flaws in the

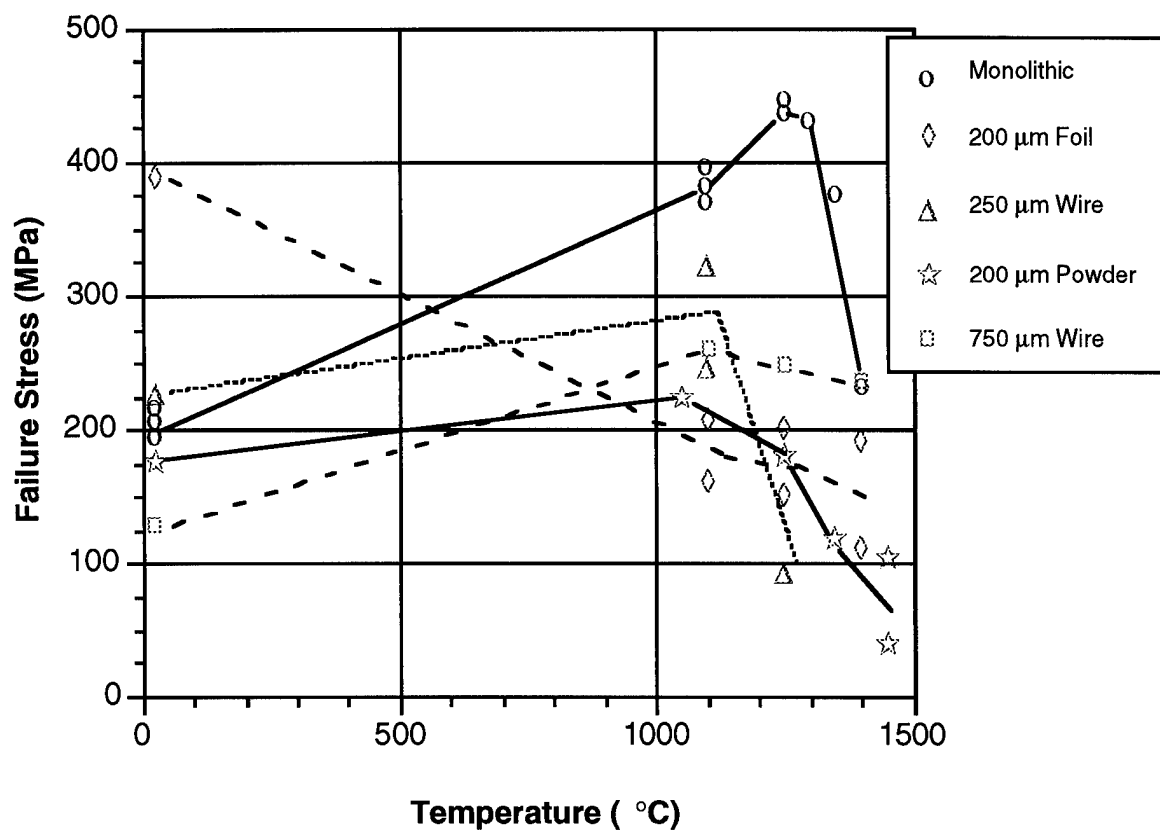


Figure 1.4 Effects of Temperature on Bend Strength

MoSi₂ matrix (Figures 1.1-1.3). Premature crack initiation may therefore occur before the true ultimate tensile stress is reached. Similarly, the microcracks or Kirkendall voids within the layered interfacial regions in the different composites may also promote premature crack initiation in the composites. Further work is clearly needed to improve our basic understanding of elevated-temperature strengthening mechanisms in Nb-reinforced MoSi₂.

1.4. Fracture

1.4.1 Particulate-Reinforced Composites

The average fracture toughness data obtained from the particulate-reinforced composites are compared with those obtained from other composites in Figure 1.5. Also included in Figure 1.5, are data from previous studies on Mo and W particulate-reinforced MoSi₂ composites [13] and structural aluminum alloys which typically have anisotropic fracture toughness values between 15 and 25 MPa√m [26]. Figure 1.5 shows that reinforcement morphology has a very strong effect on the fracture toughness of MoSi₂/Nb composites. The Nb particulate reinforced composites have fracture toughness values of approximately 5.7 MPa√m compared to matrix toughness values of ~3.6 MPa√m. The Nb particulate composites also have fracture toughness values that are comparable to those of Mo and W particulate-reinforced MoSi₂, as shown in Figure 1.5. Particulate reinforcement with thermodynamically compatible Mo, W and Nb phases therefore appears to have only a marginal effect on fracture toughness.

The degree of toughening in the particulate-reinforced composites can be estimated by modeling the shielding mechanisms that were observed in the fracture experiments. In the case of the particulate-reinforced composites, the shielding mechanisms can be inferred from the typical fracture modes presented in Figures 1.6a-1.6d. In the case of Nb particulate-reinforced composites, shielding was observed to occur via deflection by tilting and twisting via cleavage around the Nb reinforcements (Figure 1.6). This resulted in fracture surfaces that contained holes and mounds in regions in which deflection occurred continuously by tilting around the Nb particles (Figure 1.7c). Cleavage fracture of some of the Nb particles was also observed. However, there was no evidence of debonding at the particle/matrix interface of the cleaved Nb particles (Figure 1.7d).

The degree of toughening in the Nb particulate reinforced composites can therefore be estimated from the analysis by Faber and Evans [31] in which the combined effects of deflection by tilting and twisting are considered. For all the possible combinations of tilt and twist angles, the critical strain energy density of the composite is given by:

$$G_c = G_m(1 + 0.87V_f) \quad (1.2)$$

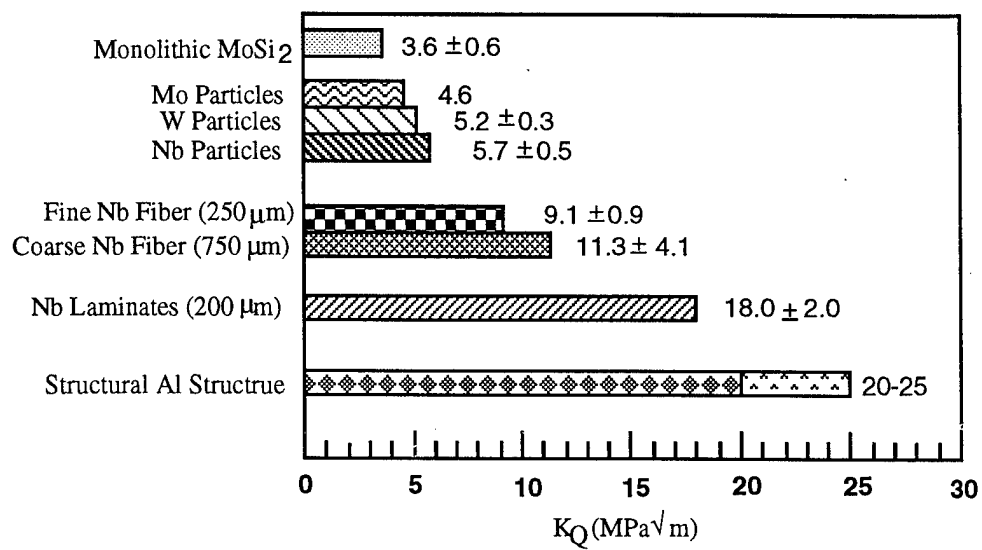


Figure 1.5 Comparisons of Fracture Toughness Data

Assuming linear elastic behavior of the composite thus yields:

$$K_c = \sqrt{E_c G_c} \quad (1.3)$$

where K_c is the fracture toughness of the composite and E_c is Young's modulus of the composite. Using constituent elastic moduli ($E_p = 103$ GPa and $E_m = 380$ GPa) taken from Ref. [26], and assuming constant strain rule-of-mixtures to obtain an estimate of the composite modulus ($E_c = 325$ GPa), the toughening ratio, $\lambda_d = K_c / K_m$, is thus estimated to be ~ 1.26 in the Nb particulate-reinforced composite. This toughening ratio suggests that the fracture toughness of the Nb particulate composite should be approx. $4.5 \text{ MPa}\sqrt{\text{m}}$, which is much less than the measured fracture toughness of $5.7 \text{ MPa}\sqrt{\text{m}}$. The difference between the measured and predicted fracture toughness (approx. 21%) is significantly greater than the 9% scatter in the experimental data (Figure 1.5). However, reasons for the discrepancy between the measured and predicted fracture toughness levels are not fully understood at present. Nevertheless, it is interesting to note that the fracture toughness of the ductile particle reinforced composites may be enhanced by restrained crack opening (in the vicinity of the crack-tip) and crack front bowing between particles, as suggested by Smith [18]. Further work is clearly needed to verify such speculation.

1.4.2. Fiber-Reinforced Composites

The 250 and 750 μm diameter composites had fracture toughness values of 9.1 and 14.1 $\text{MPa}\sqrt{\text{m}}$, respectively. These were associated respectively with approx. 2.1 and 2.8 mm of stable crack growth in the 250 and 750 μm diameter composites. The fracture toughness of the fiber-reinforced composites can be rationalized by assessing the implications of the typical failure mechanisms shown in Figures 1.7a-1.7d for composites with fiber diameters of 250 μm and 750 μm . Failure in the Nb fibers in the composites reinforced with 250 μm diameter fibers occurred by a combination of cleavage and ductile dimpled transgranular fracture (Figures 1.7a and 1.7b). Some evidence of debonding was also observed (Figure 1.7b) at the fiber/matrix interface. This was typically associated with ductile dimpled fracture modes in the surrounding Nb fibers, presumably as a result of the relaxation of constraint that can occur in the fibers due to debonding [32].

The brittle cleavage fracture modes observed in the vicinity of regions without debonding in Figure 1.7b are attributed to the effects of the high stress triaxiality induced in these regions. It is important to note, however, that both the brittle and ductile fiber fracture modes were preceded by fiber yielding. The fiber yield stress can therefore be estimated to be equal to the product of a constraint/triaxiality factor, α , and the uniaxial yield stress of the fiber, σ_{yf} . In the case of the

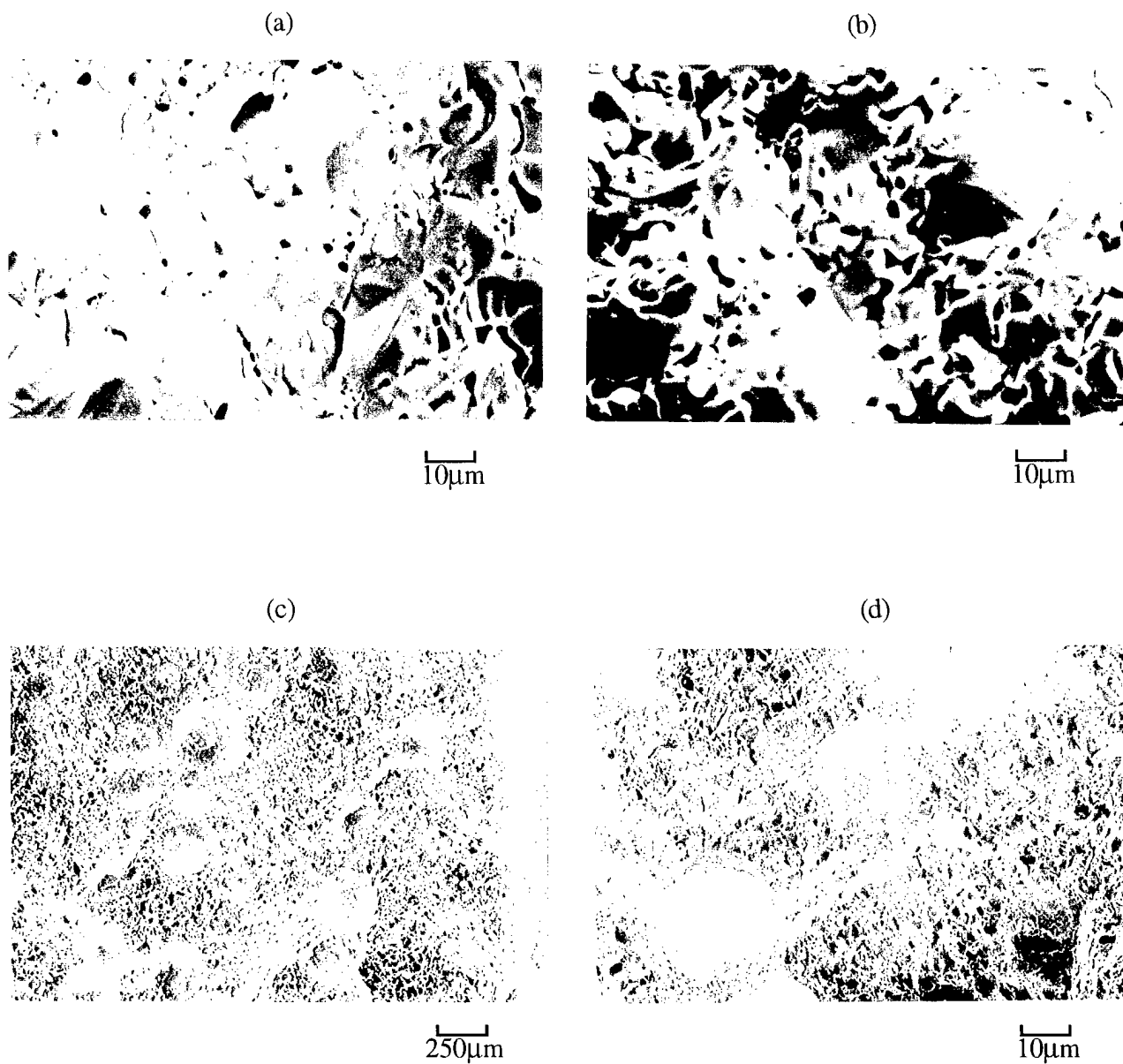


Figure 1.6 Fracture Surface Morphologies of $\text{MoSi}_2 + 20 \text{ vol.}\% \text{ Nb}$ Composite.
 (a) Mixed Cleavage + intergranular Fracture in Matrix,
 (b) Matrix Fracture,
 (c) Dimples Resulting From Decohesion and Pull Out of Particles From Matrix,
 (d) Cleavage Across Nb Particle

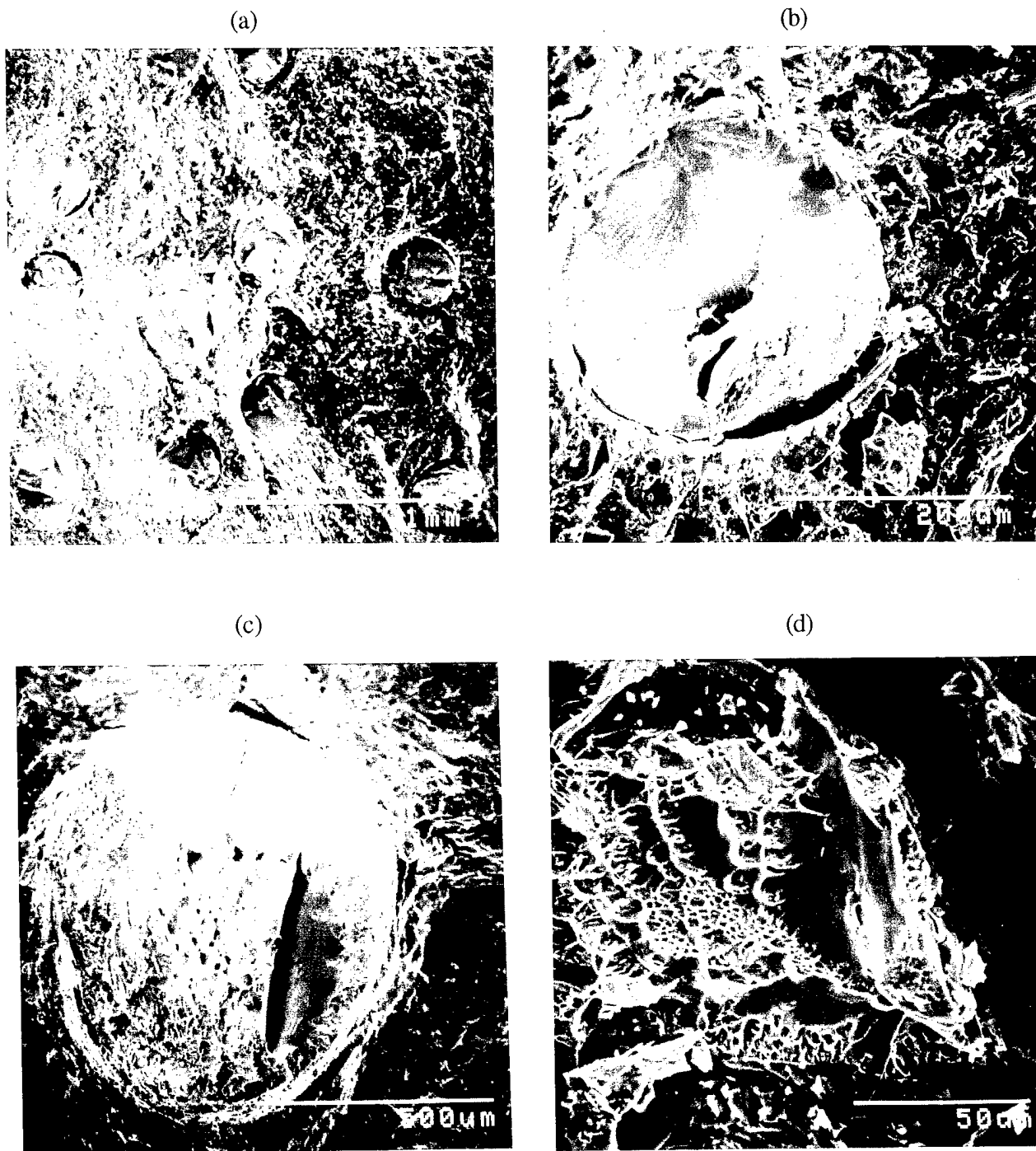


Figure 1.7 Typical Fracture Modes in Fiber-Reinforced Composites Under Monotonic Loading
(a, b) 250 μm Nb Fiber Composite; (c, d) 750 μm Nb Fiber Composite

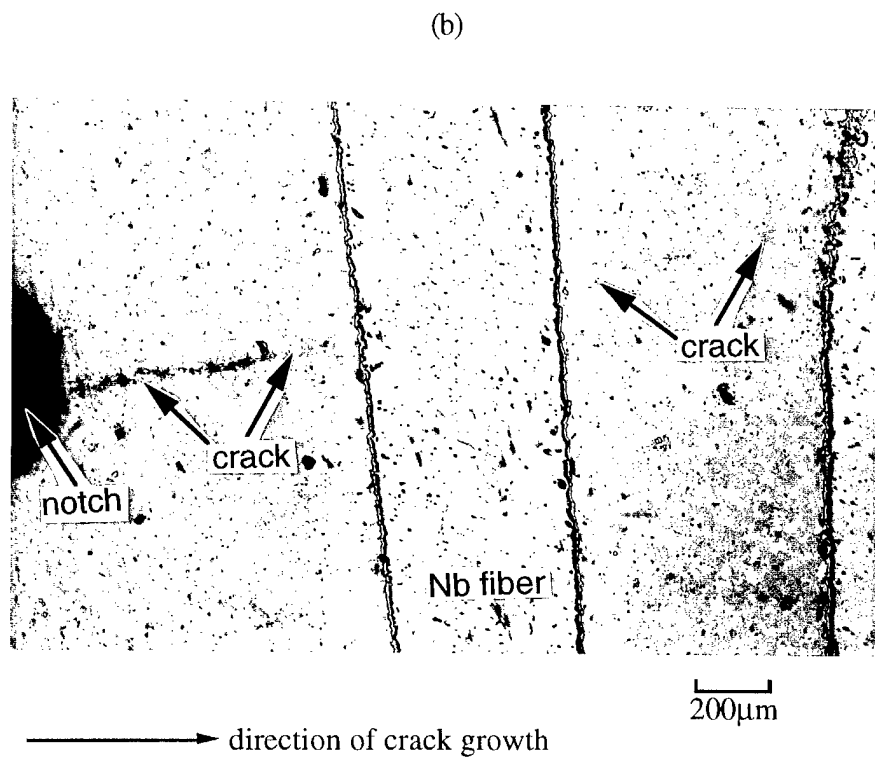
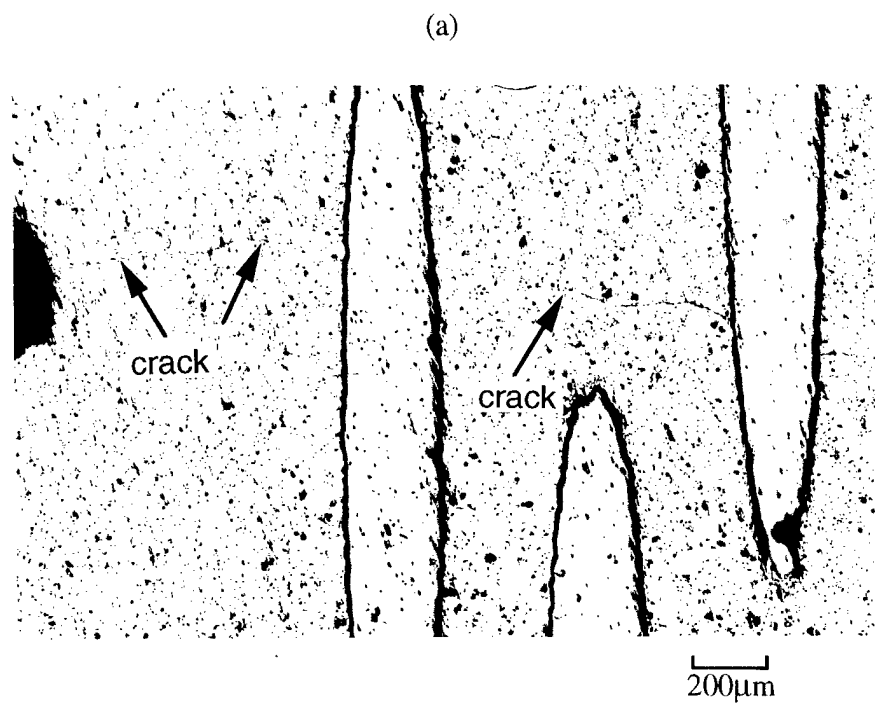


Figure 1.8 Crack Interactions With Composite Microstructure In Double Notched Specimens.
 (a) 250 μm Diameter Fiber Composite (b) 750 μm Diameter Fiber Composite

large diameter fiber composite, however, fiber fracture occurred predominantly by ductile dimpled transgranular failure (Figures 1.7c and 1.7d). There was also some evidence of debonding and crack-tip blunting at the fiber/matrix interfaces of the 250 and 750 μm diameter fibers.

The double notched specimens revealed that the fiber-reinforced composites were bridged (Figures 1.8a and 1.8b). The debonding at the fiber-matrix interfaces can also be considered as evidence of toughening by crack-tip blunting [29,30]. The toughening due to crack bridging may be expressed in terms of the stress intensity factor. This gives the applied stress intensity factor in the composite, K_c , as the sum of the matrix stress intensity factor, K_m , and the toughening component due to crack bridging, ΔK_b . The fracture toughness of the fiber-reinforced composites may thus be estimated from [27]:

$$K_c = K_m + \Delta K_b = K_m + 2\sqrt{\frac{2}{\pi}}\alpha V_f \int_0^L \frac{\sigma_y}{\sqrt{x}} dx \quad (1.4)$$

where K_m is the matrix fracture toughness, x is the distance behind the crack-tip, and L is the bridge length, which is equal to the distance between the crack-tip and the last unfractured row of fibers behind the crack-tip. The toughening ratio due to crack bridging under monotonic loading may thus be expressed as:

$$\lambda_b = \frac{K_c}{K_m} = 1 + \frac{2}{K_m} \sqrt{\frac{2}{\pi}} \alpha V_f \int_0^L \frac{\sigma_y}{\sqrt{x}} dx \quad (1.5)$$

The toughening due to crack bridging can be estimated from Equations 4 or 5. The resulting estimates (Table 1.1) generally indicate that bridging alone cannot account for the toughness levels in the fiber-reinforced composites. It is therefore important to analyze the shielding effects due to crack-tip blunting [29,30]. This can be accomplished using a micromechanics model developed recently by Chan [29]. This yields:

$$\lambda_{bt} = \frac{K_c}{K_m} = \left[1 + V_f(\Sigma - 1)\right]^{\frac{n-1}{2n}} \left[1 + V_f(\Gamma - 1)\right]^{\frac{n+1}{2n}} \left[\frac{E_c}{E_m}\right]^{\frac{n+1}{2n}} \quad (1.6)$$

or

$$\Delta K_{bl} = (\lambda_{bl} - 1)K_m \quad (1.7)$$

with

$$\Sigma = \frac{\sigma_y^d}{\sigma_y^m} \quad (1.8)$$

and

$$\Gamma = \frac{\epsilon_f^d}{\epsilon_f^m} \quad (1.9)$$

where K_∞ is the applied stress intensity factor, K_m is the matrix stress intensity factor, σ_y is the yield stress, ϵ_f is the fracture strain, n is the inverse of the strain hardening exponent, N (approx. 0.05), E_m is the matrix modulus, and subscripts m and d denote matrix and ductile phases, respectively. Using data summarized in Table 1.1, the toughening ratio due to crack-tip blunting can be obtained relatively easily. The predicted toughening levels are summarized in Table 1.2. These show that toughening due to blunting alone cannot account for the overall toughness of the composites.

The overall level of toughening increment, ΔK_{tot} , must therefore account for the combined effects of bridging and toughening. This may now be estimated if we neglect the potential interactions between crack-tip blunting and crack bridging mechanisms. The estimate of the overall toughening due to crack bridging and crack-tip blunting mechanisms is obtained simply by applying the principle of linear superposition. This yields:

$$\Delta K_{tot} = \Delta K_b + \Delta K_{bl} \quad (1.10)$$

The predicted overall fracture toughness is comparable to the measured toughness, in the case of the 750 μm diameter composite (Table 1.3). However, there is a large discrepancy (approx.

TABLE 1.1 CRACK BRIDGING IN MoSi₂/Nb COMPOSITES

| Type of Reinforcement | V_f | $L(\text{mm})$ | α | λ_b | ΔK_b (MPa $\sqrt{\text{m}}$) |
|----------------------------|-------|----------------|----------|-------------|--|
| 250 μm Fiber | 0.10 | 2.1 | 1.3 | 1.9 | 3.7 |
| 750 μm Fiber | 0.16 | 2.8 | 1.6 | 2.4 | 5.0 |
| 200 μm Laminate | 0.20 | 3.5 | 1.4 | 2.3 | 6.58 |

TABLE 1.2 CRACK-TIP BLUNTING IN MoSi₂/Nb COMPOSITES

| Type of Reinforcement | $\epsilon_{yd} / \epsilon_{ym}$ | $\sigma_{yd} / \sigma_{ym}$ | λ_{bl} | ΔK_{bl} (MPa $\sqrt{\text{m}}$) |
|----------------------------|---------------------------------|-----------------------------|----------------|---|
| 250 μm Fiber | 1.2 | 1.8 | 1.3 | 3.0 |
| 750 μm Fiber | 1.5 | 1.8 | 1.5 | 3.6 |
| 200 μm Laminate | 2.0 | 1.8 | 1.8 | 4.6 |

TABLE 1.3 CRACK-TIP BLUNTING IN MoSi₂/Nb COMPOSITES

| Type of Reinforcement | Bridging ΔK_b | Blunting ΔK_{bl} | Total K_{total} | Measured K_{exp} |
|----------------------------|--------------------------|-----------------------------|-----------------------------|------------------------------|
| 250 μm Fiber | 3.7 | 3.0 | 10.3 | 9.1 |
| 750 μm Fiber | 5.0 | 3.6 | 12.2 | 14.1 |
| 200 μm Laminate | 6.6 | 4.6 | 14.8 | 18.0 |

Note that matrix toughness = 3.6 MPa $\sqrt{\text{m}}$

30%) between the measured and predicted fracture toughness values in the case of the 250 μm diameter composite (Table 1.3). This discrepancy is greater than the experimental error in the fracture toughness measurement, and it may be due to possible interactions between crack-tip blunting and bridging mechanisms. The predictions also show that the higher fracture toughness values of the larger diameter fiber composites can be attributed partly to the differences in the blunting toughening ratios (Table 1.3). Table 1.3 also shows clearly that the toughening levels in the fiber-reinforced composites are much less than those in the laminated composites.

1.4.3. Laminated Composites

The measured fracture toughness values obtained from the laminated composites were between 16 and 20 $\text{MPa}\sqrt{\text{m}}$. These were associated with approx. 3.0 mm of stable crack growth. The fracture toughness levels are clearly much higher than those of the particulate and fiber-reinforced composites (Figure 1.5). It is therefore important to try to understand why the laminated composites are so tough. As in the previous sections, the relatively high fracture toughness of the laminated MoSi_2/Nb composite can be understood of evaluating the contributions from crack-tip shielding after careful consideration of the relevant fracture/toughening mechanisms. Unlike the particulate (Figures 1.6a-1.6d) and fiber-reinforced (Figures 1.7a-1.7d) composites, fracture in the laminated composites occurred completely by plastic stretching and ductile dimpled failure of the Nb layers (Figures 1.9a and 1.9b). Extensive matrix cracking was also observed in the laminated composites (Figure 1.9c), along with evidence of crack bridging and crack-tip blunting (Figures 1.9d). The laminated composites therefore exhibited the clearest evidence of ductile fracture and ductile phase toughening (Figures 1.9a-1.9d).

Evidence of multiple matrix cracking on the sides the double edge notched specimens is presented in Figures 1.9c and 1.9d. The average saturation matrix crack spacing observed in the double notched specimens was ~ 1.3 mm after fracture of one of the notches. Bridge lengths were also estimated by careful examination of the sides of the double edge notched specimens. The average bridging length in the laminated composites was also determined to be ~ 2.9 mm. The toughening increments due to crack bridging and crack-tip blunting can therefore be calculated using equations presented earlier. The results are given in Tables 1.1 and Table 1.2 in which the predicted toughening levels are compared with the measured values. The results show that neither crack bridging nor crack-tip blunting can account solely for the overall toughness of the composites.

The overall fracture toughness of the bridged laminated MoSi_2/Nb composites must therefore assess the contributions from crack bridging and crack-tip blunting. This can be achieved by



Figure 1.9 Typical Deformation and Fracture Modes in Laminated Composites.
(a) Ductile Dimpled Fracture of Nb Layer; (b) Extensive Plastic Stretching of Nb Layers; (c) Multiple Matrix Cracking; and (d) Crack Bridging and Crack-Tip Blunting By Nb Layers.

applying the principle of linear superposition. The resulting predictions obtained from Equation 10 are summarized in Table 1.3. The overall laminated composite toughness is estimated to be approx. $14.7 \text{ MPa}\sqrt{\text{m}}$. This is lower than the measured toughness values of approx. $18 \text{ MPa}\sqrt{\text{m}}$ that was obtained from the laminated composites (Table 1.3). The differences between the measured and predicted toughness levels in the laminated composites are greater than the experimental scatter in the measured fracture toughness data (Figure 1.5). This suggests that the overall toughening (Table 1.3) may be enhanced by interactions between crack bridging and blunting. However, such analysis is beyond the scope of the present report.

Finally in this section, it is important to discuss the implications of the current results for potential structural applications. Structural aluminum alloys have orientation dependent fracture toughness levels that are typically between 15 and $25 \text{ MPa}\sqrt{\text{m}}$ [31]. The lower fracture toughness levels are typically observed in the short transverse orientations, especially in forged and/or rolled products. The fracture toughness levels in the laminated MoSi_2/Nb composites are therefore close to those of structural aluminum alloys that are currently used in a wide range of structural applications. However, unlike structural aluminum alloys, the fracture toughness of the MoSi_2/Nb laminates do not appear to be very orientation dependent. Preliminary average fracture toughness values of approx. $16 \text{ MPa}\sqrt{\text{m}}$ have been obtained from specimens with cracks parallel to the Nb layers. These are only 11% lower than the average fracture toughness obtained from MoSi_2/Nb laminates with cracks perpendicular to the laminae. The MoSi_2/Nb laminates therefore appear to be tough when the cracks are parallel or perpendicular to the Nb layers. However, more detailed resistance-curve experiments are needed to distinguish between the crack initiation and propagation stages associated with potential R-curve behavior.

1.5. Resistance Curve Behavior

Resistant curve (R-curve) behavior of MoSi_2/Nb Composites was shown in Figure 10. The fiber-reinforced composites (250 μm and 750 μm fiber) show similar R-curve behavior. However, the 200 μm Nb laminate-reinforced composite has better resistance to the crack growth.

Crack growth in the R-curve test appeared to be intermittent (crack is not stable in the MoSi_2 matrix). R-curve behavior in MoSi_2/Nb Composites result from crack bridging or/and blunting when a crack intercepts a ductile Nb fiber or layer. We can use the model described before to predict the toughening due to crack bridging and crack-tip blunting, and thus predict the R-curve behavior. A schematic illustration of crack growth in a 250 μm Nb fiber-reinforced composite was shown in Figure 1.11. We assume toughening due to crack-tip blunting is the same for the crack with or without bridging. Use Equation 1.5 and 1.6, we can calculate the toughening due to crack bridging and crack-tip blunting as the crack propagate. The calculate value is presented

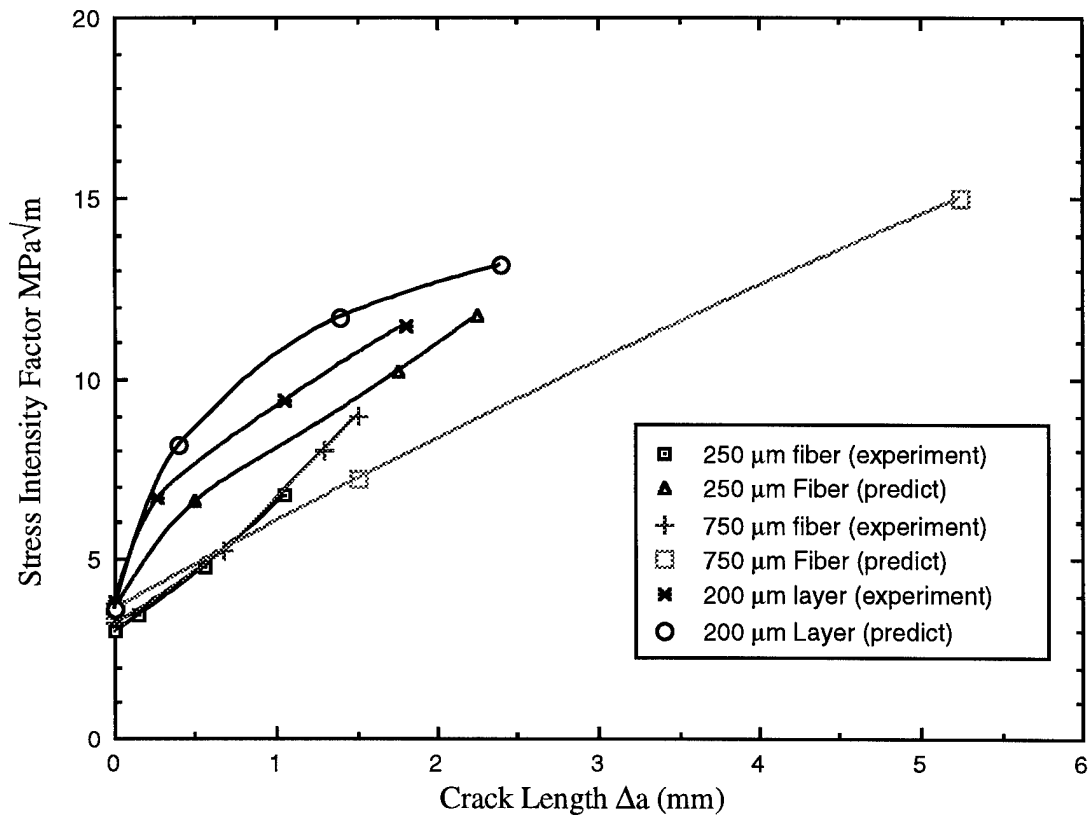
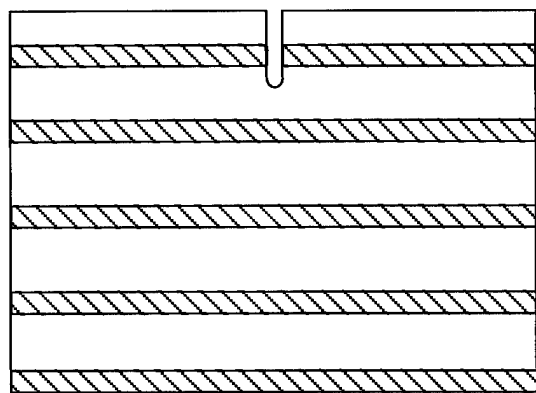
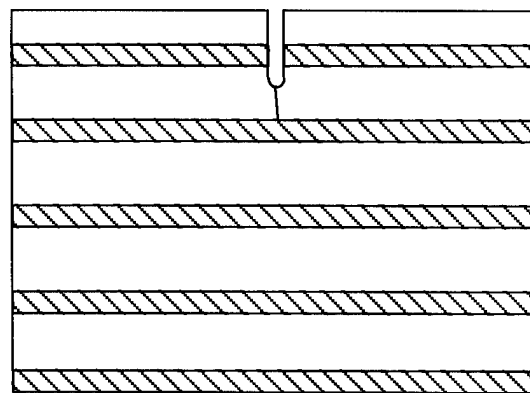


Figure 1.10 Resistance Curve Behavior (Experimental vs. Predicted)



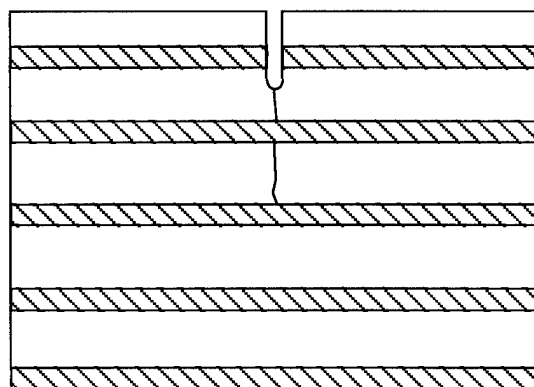
$\Delta a=0$

(c)

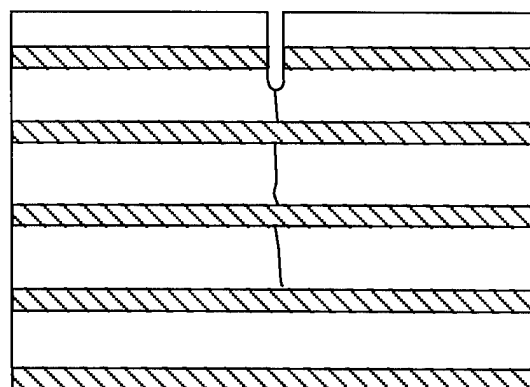


$\Delta a=500 \mu\text{m}$
 $\Delta K_b=3 \text{ MPa}\sqrt{\text{m}}$
 $\Delta L=0$
 $\Delta K_{br}=0$

(d)



$\Delta L=1250 \mu\text{m}$
 $\Delta K_b=3 \text{ MPa}\sqrt{\text{m}}$
 $\Delta K_{br}=3.65 \text{ MPa}\sqrt{\text{m}}$



$\Delta L=2500 \mu\text{m}$
 $\Delta K_b=3 \text{ MPa}\sqrt{\text{m}}$
 $\Delta K_{br}=5.1 \text{ MPa}\sqrt{\text{m}}$

Figure 1.11 Schematic Illustration of Crack Growth Sequence in a 250 μm Nb Fiber-Reinforced MoSi_2 Composite.

on Figure 1.11. The predicted R-curve for fiber and laminate reinforced composites were presented in Figure 1.10. The predicted R-curves appear to fit the ones obtained by experiment.

1.6. Fatigue Crack Growth

1.6.1 Particulate-Reinforced Composites

Fatigue crack growth rate data are presented for the Nb particulate-reinforced composites in Figure 1.12. The authors were not able to obtain stable fatigue crack growth rate data from monolithic MoSi₂ that was tested under three-point bend loading after compression pre-cracking. However, room- and elevated-temperature monolithic MoSi₂ fatigue crack growth rate data, taken from Ref. [33], is included in Figure 1.12 for comparison. Unlike monolithic MoSi₂ in which stable fatigue crack growth was difficult to obtain, stable fatigue crack growth was observed by the authors in the MoSi₂/Nb particulate composite in the stress intensity factor, ΔK range between ~ 0.5 and $5 \text{ MPa}\sqrt{\text{m}}$. The fatigue crack growth rates were very fast compared to those in monolithic materials, and the Paris exponent was ~ 9.4 compared to typical values between 2 and 4 in monolithic metals [34], and values between 15 and 50 in ceramics [35-38]. Unlike monolithic MoSi₂ in which relatively straight crack paths were observed under compression fatigue loading (Figure 1.13a), the cracks tended to deflect by tilting and twisting around the interfaces of the Nb particles under four-point bend loading (Figure 1.13b). Fatigue crack growth in the MoSi₂ matrix occurred mainly by transgranular cleavage along with some incidence of intergranular fracture (Figures 1.14a and 1.14b).

1.6.2 Fiber-Reinforced Composites

The interaction of the fatigue cracks with the microstructure of a typical fiber-reinforced composites is illustrated in Figure 1.14c. Fatigue damage initiated from the notch, and propagated to the first row of fibers, prior to some debonding at the first fiber/matrix interface. Subsequent crack extension then occurred from the other side of the fiber, thus resulting in the formation of a bridging zone in the regime between the crack-tip and the first row of Nb fibers ahead of the crack-tip. No evidence of fiber rupture was observed until very high ΔK levels were reached. This is in contrast with the high incidence of fiber rupture that was observed in the double-notched specimens which were deformed under monotonic loading. The lower levels of debonding and fiber fracture observed under cyclic loading are attributed to the lower crack opening displacements at relatively low ΔK levels under cyclic loading.

Fatigue fracture mechanisms in the fiber-reinforced composites (Figures 1.14c and 1.14d) were similar to those observed in the particulate-reinforced composites (Figures 1.14a and 1.14b). The Nb fibers therefore failed by cleavage fracture mechanisms under cyclic loading. This is in contrast to the mostly ductile modes observed in the fiber-reinforced composites under

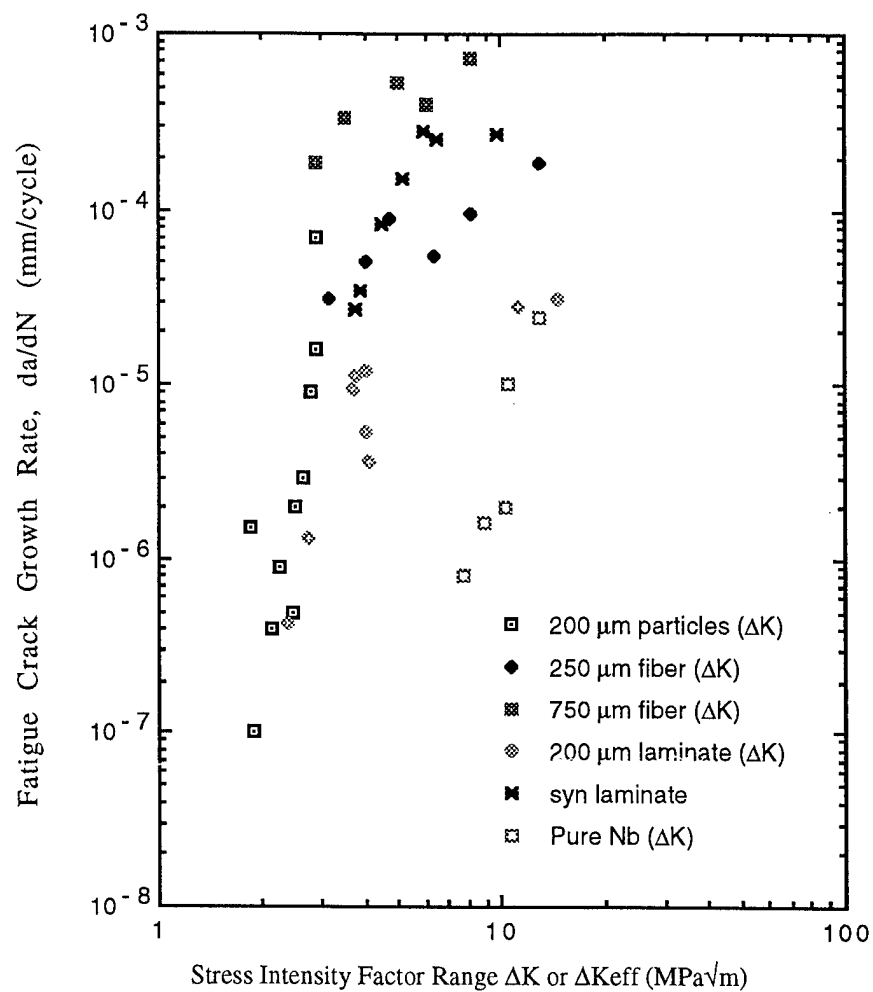


Figure 1.12 Summary of Fatigue Crack Growth Rate Data

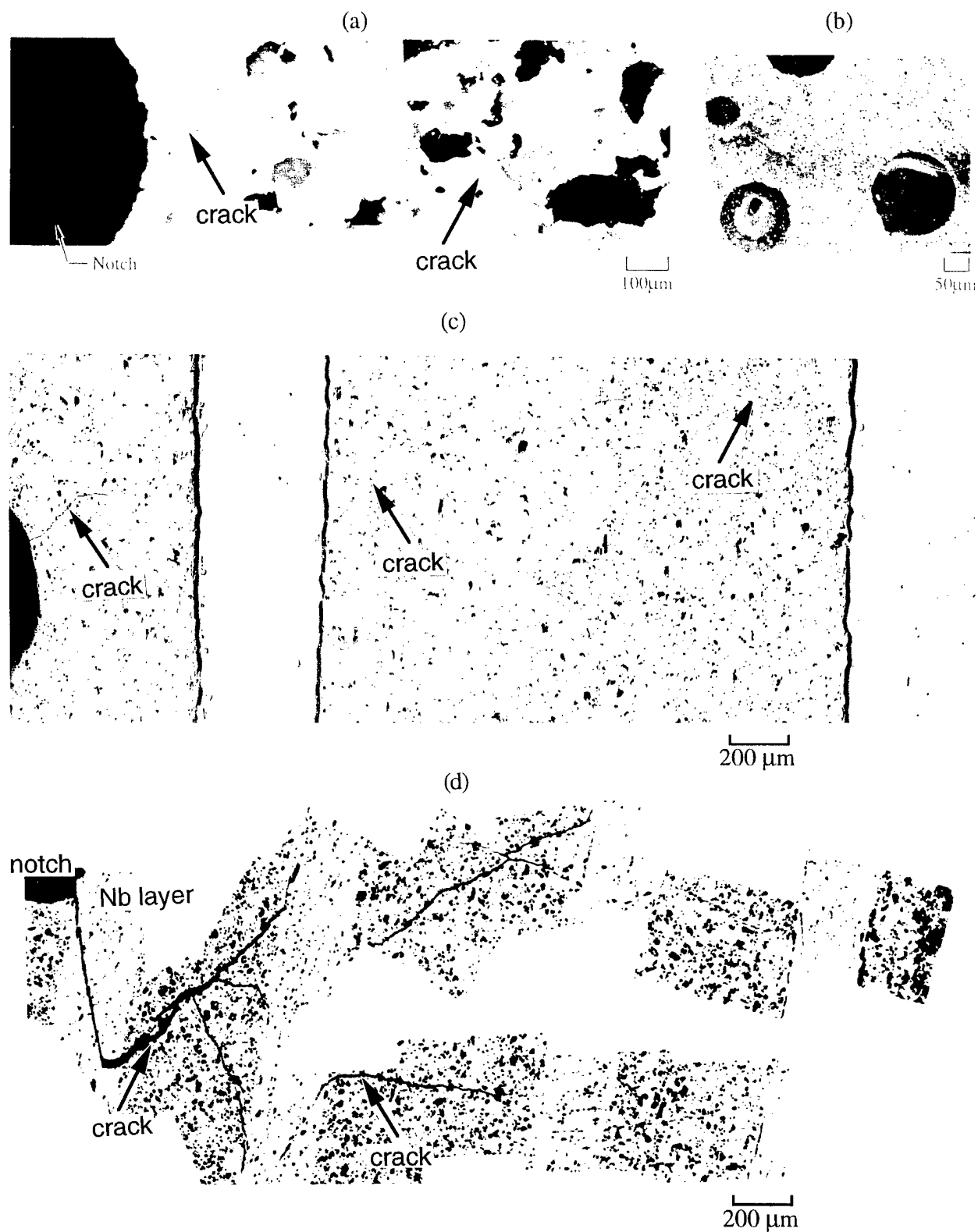


Figure 1.13 Interactions of Fatigue Cracks With Microstructure
 (a) Compression Pre-Crack in Monolithic MoSi_2 ; (b) Deflection in Particulate-Reinforced Composites; (c) Bridging and Blunting in Fiber Composite; and (d) Multiple Cracks in Laminated Composite

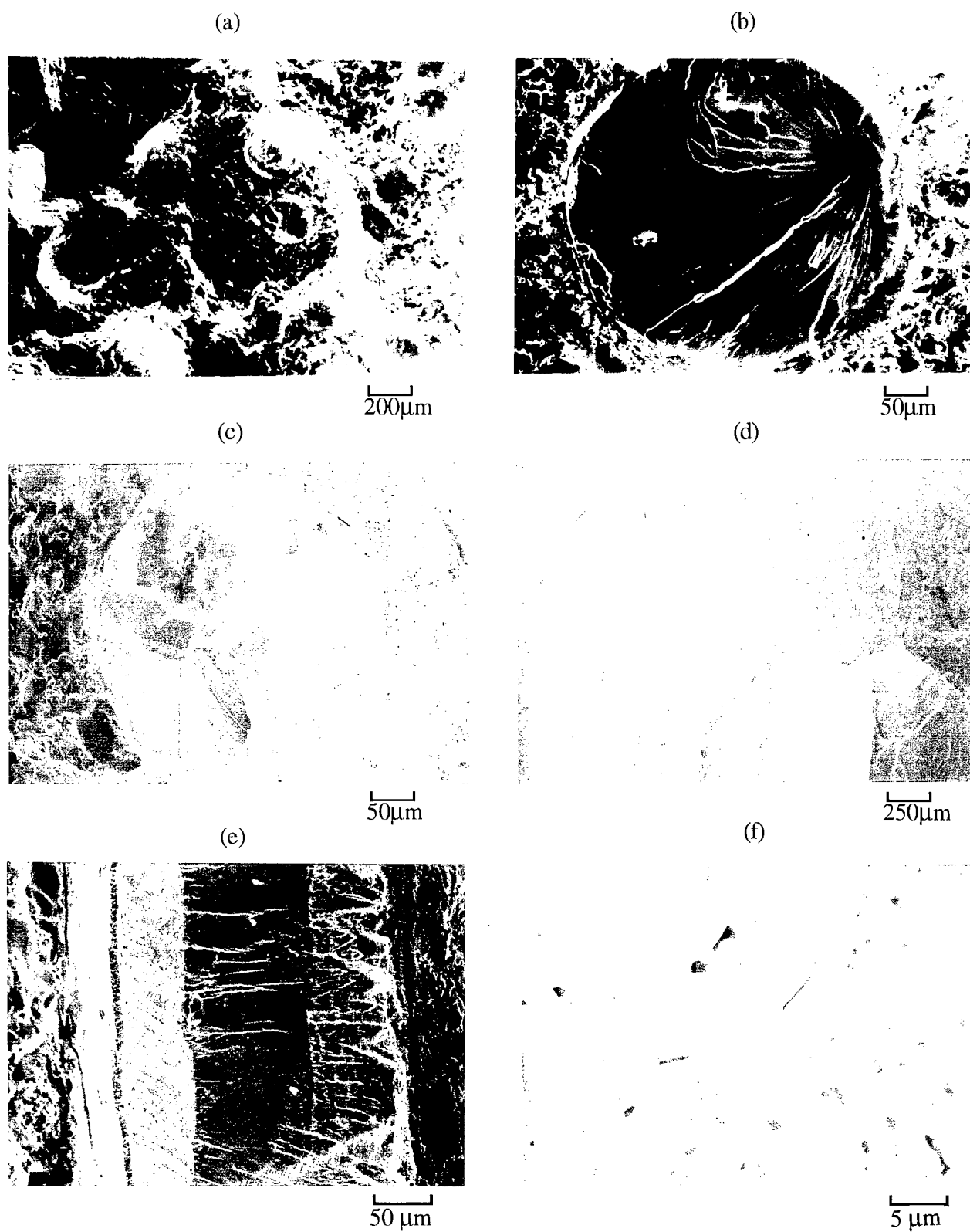


Figure 1.14 Typical Fatigue Fracture Modes. (a,b) Particulate-Reinforced Composites
 (c) 250 µm Diameter Fiber Composite (d) 750 µm Diameter Fiber
 (e,f) 200 µm Laminated Composite

monotonic loading (Figures 1.7a-1.7d). Reasons for the occurrence of cleavage fracture in the Nb reinforcements deformed under cyclic loading are unclear at present. However, it is possible to speculate that the brittle cleavage fracture modes are due to high strain rates associated with cyclic crack growth.

Crack growth in the fiber-reinforced composites was intermittent in the fiber/matrix interface regime. Nevertheless, average fatigue crack growth rate data was obtained which included some components of intermittent crack growth. Typical average fatigue crack growth rate data obtained for the fiber-reinforced composites are presented in Figure 1.12. The fiber-reinforced composites with the smaller diameter (250 μm) fibers are more resistant to fatigue crack growth than the fiber composites with the larger diameter (750 μm) fibers. This is due largely to the smaller distances between the rows of fibers in the smaller diameter composite. The reduction in the average fatigue crack growth rates induced as a result of crack-tip interactions in the fiber-matrix interfacial regime are therefore greater in the composite reinforced with the smaller diameter fibers.

Finally in this section, it is important to note that crack bridging did not appear to have a significant effect on the fatigue crack growth rate data that was obtained from the fiber-reinforced composites. This was confirmed by assessing the role of crack bridging using the method proposed by McMeeking and Evans [28]. This gives the following expression for the stress intensity factor at the crack-tip of a bridged crack subjected to cyclic loading:

$$\Delta K_{\text{tip}} = 2K_{\text{tip}}(\Delta\sigma/2) \quad (1.11)$$

where $K_{\text{tip}}(\Delta\sigma/2)$ is the near-tip stress intensity factor at the cyclic mean stress, $\Delta\sigma/2$, for a bridged crack subjected to a maximum stress of $\Delta\sigma$ at a stress ratio, $R = K_{\text{min}}/K_{\text{max}}$, of zero. The plots of fatigue crack growth rate versus the effective crack-tip stress intensity factor range are presented in Figure 1.12. These are very close to the plots of fatigue crack growth rate versus the applied stress intensity factor range, i.e., the effects of crack bridging are relatively small under cyclic loading conditions. The Paris coefficients are also very similar for the fatigue crack growth rate plots obtained from the applied and effective ΔK values.

1.6.3 Laminated Composites

The fatigue crack growth rate data for the laminated composites are presented in Figure 1.12. The laminates have much slower fatigue crack growth rates than the particulate- and fiber-reinforced composites. The laminate fatigue crack growth rates were also significantly greater than those in the pure Nb compacts, and crack growth in the laminated composites was intermittent. The intermittent nature of crack growth was due to the interactions of the cracks

with the ductile Nb layers. The fatigue crack paths in the laminated composites (Figure 1.13d) were similar to those obtained under monotonic loading at lower stress intensity factor ranges (Figures 1.8a and 1.8b). Toughening in the laminated composites therefore occurred by a combination of crack-tip blunting and crack bridging in the low/mid ΔK regime. However, crack bridging was not observed in the high ΔK regime because the cracks extended into the Nb reinforcements in this regime. Stable fatigue crack growth in the Nb laminae occurred by a combination of flat cleavage-like (Figure 1.14e) and shear modes (Figure 1.14f). The observed crack-tip shielding mechanisms (crack bridging and crack-tip blunting) in the different fatigue crack growth regimes are difficult to model due to complex load reversal effects that occur under cyclic loading. Also, the levels of crack-tip plasticity in the Nb layers are expected to be relatively small in the low-mid ΔK regime. The shielding effects due to crack-tip blunting should therefore be very small, except in the high ΔK regime where the levels of crack-tip plasticity may be significant in the Nb layers. The shielding effects due to crack-tip blunting were therefore not modeled under cyclic loading. However, the shielding due to crack bridging was modeled using an approach proposed originally by McMeeking and Evans [28]. The possible role of crack closure was also ignored in the analysis. The effective stress intensity factor, ΔK_{eff} , was thus equated to ΔK_{tip} , which is given by Equation 11. The resulting plots of fatigue crack growth rate versus effective stress intensity factor ranges are similar to the plots of fatigue crack growth rate versus applied stress intensity factor range (Figure 1.12), i.e., the shielding contributions from crack bridging are very limited under cyclic loading.

Finally, it is of interest to compare the fatigue crack growth rate data of the MoSi₂/Nb composites with those of alternative metallic and ceramic materials [34-38]. Most metallic materials have much slower fatigue crack growth rates and Paris exponents (typically between 2 and 4 [34]) than the composites examined in this study. However, the Nb fiber-reinforced and laminated MoSi₂/Nb composites have Paris exponents close to 1, while the particulate-reinforced MoSi₂/Nb composites have Paris exponents close to 9. The fatigue crack growth rates in the MoSi₂/Nb composites are also slower than those in many of the alternative ceramic materials which tend to have Paris coefficients between 15 and 50 [35-38]. The fatigue crack growth resistance of the model Nb-reinforced composites examined in this study are therefore intermediate between those of alternative ceramic and metallic materials.

1.7. CONCLUSIONS

1. Ductile phase toughened Nb fiber-reinforced MoSi₂ composites exhibit rising elevated-temperature flexure strengths at temperatures below 1100°C. However, the strengths of the composites decrease with increasing temperature above 1100°C, for reasons that are not fully

understood at present. The composite strengths are not predicted by constant stress/strain simple rule-of-mixtures, presumably as a result of the strong flaw sensitivity of the composites.

2. Fracture of "ductile" Nb reinforcements may occur by ductile or brittle fracture modes. Cleavage fracture is promoted by faster strain rates and cyclic loading in particulate- and fiber-reinforced composites. The incidence of ductile dimpled fracture increases with increasing fiber diameter under monotonic loading. However, the Nb particles always fail by cleavage, while Nb layers in the laminates fail by ductile dimpled fracture under monotonic loading.

3. Particulate-reinforcement promotes only marginal (20-30%) improvements in fracture toughness. More significant improvements in fracture toughness (100-300%) are obtained via fiber-reinforcement, and the fracture toughness values of the fiber-reinforced composites increase with increasing fiber diameter. The most significant improvements in fracture toughness (400-500%) are obtained from laminated composites reinforced with 200 μm thick laminae.

4. Toughening of the Nb particulate-reinforced composites occurs partly by crack deflection via continuous tilting and twisting. Toughening in the Nb fiber- and laminate-reinforced composites occurs by crack-tip blunting and crack bridging. The toughening mechanisms are similar under monotonic and cyclic loading, and the shielding effects of individual toughening mechanisms can be estimated using micromechanics models.

5. Fatigue crack growth rates in composites reinforced with 750 μm diameter Nb fibers are about an order-of-magnitude faster than those in composites reinforced with the 250 μm diameter Nb fibers, and two order of magnitudes faster than those in laminated composites reinforced with 200 μm thick Nb laminae. The laminated composites have similar crack growth resistance to the particulate composites in near-threshold regime. However, crack growth rates in the composites are much faster than those in monolithic Nb. Fatigue crack growth in the composites is intermittent.

Chapter 2

Transformation Toughening in MoSi₂

2.1. Introduction

Molybdenum silicide (MoSi₂) is currently being considered as a high temperature material for structural applications in the next generation of propulsion aerospace vehicles due to its attractive combinations of high temperature oxidation/corrosion resistance, high melting point (2030 °C), good thermal conductivity and moderate density (6.24 g/cm³) [39,40]. However, the potential use of MoSi₂ in structural applications is currently limited by a catastrophic oxidation (pest) problem at moderate temperatures (500-650°C)[41,42], and its brittle behavior at room temperature [21,24]. Several efforts have been made to improve the room-temperature fracture toughness of MoSi₂ [43-47]. These include the use of ductile phase toughening with thermodynamically compatible (Nb, W or Mo) reinforcements [12-15], brittle reinforcement with SiC whiskers [44,45] or TiC particles [46], and transformation toughening with CaO or Y₂O₃ stabilized ZrO₂ particles [47-49]. Limited improvements in the toughness of MoSi₂ have also been achieved via solid solution alloying with WSi₂ [50].

Ductile phase reinforced MoSi₂ composites have been shown to have fracture toughness levels that are between 20 and 500% greater than those of monolithic MoSi₂ [4,6,9,12,13]. Unfortunately, however, these composites have limited high temperature strength [21,42]. Also, the high temperature oxidation resistance of the ductile phase toughened composites is very limited due to the poor oxidation resistance of the refractory metals that are often used to toughen the ductile phase reinforced MoSi₂ composites. Brittle reinforced MoSi₂ composites are therefore particularly attractive due to their inherent oxidation resistance. Such composites appear to offer the opportunity to develop MoSi₂ composites with attractive combinations of elevated temperature strength and oxidation resistance, as well as improved fracture toughness [44-49]. Unfortunately, however, the improvements in fracture toughness (10-250%) that can be achieved in the brittle reinforced MoSi₂ composites have been generally less than those obtained via ductile phase toughening [12-15]. There is therefore a need to develop brittle phase reinforced MoSi₂ composites with improved fracture toughness.

Transformation toughening has been shown to promote improved fracture toughness in MoSi₂ in recent work by Petrovic et al. [47,48] and Soboyejo et al. [49]. The indentation fracture toughness measurements by Petrovic et al. [47,48] on CaO and Y₂O₃ stabilized ZrO₂ particulate reinforced composites have shown that fracture toughness improvements between 10 and 250% can be achieved in MoSi₂ composites. Fracture toughness measurements by Soboyejo

et al. [49] on single notched bend specimens fabricated from MoSi₂ composites reinforced with Y₂O₃ stabilized ZrO₂ particles have also revealed that toughening (10-30%) can also be achieved in such materials.

Contrary to all expectations, the highest fracture toughness values have been obtained from materials reinforced with unstabilized monoclinic zirconia particles, i.e., ZrO₂. Preliminary laser Raman spectroscopy and optical interference studies by Soboyejo et al. [49] have also shown that transformation toughening (in MoSi₂ composites reinforced with 0.7 μm sized Y₂O₃ stabilized ZrO₂ particulates) only occurs when the metastable tetragonal phase is stabilized with 2 mole % Y₂O₃. The toughening mechanisms in the composites reinforced with zirconia stabilized with other yttria levels are therefore yet to be determined.

A novel micromechanics approach for the prediction of residual stress in transformation toughened composites is presented in this chapter of the report. The approach relies on the application of superposition concepts to the estimation of average residual stresses due to thermal expansion mismatch and multi-particle stress fields. Closed form analytical expressions are presented for the estimation of the effects of reinforcement volume fraction on average residual stresses in particulate-reinforced composites. The model is then applied to the prediction of residual stress in molybdenum disilicide composites reinforced with 20 vol. % of partially stabilized zirconia particles with yttria (Y₂O₃) contents between 0 and 6 mole %. The effects of yttria stabilization on crack-tip shielding are also assessed using a combination of fracture experiments and micromechanics analysis.

The chapter shows that reinforcement with unstabilized zirconia results in the highest fracture toughness (when compared with other levels of stabilization) due to the effects of compressive residual stresses. Further evidence is also presented to confirm that transformation toughening occurs only in composites reinforced with 20 vol. % zirconia stabilized with 2 mole % Y₂O₃. Toughening in composites reinforced with 20 vol. % of zirconia stabilized with 4 or 6 mole % yttria is attributed largely to the effects of microcrack shielding. The effects of yttria stabilization on elevated-temperature strength are also discussed. The chapter highlights the importance of combined use of experimental and analytical micromechanics and materials science concepts in the rationalization of the mechanical properties of transformation toughened composites.

2.2. Micromechanical Modeling

2.2.1 Transformation Toughening

Considerable effort has been expended in the development of a theoretical framework for the prediction of the toughening that can be achieved as a result of crack-tip stress-induced

transformations [50-64]. These transformations induce zone shielding effects that are associated with the volume increase (approx. 3-5 % in many systems) that occurs due to stress-induced phase changes. For simplicity, most of the micromechanics analyses have assumed spherical transforming particle shapes, and critical transformation conditions that are controlled purely by mean stresses, i.e., they have generally neglected the effects of shear stresses, which may be important, especially when the transformations involve deformation-induced twinning phenomena [54]. Nevertheless, the existing toughening models have been shown to provide reasonably good estimates of the level of transformation toughening, even when the stress-induced transformations are assumed to occur only as a result of mean stresses [55]. Transformation toughening will therefore be assumed to be induced only by mean stresses in this study, although the possible effects of shear stresses are recognized [53,58].

In general, the level of crack-tip shielding due to stress-induced transformations is related to the transformation zone size and the volume fraction of particles that transform in the regions of high stress triaxiality at the crack-tip. A transformation zone, akin to the plastic zone in ductile materials, is thus developed as a crack propagates through a composite reinforced with transforming particles. This is illustrated schematically in Figure 2.1. The size of the transformation zone associated with a Mode I crack under small scale transformation condition has been studied [54,55]. Based on the assumption that the transformation occurs when the mean stress level at the crack tip exceeds a critical stress value (σ_C^T), McMeeking and Evans [54] estimated the zone size for an idealized case in which all the particles within the transformation zone are transformed. Following a similar procedure, Budiansky et al. [55] give the following equation for the estimation of the height of the transformation zone (Figure 2.1):

$$h = \frac{\sqrt{3}(1+\nu)^2}{12\pi} \left(\frac{K}{\sigma_C^T} \right)^2 \quad (2.1)$$

where h is the half-height of the transformation wake (Figure 2.1), K is the far field stress intensity factor and ν is the Poisson's ratio. The toughening due to the transformation can also be expressed as [24,25,37]:

$$\Delta K_t = \frac{0.22E_c f \epsilon_C^T \sqrt{h}}{1-\nu} \quad (2.2)$$

where E_c is the elastic modulus of the composite, f is the volume fraction of transformed particles, ϵ_C^T is the transformation volume strain, which for the case of the tetragonal-to-monoclinic transformation in zirconia is approximately 0.04. This model assumes that the

volume fraction of the transformed material to be constant with increasing distance, x , from the crack face. However, in reality, the actual volume fraction of transformed phase varies with increasing distance from the crack face [64]. Equation 2.2 must therefore be expressed in integral form to account for the variation in the degree of transformation with increasing distance from the crack face. This yields the following expression for the toughening due to stress-induced transformations [64]:

$$\Delta K_t = \frac{0.22E_c \varepsilon_c^T}{1-\nu} \int_0^h \frac{f(x)}{2\sqrt{x}} dx \quad (2.3)$$

where $f(x)$ is a mathematical function that represents the fraction of transformed zirconia as a function of distance, x , from the crack. The critical transformation stress necessary to achieve the transformation can be expressed as a function of the total Gibb's free energy associated with the transformation from tetragonal-to-monoclinic phase. This may be estimated from [51,57]:

$$\sigma_c^T = \frac{\Delta G}{\varepsilon_c^T} \quad (2.4)$$

where σ_c^T is the critical stress and ΔG is the Gibb's free energy of the transformation. The above expression does account for the effect of the enthalpy terms in the equivalent Kirchhoff circuits for the transformation. Also, the potential mean stresses due to the thermal expansion mismatch between MoSi_2 and PSZ particles after processing have not been considered in the above analyses. Depending on the thermal expansion coefficients, the zirconia particles may be subjected to either mean tension or compression. The residual mean stress will be derived in detail in the next section. In general, however, if the mean stress is compressive, the far-field applied stress necessary for transformation will increase. On the contrary, the existence of tensile mean stress will trigger the transformation at a lower level of applied stress. As a result of this, the mean stress, σ_m , that is needed to induce the transformation of ZrO_2 particles is modified by the radial residual stress, σ_m . The modified critical condition for transformation is thus given by [51]:

$$\sigma_m = (\sigma_c - \sigma_0) \quad (2.5)$$

2.2.2 Residual Stress Analysis

Residual stresses in particulate reinforced composites occur mainly as a result of the thermal expansion mismatch between the reinforcements and the matrix materials [65]. However, most

of the existing solutions for residual stress have used unit cell methods to analyze the effects of the interactions between the stress fields that surround each of the individual particles[51]. Such interactions will be included in an analytical framework for the estimation of the residual mean stress levels in this study. Unlike some of the approximate numerical solutions reported recently in this area [66], an analytical expression is presented for the estimation of average residual stresses. This expression is obtained by considering the stress state arising from any random distribution of particles surrounding an arbitrary central particle.

We begin our analysis by considering any individual particle in a brittle matrix that is reinforced with a random distribution of particles (Figure 2.2). For clarity, the selected individual particle is shaded in Figure 2.2. However, it is important to note that any one of the particles in Figure 2.2 could have been shaded for the purpose of this study. The shaded particle therefore has no unique features that distinguish it from the other particles that were not selected. First, we consider the residual stress field that is induced as result of the thermal expansion mismatch between the reinforcement and the matrix. We then apply the principle of linear superposition to determine the effects of surrounding particles on the average residual stresses at the interfaces between the individual particles and the brittle matrix. An analytical solution is thus obtained for the prediction of the effects of reinforcement volume fraction on the residual mean stresses at the reinforcement/matrix boundaries. For each individual particle, the stresses, strains and displacement are obtained from the Lamé solutions. Equilibrium equations and Hooke's law in the chosen three-dimensional spherical coordinate system are thus given by the following equations [67]:

$$\frac{d\sigma_r}{dr} = \frac{2}{r}(\sigma_\theta - \sigma_r) \quad (2.6)$$

$$\sigma_\theta = \sigma_\phi \quad (2.7)$$

$$\varepsilon_\theta = \frac{u}{r} = \frac{1}{E}[(1-\nu)\sigma_\theta - \nu\sigma_r] \quad (2.8)$$

where, σ and ε respectively represent the stress and strain; subscripts r , θ and ϕ indicate the radial and tangential directions, respectively; u is the displacement in radial direction, E is the elastic modulus and ν is the Poisson's ratio. Stresses and displacement are given by the Lamé solutions [67]:

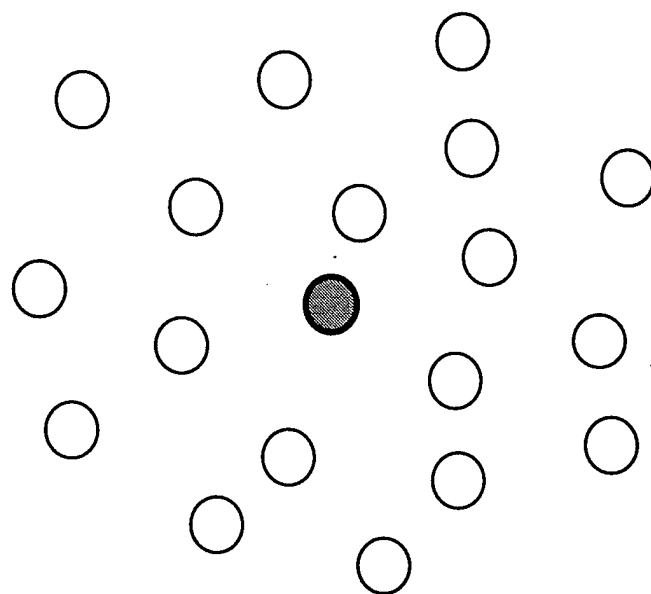


Figure 2.2 Schematic Illustration of Random Particle Configuration in Particulate Reinforced Composites

$$\sigma_r = A + \frac{B}{r^3} \quad (2.9)$$

$$\sigma_\theta = \sigma_\phi = A - \frac{B}{2r^3} \quad (2.10)$$

$$u = \frac{1}{E} \left[(1-2\nu) \cdot r \cdot A - \frac{1+\nu}{2} \cdot \frac{B}{r^2} \right] \quad (2.11)$$

where A and B are the so-called Lamé constants which will be determined later. For spherical particles, Since the Lamé stress cannot be infinite in Equations (2.9) and (2.10) when $r = 0$. Hence, $B = 0$ in Equations (2.9) - (2.11), so we have

$$\sigma_r = \sigma_\theta = \sigma_\phi = A_p = (\sigma_0)_i \quad (2.12)$$

$$u = \frac{1}{E_p} (1-2\nu_p) \cdot r \cdot A_p \quad (2.13)$$

where, $(\sigma_0)_i$ is the residual stress due to an individual particle in the matrix, E_p is the Young's modulus of the particle and ν_p is the Possion's ratio of the particle. In the matrix region, the stresses and displacement are given by:

$$\sigma_r = A_m + \frac{B_m}{r^3} \quad (2.14)$$

$$\sigma_\theta = \sigma_\phi = A_m - \frac{B_m}{2r^3} \quad (2.15)$$

$$u = \frac{1}{E_m} \cdot \left[(1-2\nu_m) \cdot r \cdot A_m - \frac{1+\nu_m}{2} \cdot \frac{B_m}{r^2} \right] \quad (2.16)$$

where, A_m and B_m are constants to be determined. E_m and ν_m are the elastic modulus and Possion's ratio of the matrix, respectively. Boundary conditions take the form:

$$\sigma_r \Big|_{r=a^-} = \sigma_r \Big|_{r=a^+} = (\sigma_0)_i \quad (2.17)$$

$$u|_{r=a^-} - u|_{r=a^+} = (\alpha_p - \alpha_m) \cdot \Delta T \cdot a \quad (2.18)$$

$$\sigma_r|_{r=R} = 0 \quad (2.19)$$

where a is the radius of the particle, R is the radius of the matrix, α_p and α_m are the thermal expansion coefficients of the particle and the matrix, respectively, $\Delta T = T_0 - T$, T_0 is the fabrication temperature, and T is the temperature at which the stress is determined. Combining equations (2.9), (2.10) and (2.11), we have

$$(\sigma_0)_i = \frac{E_m \cdot (\alpha_p - \alpha_m) \cdot \Delta T}{\frac{E_m}{E_p} \cdot (1 - 2\nu_p) + \frac{1}{1 - (V_p)_i} \cdot \left((1 - 2\nu_m) \cdot (V_p)_i + \frac{1}{2}(1 + \nu_m) \right)} \quad (2.20)$$

where, $(V_p)_i$ is the volume fraction of the central particle (Figure 2.2). When $(V_p)_i$ approaches zero, we have the solution for the special case of a single particle in an infinite matrix [65]. The residual mean stress is independent of coordinate system. Local variations in residual stress associated with the angular dependence of residual stress with θ and ϕ away from the composite are neglected by such mean stresses. Nevertheless, the residual mean stresses will be used as average measures of residual stress in this study. From the equations (2.15)-(2.18), the average residual stress $\bar{\sigma}_i$ due to each individual particle in the matrix, can be expressed as:

$$\bar{\sigma}_i = A_m = -\frac{(V_p)_i}{1 - (V_p)_i} \cdot (\sigma_0)_i \quad (2.21)$$

The contributions from surrounding particles to the residual mean stress, $\bar{\sigma}_i$, has an opposite sign to $(\sigma_0)_i$. This is because the residual stress contributions from the surrounding particles have opposite signs to those of the individual particles. They are also independent of the distance from the individual particles, and thus dependent only on the volume fraction of particles in the composite. It is therefore relatively easy to superpose the residual mean stress contributions from the surrounding particles on the residual mean (self) stresses of the central particles (Figure 2.2). Hence, by applying the superposition principle, the residual mean stress σ_0 acting on the central particle within a multiple-particle-reinforced composite (Figure 2.2) is given by:

$$\sigma_0 = (\sigma_0)_i + \sum_{k=1}^n \left(\bar{\sigma}_i \right)_k \quad (2.22)$$

The first term on the right side of the equation is the residual stress due to the individual particle, while the second term represents the sum of the contributions from all the other particles. Note that n is the number of particles that contribute to the residual mean stress experienced by each individual particle. Equation (2.22) may also be written as:

$$\sigma_0 = \gamma \cdot (\sigma_0)_i \quad (2.23)$$

where

$$\gamma = \frac{(n+1) \cdot (1 - V_p)}{n+1 - V_p} \quad (2.24)$$

The coefficient γ is defined as effective coefficient. It is a function of volume fraction and the number of the particles. Note that, in all cases, when $V_p \rightarrow 0$, $\gamma \rightarrow 1$; and when $V_p \rightarrow 1$, $\gamma \rightarrow 0$. Hence, when the volume fraction of the particles is small, there is very little effect of surrounding particles on the residual stress. However, when the volume fraction of the particles is large, the contributions from the surrounding particles to the overall residual stress are much larger.

In addition to the residual mean stresses induced as a result of the thermal expansion mismatch between the reinforcements and the matrix, residual stresses may also be induced as a result of the volume change associated with phase transformation from tetragonal to monoclinic phase that occurs during cooling from the processing temperature to room temperature. In the most extreme cases, the residual mean stresses associated with such phase transformations may be equated to the critical transformation stress which produces a stress-free volume expansion of approx. 4% [51,52]. When the resulting residual mean stresses are not relaxed by dislocation emission, the corresponding matrix reaction to this instantaneous volume change is a compressive hydrostatic residual stress which is given by [49]:

$$\sigma_C^T = \frac{f \cdot \Delta G}{\epsilon_C^T} \quad (2.25)$$

where σ_C^T is the critical transformation stress, f is the volume fraction of tetragonal phase that undergoes phase transformation during cooling from the processing temperature to room temperature, and ΔG is the Gibbs free energy of the phase transformation. The above expression does account for the effect of the enthalpy terms in the equivalent Kirchhoff circuits for the transformation.

The compressive residual stress induced as a result of phase transformation during cooling from the processing temperature will affect the overall level of residual stress at the reinforcement matrix interface. The overall residual stress may be estimated again by applying the superposition principle. This overall residual stress is therefore given by the sum of the hydrostatic interfacial residual stress values obtained from Equations (2.22)-(2.24) and the compressive hydrostatic stress values induced as a result of the transformation from tetragonal to monoclinic phase during cooling from the processing temperature. The overall hydrostatic residual stress can then be substituted into Equation (2.4) to determine the effects of residual stress on the critical conditions for transformation. The overall residual stress values may also be used to assess the possible shielding or anti-shielding effects that may occur, respectively, as a result of negative or positive residual stress values. Material property data that was substituted into the above equations is summarized in Table 2.1.

2.3. Experimental Procedures

2.3.1 Material and Microstructures

The molybdenum disilicide that was used in this study was procured from Cerac, Milwaukee, WI, in the form of -325 mesh powder (44 μm average diameter). The MoSi_2 powder was 99.5 % pure. Zirconia powder with different levels of yttria stabilization (0 mole %, 2 mole %, 4 mole % and 6 mole % designated respectively as: TZ-0Y, TZ-2Y, TZ-4Y and TZ-6Y hereafter) was procured from Tosoh Corporation, Bound Brook, NY. The average particle size of the 99 % pure yttria particles was 0.7 μm . Mixtures consisting of 80 vol. % MoSi_2 and 20 vol. % zirconia particles were dry phase blended by ball milling with zirconia media for 24 h. The phase blended powders were then poured into Nb cans, vacuum sealed by electron beam welding and hot isostatically pressed (HIPed) at 1400°C under 207 MPa pressure for 4 hours.

The microstructures of the HIPed composites were studied using optical, scanning and transmission electron microscopy (TEM). Foils for TEM were prepared from circular discs that were 3 mm in diameter. The slices, which were 150 μm thick, were electro-discharge machined (EDM) prior to grinding on both sides to a thickness of about 80 μm . The ground specimens were then dimpled with using a 30 N load with 1 μm diamond paste to a final thickness of about

Table 2.1 Summary of Mechanical and Thermal Properties

(a) Elastic Properties of PSZ Particles and MoSi₂ Matrix

| Property | Matrix | Particles |
|-----------------------|--------|-----------|
| Young's Modulus (GPa) | 380 | 205 |
| Possion's Ratio | 0.17 | 0.3 |

(b) Thermal Expansion Coefficients of PSZ Particles and MoSi₂ Matrix

| Matrix $\alpha_m (m / m / ^\circ C) \cdot 10^{-6}$ | | Particles $\alpha_p (m / m \cdot ^\circ C) \cdot 10^{-6}$ | | | |
|---|------|--|-------|-------|-------|
| | | | TZ-2Y | TZ-4Y | TZ-6Y |
| 20 °C | 6.8 | 100 °C | 8.9 | 8.2 | 7.9 |
| 400 °C | 8.3 | 400 °C | 10.0 | 9.5 | 9.2 |
| 800 °C | 9.2 | 700 °C | 10.6 | 9.7 | 10.0 |
| 1000 °C | 9.5 | 1000 °C | 10.7 | 10.4 | 10.3 |
| 1200 °C | 9.8 | 1300 °C | 10.7 | 10.4 | 10.2 |
| 1400 °C | 10.0 | 1500 °C | 10.4 | 10.4 | 10.1 |

30 μm . Finally, the foils were Ar ion milled to produce thinned regions for TEM examination. The TEM examination of the substructures and microcrack distributions was carried out using a transmission electron microscope that was operated at 200 kV.

2.3.2 X-ray Diffraction Analysis

Knowledge of the volume fractions of tetragonal and monoclinic phase in the different composites is required before an assessment of the shielding contributions from transformation toughening can be made (see Equations 2.2 and 2.3). As in previous studies [49,50], estimates of the bulk levels of monoclinic and tetragonal phase were obtained using X-ray diffraction techniques. These rely on a calibration curve that is obtained by plotting the ratios of X-ray peaks in powder mixtures of known proportions of tetragonal and monoclinic phase against the known volume fractions of monoclinic or tetragonal phase. Since the TZ-0Y reinforcements are fully monoclinic and the TZ-6Y reinforcements are fully tetragonal [49], the phase contents in the powder calibration mixtures were varied by mixing various proportions of the TZ-0Y and TZ-6Y powders. The existence of the monoclinic phase is indicated by the strong doublet peaks for (111) at $2\theta \approx 31.4^\circ$ and (111) planes at $2\theta \approx 28.2^\circ$. The tetragonal phase has its strongest peak at $2\theta \approx 30.5^\circ$ which corresponds to (111). Such a clear-cut difference of monoclinic phase content made these two powders ideal materials to calibrate the relationship between the volume fraction of transformable zirconia in the composites and the X-ray diffraction intensity.

After dry phase blending of the powder mixtures with zirconia media for 24 h to ensure uniform mixing, X-ray diffraction peaks were obtained from powder mixtures of $\text{MoSi}_2/\text{TZ-0Y/TZ-6Y}$ consisting of 80 vol. % MoSi_2 . The volume proportions of TZ-0Y and TZ-6Y phase were: 20:0; 15:5; 10:10; 5:15 and 0:20. X-ray diffraction peaks were obtained from these powder mixtures using a Scintag PAD V diffractometer which was operated in continuous scan mode at 45 kV and 20 mA to give $\text{CuK}\alpha$ radiation. Steps of 0.03 radians in 2θ were employed for values of 2θ between 0° to 90° . The counting time was 90 minutes.

The (111) peak for monoclinic ZrO_2 (111) was chosen because it does not overlap with MoSi_2 or tetragonal ZrO_2 peaks. It also has sufficient intensity for phase analysis. The amounts of monoclinic ZrO_2 were determined from the ratios of the integrated intensities of (111) peaks in the mixtures to those in pure monoclinic ZrO_2 . The values of the integrated intensities were estimated from the areas under (111) monoclinic ZrO_2 peaks using the approximate triangle method [68-72]. The X-ray calibrations for the uniform mixtures were then obtained using the so-called matrix method [73,74] for a mixture consisting of three components, i.e., MoSi_2 , TZ-0Y and TZ-6Y. This yields the following expression for the ratios of the integrated intensities:

$$\frac{I_1}{(I_1)_0} = \frac{\mu_1 x_1}{\sum_{i=1}^3 \mu_i x_i} \quad (2.26)$$

where, I_1 is the integrated intensity of monoclinic zirconia (component 1) in the mixture; $(I_1)_0$ is the integrated intensity of component 1 in the pure state; x_i represents the weight fraction of the i th component; and μ_i is the mass absorption coefficient of the i th component. The weight fraction of monoclinic ZrO_2 is thus given by:

$$x_m = \frac{\mu_t \cdot (1 - x_{ms}) + \mu_{ms} \cdot x_{ms}}{\mu_m - (\mu_m - \mu_t) \cdot \frac{I_m}{(I_m)_0}} \cdot \frac{I_m}{(I_m)_0} \quad (2.27)$$

where, I_m is the integrated intensity of monoclinic ZrO_2 in the mixture; $(I_m)_0$ is the integrated intensity of monoclinic ZrO_2 in the pure state; x represents the weight fraction; and μ is the mass absorption coefficient. Subscripts m , t and ms represent monoclinic ZrO_2 , tetragonal ZrO_2 and MoSi_2 , respectively. For $\text{CuK } \alpha$ radiation, $\mu_{ms} = 123.83$, $\mu_m (\text{TZ-0Y}) = 104.1$ and $\mu_t (\text{TZ-6Y})$. A linear relationship between the weight fraction of monoclinic ZrO_2 and the relative integrated intensity of monoclinic ZrO_2 can thus be obtained. This is given by:

$$x_m \approx \frac{\mu_t \cdot (1 - x_{ms}) + \mu_{ms} \cdot x_{ms}}{\mu_m} \cdot \frac{I_m}{(I_m)_0} \quad (2.28)$$

The maximum error due to above approximation is less than 0.1% [74]. The calibration curve described by Equation (2.28) can therefore be used to obtain accurate estimates of the bulk fractions of monoclinic zirconia phase in the HIPed TZ-0Y, TZ-2Y, TZ-4Y and TZ-6Y composites. Differences between the bulk levels of monoclinic zirconia phase and the volume fractions of monoclinic zirconia phase with the transformation zones may also be used to infer the volume fractions of monoclinic phase produced as a result of stress-induced martensitic transformations.

2.3.3 Laser Raman Spectroscopy

Laser Raman spectroscopy (LRS) analysis was also performed on the same powder mixtures that were used to obtain the X-ray calibrations. The LSR analysis was performed by SPEX Industries, Edison, NJ, using a Raman 500 microprobe under the following conditions: 488 nm laser excitation, 100 mW of power at the laser head (~10 mW at specimen), 80 X objective,

monochromator entrance width of 100 μm , and a probe diameter of $\sim 1 \mu\text{m}$. The typical time for spectra collection was approximately 4 minutes. Since the actual amounts of monoclinic and tetragonal zirconia phase in the different powder mixtures and HIPed compacts were known from the previous X-ray analysis, it was relatively easy to obtain a calibration curve for the estimation of the volume fraction of monoclinic zirconia phase. Intensity ratios of the Raman shifts/peaks (192 cm^{-1} for the monoclinic phase and 264 cm^{-1} for the tetragonal phase) were used to obtain the LSR calibration.

LSR analysis was also conducted on the HIPed compacts of the different composites to determine the bulk levels of tetragonal and monoclinic phase after HIPing. The LSR analysis revealed that the TZ-0Y was fully monoclinic (unstabilized), while the TZ-4Y and TZ-6Y composites were fully tetragonal (fully stabilized) at room temperature. Only the TZ-2Y composite contained a mixture of 13 vol. % tetragonal and 7 vol. % monoclinic phases. The LSR analysis therefore revealed that the HIPed compacts of the TZ-2Y, TZ-4Y and TZ-6Y composites had the potential to undergo stress-induced martensitic transformations from tetragonal to monoclinic phase during subsequent mechanical loading at room temperature. However, the occurrence of such transformations in reality will depend on whether the critical transformation stress is less than the fracture stress of the composites. No stress-induced transformations were expected in the TZ-0Y composite which contained no tetragonal phase that could undergo stress-induced transformations. The effects of stress-induced transformations on fracture toughness will be discussed later.

2.3.4 Mechanical Properties

Compression tests were performed on 6 mm long specimens with rectangular cross sections (6 mm \times 3 mm) using a servohydraulic test machine. The specimens were fabricated by electro-discharge machining prior to testing under compression loading with silicon carbide rams at a strain rate of $5 \times 10^{-4} \text{ s}^{-1}$. Compression tests were carried out in air at 1000, 1200, 1300 and 1400°C. The specimens were soaked at temperature for 30 minutes prior to testing at elevated temperature. The specimens were loaded to final strains between 5 and 10%, and the 0.2 % offset yield stresses were determined for specimens that were not crushed during monotonic loading to the above strain levels. Fracture/rupture stresses were determined from specimens that were crushed before the onset of a 0.2% offset yield stress.

Fracture toughness tests were also performed under three-point bend (with an inner span 12.7 mm) in air at room temperature using single edge notched (SEN) bend bars with square (6.35 mm \times 6.35 mm) cross sections. Notches of 1.9 mm in depth were produced by electro-discharge machining (EDM). Prior to the fracture testing, the side surfaces of the SEN specimens were ground with emery paper and diamond polished to a surface finish of 1 μm . This was done to

facilitate subsequent analysis of the transformation zone by laser Raman microscopy [49,50] and interference microscopy techniques [49,50]. The fracture toughness tests were conducted under load control, in accordance with ASTM-E399 specifications [75]. The specimens were loaded monotonically to failure at a loading rate that corresponded to a stress intensity increase rate of $0.92 \text{ MPa}\sqrt{\text{m}}\cdot\text{s}^{-1}$ at the crack-tip. The failure loads were obtained from an automated data acquisition system, and used to calculate the fracture toughness by substitution into the equation provided by ASTM-E399 code [75]. The fracture mechanisms in the different composites were studied using scanning electron microscopy techniques.

2.3.5 Transformation Zone Analysis

After fracture testing, laser Raman spectroscopy analysis was performed on the sides of the fractured specimens to determine the volume fraction of monoclinic/tetragonal phase as a function of distance from the crack faces. The Raman spectroscopy examination was performed by SPEX Industries, Inc., Edison, NJ, using a Raman 500 microprobe under the same conditions that were used to obtain the LRS calibrations. The volume fractions of monoclinic phase obtained from a calibration obtained under the following conditions: 488 nm laser excitation, 100 mW of power at the laser head ($\sim 10 \text{ mW}$ at specimen), 80 X objective, monochromator entrance width of $100 \mu\text{m}$, and a probe diameter of $\sim 1 \mu\text{m}$. The typical time for spectra collection was approximately 4 minutes. A calibration was developed using the five powder mixtures similar to those employed in the X-ray calibration. Intensity ratios of the Raman shifts/peaks (192 cm^{-1} for the monoclinic phase and 264 cm^{-1} for the tetragonal phase) were used for the calibrations of Raman spectroscopy data. These were used subsequently to estimate the monoclinic phase volume fractions in the HIPed composites prior to fracture toughness testing.

Raman spectroscopy was also conducted on the polished sides of the SEN specimens near the fracture surface. The laser Raman spectroscopy analysis was performed at various distances from the fracture surface (up to $500 \mu\text{m}$) to reveal the variations in the monoclinic and tetragonal zirconia phase fractions. From these variations, the sizes of the transformation zone was estimated to be equal to the distance from the crack face to the point where the volume fraction of monoclinic phase was equal to that in the bulk. Polynomial expressions that relate the variation in the volume fraction of monoclinic phase to the distance from the crack face, i.e., $f(x)$ in Equation 2.3, were thus obtained by standard curve-fitting techniques. These polynomial expressions and the measured transformation zone height are important in the estimation of the level of transformation toughening.

Optical interference microscopy techniques were also used to obtain independent checks of the transformation zone dimensions around the cracks in the fractured specimens. The zones were examined using a Zeiss interference microscope. Interference phenomena produced by a

monochromatic green light from a thallium light source, resulted in fringes on the sides of the specimens (near the fracture surface) when the fracture stresses were sufficient to induce the transformation from tetragonal-to-monoclinic phase. The heights of the transformation zones were determined by identifying the points where the parallel fringe lines in the elastic regions, or the polished flat surfaces outside the transformation zones, deviated from linearity. The deviation is caused by topographical changes that occur in the highly stressed regions within the transformation zones, where a volume increase of the transformed particles occurs as a result of stress-induced martensitic transformations. Further details of the optical interference technique are given in a recent paper by Soboyejo and Mercer [76].

2.4. RESULTS AND DISCUSSION

2.4.1 Microstructure

Optical micrographs that show the microstructures of the resulting materials are presented in Figures 2.3a-2.3d. These show that the zirconia grains were present mainly at the grain boundaries of the MoSi₂ grains. This is because the 0.7 μm diameter zirconia particles were much smaller than the 44 μm average diameter MoSi₂ particles that were used to fabricate the different composites. The zirconia particles were therefore distributed within the interstices between the MoSi₂ powders after phase blending. Nevertheless, the resulting distributions of zirconia grains within the TZ-0Y and TZ-2Y composites were more contiguous than those obtained from the TZ-4Y and TZ-6Y composites (Figures 2.3a-2.3d). Reasons for the differences between the continuity/contiguity of the zirconia reinforcements in the composites are unknown at present.

The transmission electron microscopy (TEM) examination also revealed some significant differences between the microstructures and substructures of the zirconia-reinforced composites (Figures 2.4a-2.4d). The TZ-0Y composite (Fig. 2.4a and 2.4b) has very low dislocation density, and there is very little evidence of interfacial dislocation emission from the interface in this composite. Also, no obvious evidence of matrix microcracking was observed in this composite after fabrication. This will be shown later to be consistent with average compressive residual stresses in the TZ-0Y composite. However, unlike the TZ-0Y composite, a high density of dislocations and microcracks were observed during the TEM analysis of the other composites. This is illustrated in Figures 2.4c and 2.4d for the TZ-2Y and TZ-4Y composites. The figures show clear evidence of matrix microcracking and the formation of tangled dislocation networks after dislocation emission from the reinforcement/matrix interfaces.

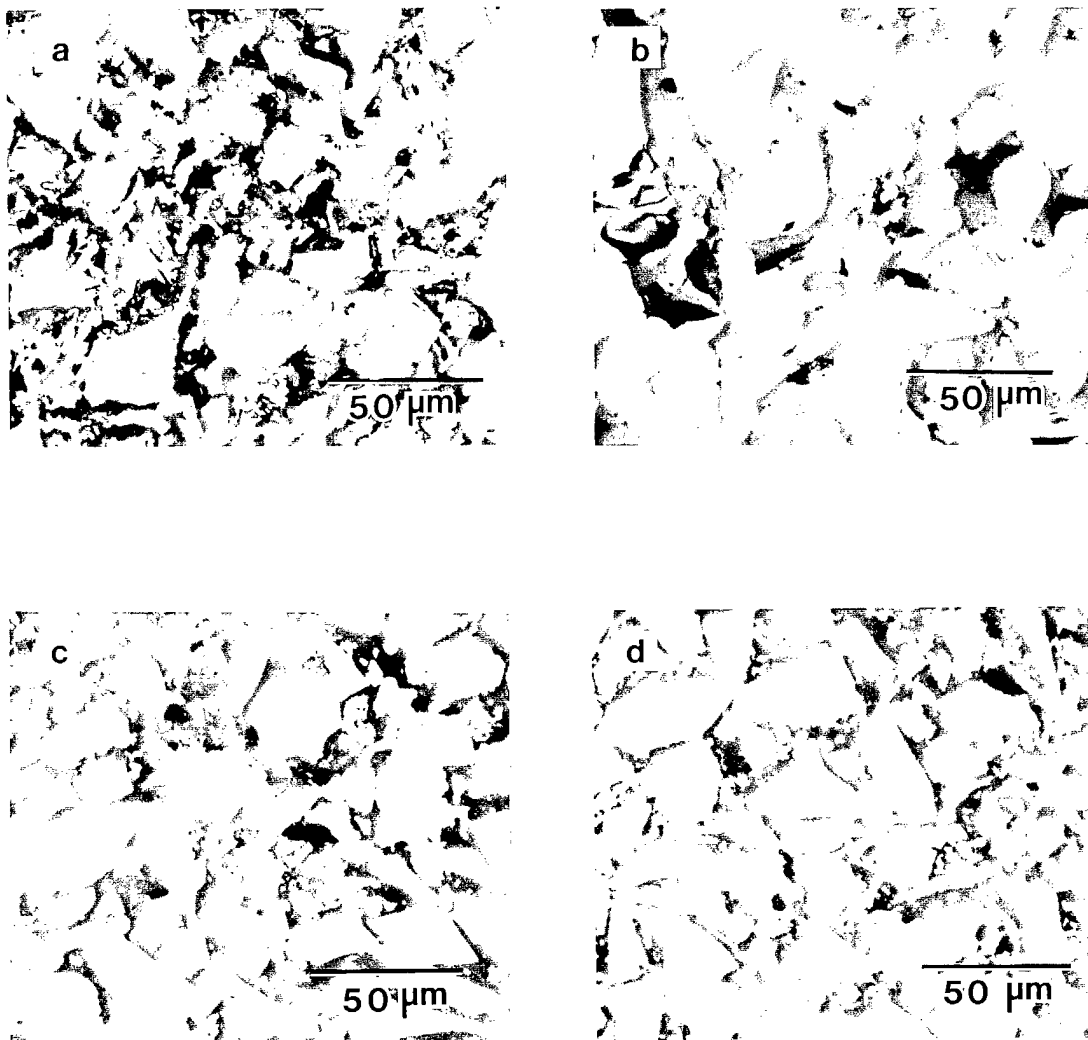


Figure 2.3 Optical Micrographs of MoSi₂/PSZ Composites
(a) TZ-0Y, (b) TZ-2Y, (c) TZ-4Y and (d) TZ-6Y

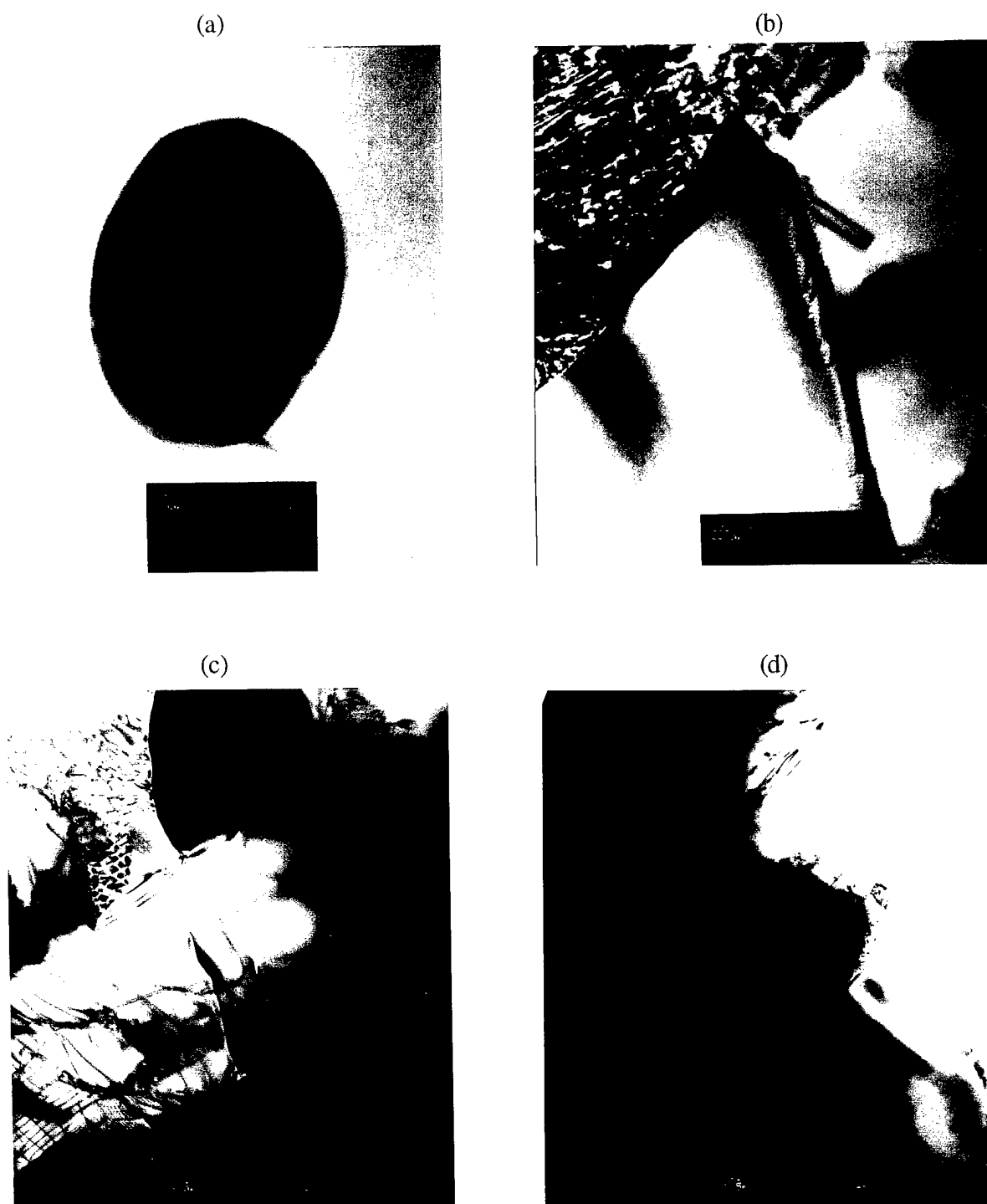


Figure 2.4 Transmission Electron Micrographs of MoSi₂/PSZ Composites
(a) TZ-0Y, (b) TZ-0Y, (c) TZ-2Y and (d) TZ-4Y

The high density of microcracks and dislocations will be shown, in subsequent sections, to be due to the effects of higher tensile residual stresses that develop in these composites during cooling from the processing temperature. Also, the low densities of dislocations and the absence of matrix cracks in the TZ-OY composites will be shown to be due to moderate compressive residual stresses that develop in these composites during processing. For now, it is simply sufficient to note that the relatively high matrix dislocation densities can only occur during dislocation emission at/or above the ductile-to-brittle transition temperature where easy glide of dislocations is possible in MoSi_2 [77]. The occurrence of matrix cracking may also promote microcrack shielding/anti-shielding, depending on the spatial configurations of the cracks with respect to the dominant crack-tips [78-80]. Further discussion on toughening mechanisms will be presented later.

2.4.2 X-ray Calibration

The experimentally determined X-ray intensity ratios of monoclinic zirconia in the powder mixtures to those of monoclinic zirconia in the pure state are plotted against the monoclinic zirconia composition (in wt. %) in Figure 2.5a. This figure shows an almost linear variation in intensity ratio with increasing monoclinic phase fraction. The results are similar to those reported by Marshall et al. [50] for monolithic zirconia ceramics consisting of tetragonal and monoclinic phases. However, the calibrations obtained from the "monolithic" zirconia mixtures of tetragonal and monoclinic phases are somewhat different from those presented in Figure 2.5a for the MoSi_2 /zirconia powder mixtures. The differences are attributed to the different X-ray adsorption characteristics of the "monolithic" and "composite" systems.

The monoclinic zirconia content predicted by the calibration curve shown in Figure 5a, is compared with theoretical predictions (obtained from Equation 2.28) in Figure 2.5b. Good agreement was observed between the actual/experimental and estimated/theoretical monoclinic zirconia content in the powder mixtures. The experimental calibration curve was therefore used to estimate the phase fractions of monoclinic phase in hot isostatically pressed MoSi_2 /zirconia composites with the different levels of yttria stabilization. The estimates of the monoclinic zirconia volume fractions obtained from the experimental calibration curve (Figure 2.5a) are presented in Table 2.2. The TZ-0Y composites were fully monoclinic, as expected for pure unstabilized zirconia [49]. However, the TZ-4Y and TZ-6Y composites remained fully tetragonal at room temperature, presumably because they were fully stabilized by the yttria additions. The TZ-2Y composite contained 7 vol. % monoclinic phase and 13% tetragonal phase. It was therefore apparent that only about 13 vol. % of the 20 vol. % of TZ-2Y composite had the potential to undergo stress-induced phase transformations from the tetragonal to the monoclinic phase. Further discussion of transformation toughening will be presented later.

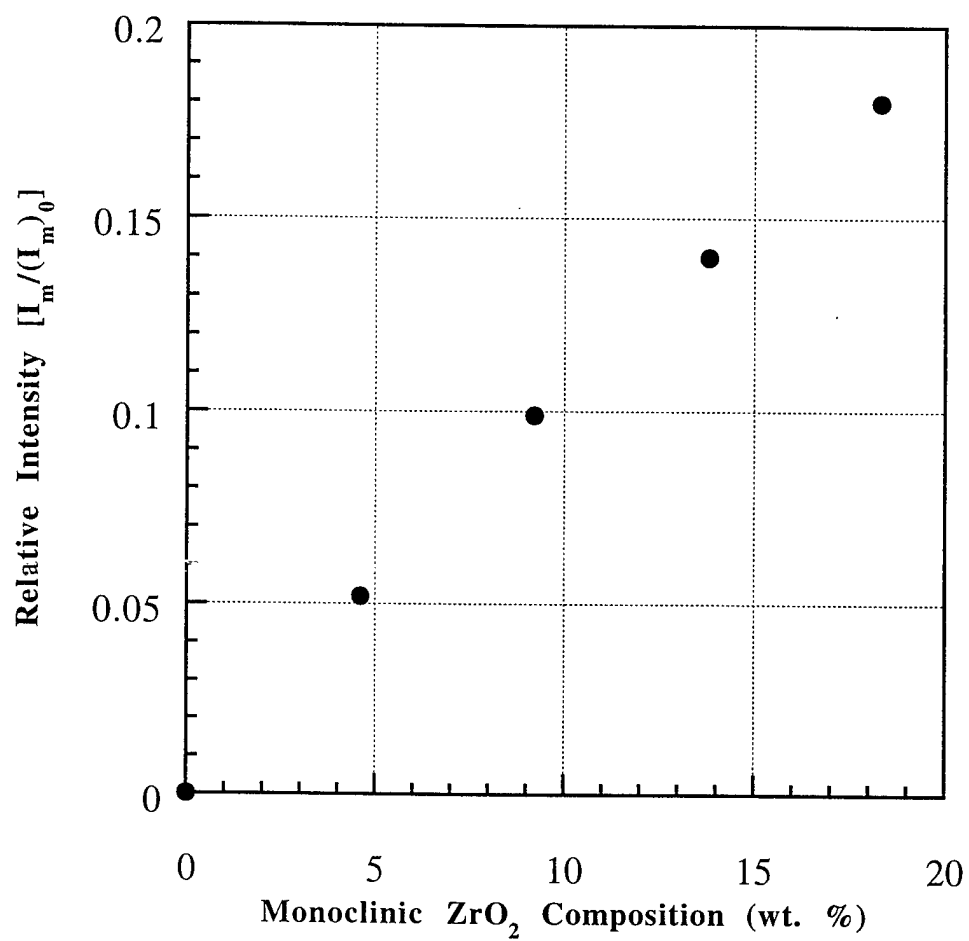


Figure 2.5 X-ray Diffraction Calibration
(a) Plot of Intensity Ratio versus Volume Fraction of Monoclinic Phase

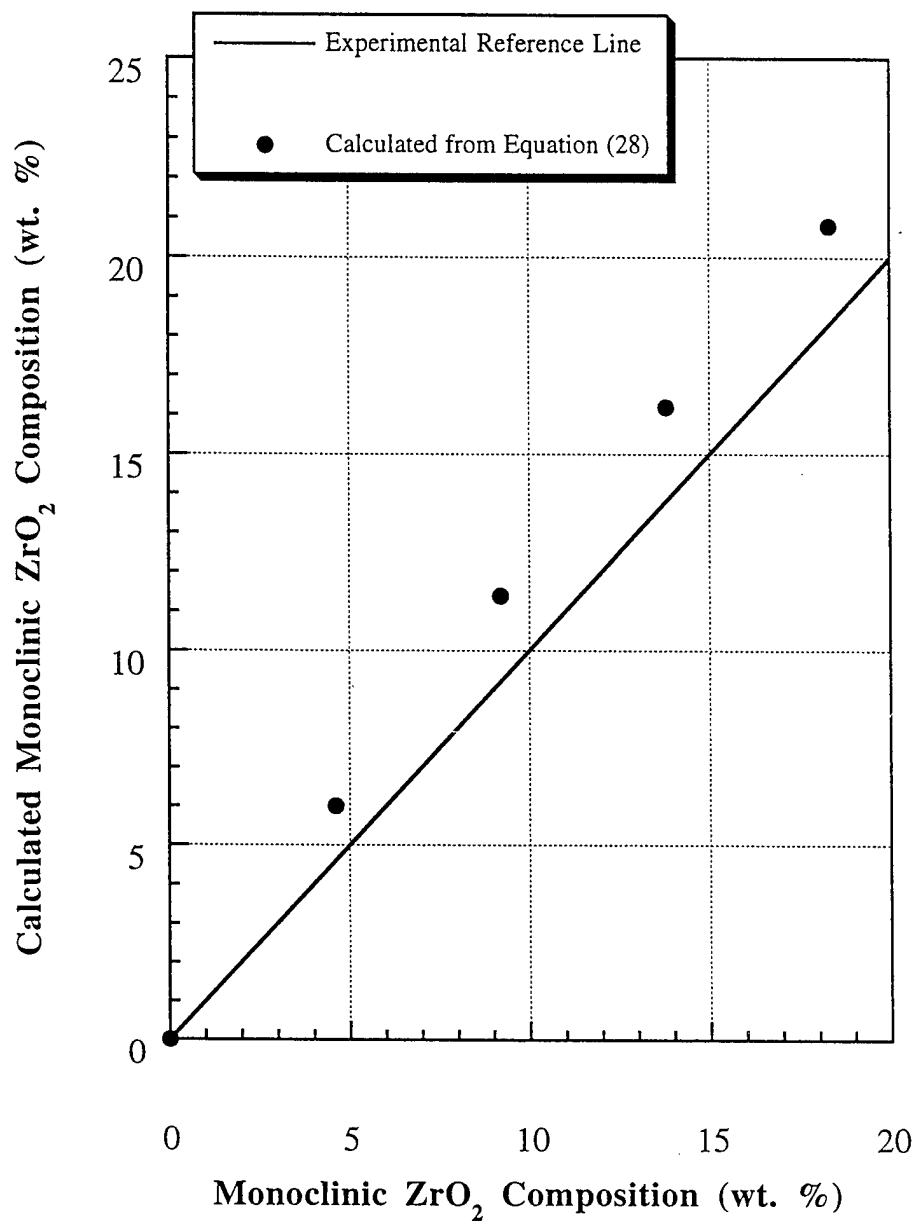


Figure 2.5 X-ray Diffraction Calibration
(b) Comparison of Predicted and Actual Monoclinic Phase Content

Table 2.2 Summary of Mechanical Properties

(a) Compressive Strengths of ZrO_2 Particle Reinforced $MoSi_2$ Composites

| Temperature (°C) | Materials | | | | |
|---------------------|-----------|----------------|----------------|----------------|----------------|
| | $MoSi_2$ | $MoSi_2/TZ-0Y$ | $MoSi_2/TZ-2Y$ | $MoSi_2/TZ-4Y$ | $MoSi_2/TZ-6Y$ |
| 1000 | 663 * | 835 | 665 * | 597 * | 712 * |
| 1200 | 484 | 485 | 336 | 410 | 374 |
| 1300 | 368 | 332 | 300 | 314 | 297 |
| 1400 | 285 | 108 | ----- | 157 | ----- |

(b) Measured Fracture Toughness of PSZ Reinforced $MoSi_2$ Composites

| Materials | $MoSi_2$ | $MoSi_2+TZ-0Y$ | $MoSi_2+TZ-2Y$ | $MoSi_2+TZ-4Y$ | $MoSi_2+TZ-6Y$ |
|-------------------------------|----------|----------------|----------------|----------------|----------------|
| K_{IC} ($MPa\sqrt{m}$) | 3.8 | 5.7 | 5.0 | 5.5 | 4.8 |

Finally in this section, it is of interest to compare the errors in the calibrations obtained from this study (Figure 2.5) with those reported by Garvie and Nicholson [68] for unreinforced CaO stabilized zirconia. Using the matrix method, they calculated the proportions of monoclinic ZrO_2 from the ratios of $I_{\text{m}(111)}$ to $(I_{\text{m}(111)})_0$ in the CaO- ZrO_2 system. The errors corresponding to 11.1 wt. % and 21.9 wt. % were 17.1% and 16.0 %, respectively . In the present study, the errors corresponding to 9.2 wt. % and 18.3 wt. % of monoclinic ZrO_2 were 19.3 % and 12.0 %. Also, the accuracy of the calibrations increase with increasing volume fraction of monoclinic ZrO_2 . This is because the integrated X-ray intensity at a higher volume fraction of monoclinic ZrO_2 phase can be measured with greater accuracy than that of a smaller volume fraction of monoclinic phase. The lower accuracies in the volume fraction estimates obtained from the powder mixtures with smaller monoclinic zirconia phase content are attributed mainly to higher signal-to-noise ratios in these materials.

2.4.3 Laser Raman Spectroscopy

The LRS calibration curve obtained from the different MoSi_2 /zirconia powder mixtures is shown in Figure 2.6. The calibration curve is almost linear, consistent with previous reports in the literature for other zirconia-reinforced systems [50]. The small differences between the MoSi_2 /zirconia calibration curve and those obtained from other systems are attributed to the effects of the MoSi_2 matrix (which is also Raman active) on the laser beam. In any case, the calibration curve shown in Figure 2.6 was used to estimate the bulk volume fraction of monoclinic phase in the TZ-2Y composite. The latter was the only composite in which tetragonal and monoclinic phases were both detected. The TZ-2Y composite was thus shown to consist of approx. 13 vol. % tetragonal phase and 7 vol. % monoclinic phase after HIPing.

2.4.4 Residual Stress

The predicted relationships between the effective coefficient (Equation 2.23) and particle volume fraction are shown in Figure 2.7a for various configurations with n between 3 and infinity. Note that $\sigma_0 = (\sigma_0)_i$ in Equation 2.23 when n is infinite. This is because the coefficient γ in Equation 2.23 approaches 1 when n is infinite. A linear relationship is thus obtained between the effective coefficient and the volume fraction of particulate phase. This is a happy result since the limiting condition corresponding to an infinite value of n provides the best unit cell idealization of most particulate composites. It is also important to note here that the effective coefficient approaches 1 for all possible values of n , when the reinforcement volume fraction approaches 0. The results presented in Figure 2.7a are consistent with the classical Selsing model [65] when $V_f \rightarrow 0$. This is encouraging because the model by Selsing was

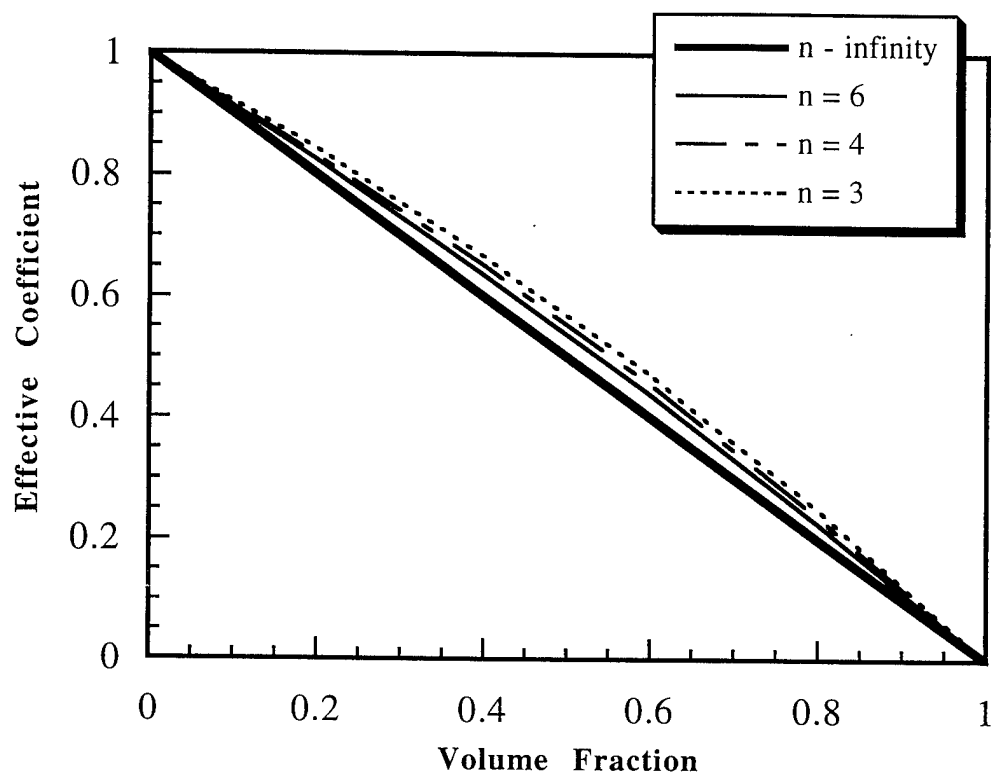


Figure 2.6 (a) Plots of Effective Coefficient versus Particle Volume Fraction

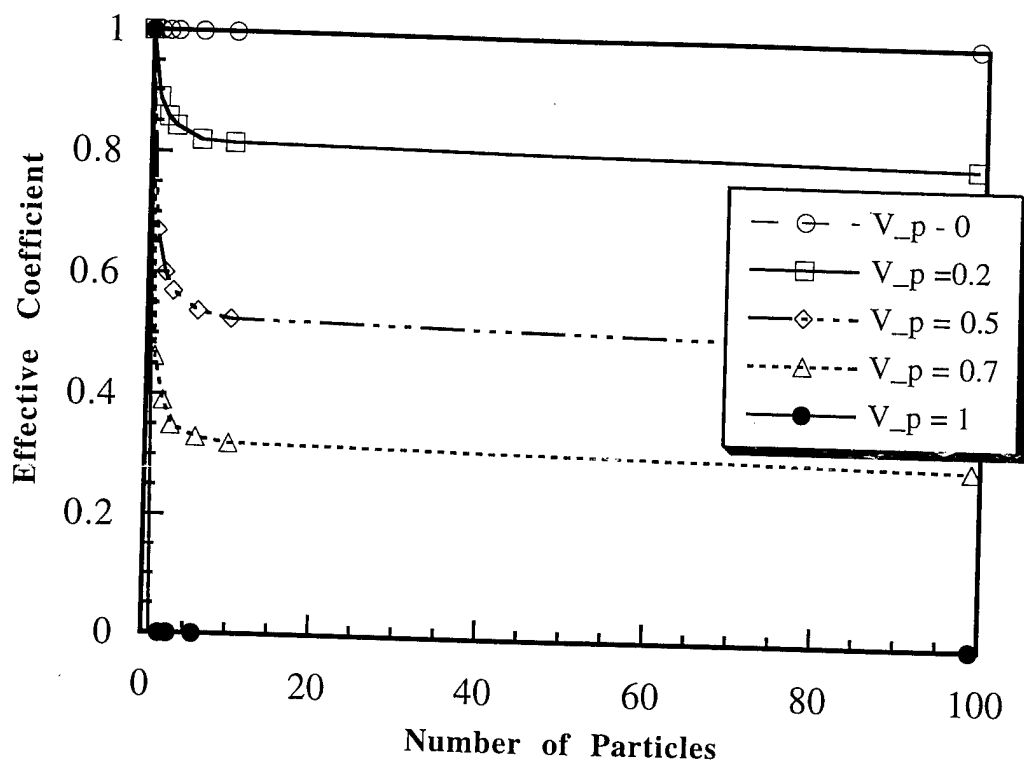


Figure 2.6 (b) Plots of Effective Coefficient versus Number of Particles

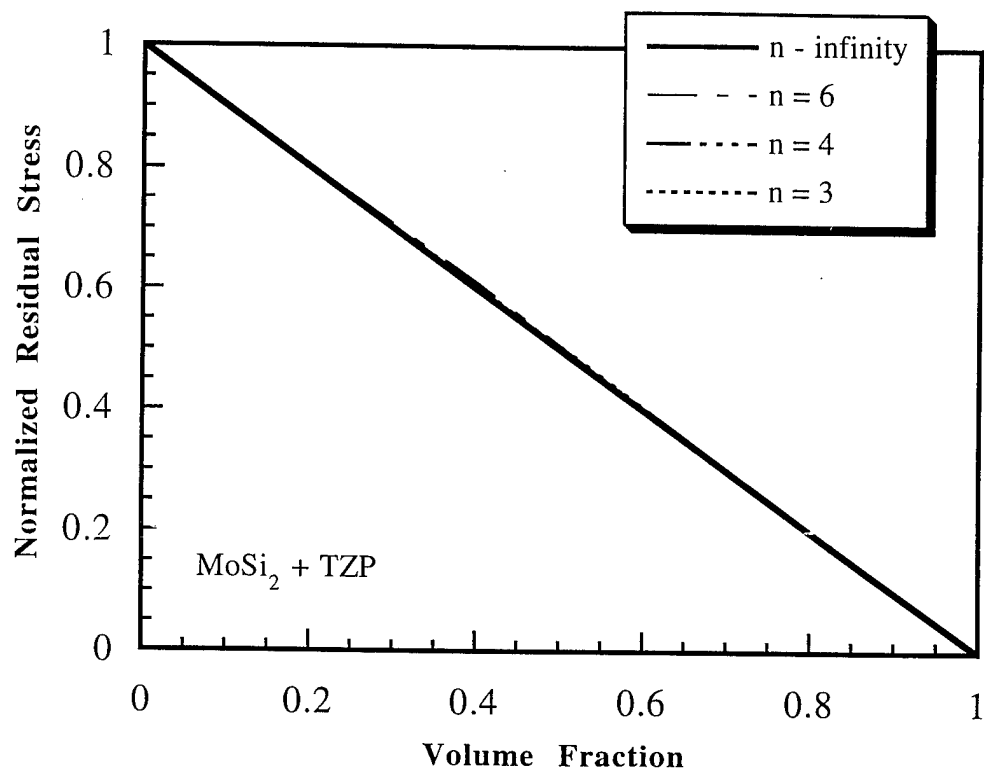


Figure 2.7 Summary of Predicted Residual Stresses
 (a) Plot of Normalized Residual Stress versus Particle Volume Fraction

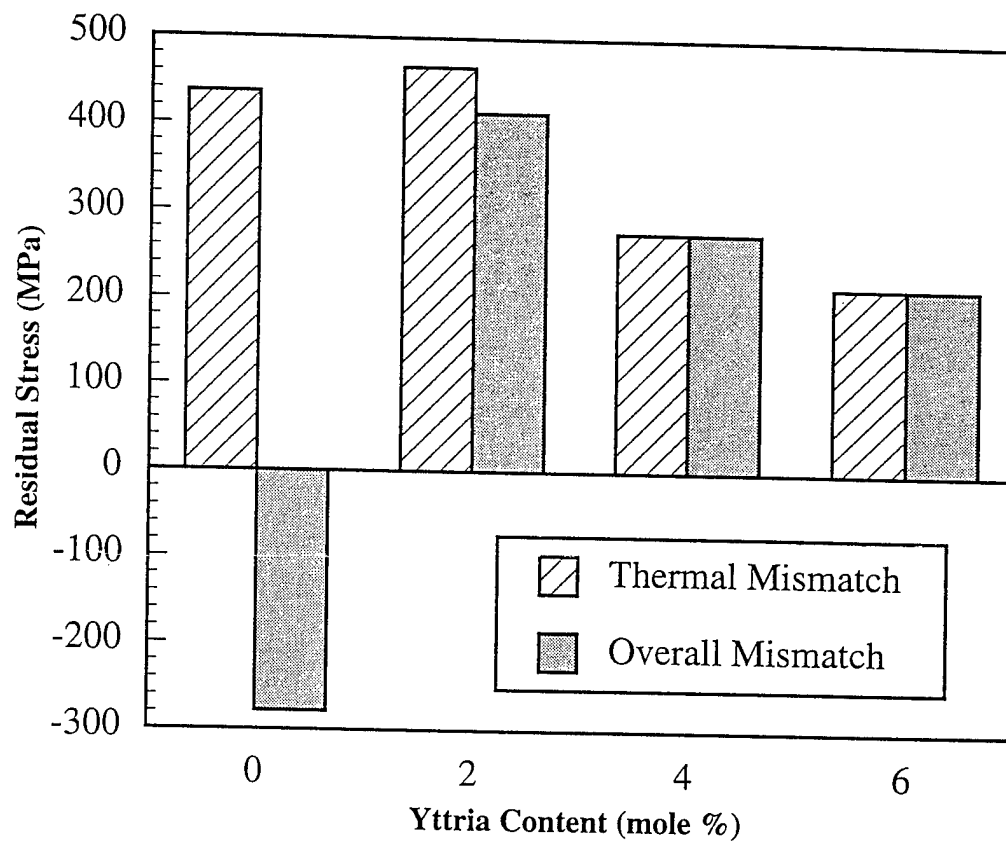


Figure 2.7 Summary of Predicted Residual Stresses
(b) Effect of Yttria Content on Residual Stresses

developed for the prediction of elastic residual stresses in composites with low reinforcement volume fractions, i.e., composites with V_f close to zero. The model considers the residual stresses due to thermal expansion mismatch in which reinforcement interaction/volume fraction effects are neglected.

The current model is therefore in exact agreement with the Selsing model [65] when $V_f \rightarrow 0$. However, increasing differences are observed between the current model and the Selsing model as the reinforcement volume fraction increases. This is shown in Figure 2.7a in which the effective coefficient is shown to decrease continuously as the reinforcement volume fraction increases. The effective coefficients decrease continuously to zero since there is no thermal expansion mismatch at the limiting condition, i.e., when $V_f \rightarrow 1$. The decrease in the effective coefficient with increasing reinforcement volume fraction is of practical importance, especially at high reinforcement volume fractions where the effective coefficients are closer to 0 than 1. Residual stress estimates that are based on the Selsing model ($V_f \rightarrow 1$ in Figure 2.7a) may will therefore overpredict the residual stresses in composites with reinforcement volume fractions that are much greater than zero. Erroneously high residual stresses have been predicted by the Selsing model in such cases [65]. The effective coefficients presented in Figure 2.4a may therefore be used as a correction factor for improving the accuracies of the residual stress estimates in composites with reinforcement volume fractions that are greater than zero.

The relationship between the effective coefficient and the number of randomly distributed particles surrounding any arbitrary particle (shaded particle in Figure 2.2) is shown in Figure 2.7b for various reinforcement volume fractions. In all cases, the effective coefficients decrease rapidly (from the limiting value of 1) to asymptotic values, as the number of particles increases from 1 to 10. For $n > 10$, the effective coefficients are almost constant. Also, the asymptotic values of the effective coefficients decrease from 1 to 0 as the reinforcement volume fractions increase from 0 to 1. The current study therefore shows that approx. 10 particles should be considered for the assessment of the possible interactions between multiple particles. This is important since the computational efforts required for the analysis of multi-particle unit cell configurations may increase significantly with increasing values of n .

An illustration of the importance of the current analysis is provided in Figure 2.7a in which the normalized residual stress, β , estimates obtained for the TZ-2Y composite are presented as a function of reinforcement volume fraction for different values of n between 3 and infinity. The normalized residual stresses that are plotted in this figure represent the ratio between the residual stresses computed from the current model, σ_0 , and those obtained from the Selsing model [65], σ_{r0} , i.e., $\beta = \sigma_0/\sigma_{r0}$. The normalized residual stresses are similar for values of n between 3 and infinity. The asymptotic solutions corresponding $n \rightarrow \infty$ may therefore be used to obtain estimates of the residual mean stress in the in particulate reinforced composites. Also, due to the

linear relationship between the normalized residual stress and the particle volume fraction (Figure 2.7a), and the fact that $\beta \rightarrow 1 - V_p$ as $n \rightarrow \infty$, the average residual stress in the MoSi₂/zirconia composite system is given by:

$$\sigma_0 = (1 - V_p) \cdot \frac{E_m \cdot (\alpha_p - \alpha_m) \cdot \Delta T}{\frac{E_m}{E_p} \cdot (1 - 2V_p) + \frac{1 + \nu_m}{2}} \quad (2.29)$$

Equation (2.29) was used to estimate the residual stresses due to thermal expansion mismatch in the different composite that were examined in this study. The residual stress estimates were obtained using physical, thermal and mechanical properties that are summarized in Table 2.1. The estimated values of the residual stress levels due to thermal expansion mismatch are summarized in Figure 2.7b. Unlike previous 1-2 GPa thermal mismatch residual stress estimates obtained from the modified Selsing model by Becher [51], more realistic values of the thermal mismatch residual stress between 200 and 460 MPa are predicted by the current model. The thermal mismatch stresses are also tensile, consistent with the thermal expansion data presented in Table 2.1. However, the thermal mismatch stresses do not include the possible compressive residual stress components which may be induced as a result of volume changes that occur during phase transformation from tetragonal to monoclinic phase in the TZ-0Y and TZ-2Y composites.

The compressive residual stress component due to the volume expansion of PSZ particles can be predicted using Equation 2.25. Using the Gibb's free energy expression for transformations controlled purely by dilatational strains, the residual stress due to volume expansion can be approximated by the critical transformation stress for an unconstrained volume expansion, σ_C^T , which is estimated to be -1.6 GPa [49]. This value is likely to overestimate the residual stress component due to volume expansion, since it neglects the possible relief of stress that can occur by dislocation emission from the interface (Figures 2.4b-2.4d). An alternative method for the estimation of residual stress was therefore explored. This relied on the combined use of the transformation zone measurements obtained for the TZ-2Y composite, and Equation 2.1 developed by Budiansky and co-workers [55] for the estimation of the transformation zone size. By rearrangement of Equation (1), the critical transformation stress may also be estimated from Equation 2.1 when the transformation zone size is known. From earlier studies, the transformation zone size in the MoSi₂ + TZ-2Y composite has been shown to be approx. 120 μm [49]. Hence, by substituting into Equation 2.1, the residual stress due to the volume expansion that occurs during phase transformation can be estimate from the critical transformation stress, σ_C^T , to be 715 MPa. This calculated value of the critical transformation

stress is comparable to experimentally determined value of -800 and -550 MPa in CeO_2 and MgO stabilized zirconia reported by Chen and co-workers [62-64].

In the case of the TZ-0Y composite, phase transformation occurs at about 1200 °C. This phase transformation results in a volume expansion of about 4% in the PSZ particles. From Equation 2.29, the tensile residual stress developed between the fabrication temperature (1400 °C) and the transformation temperature of 1200 °C is estimated to be approx. 100.0 MPa. Below 1200 °C, there are two components of residual stress: a tensile residual stress component due to thermal expansion mismatch, and compressive residual stress due to the volume expansion of PSZ particles that occurs at the transformation temperature. The tensile residual stress due to the thermal expansion mismatch is approx. 437 MPa after cooling from the fabrication temperature to room temperature. The compressive residual stress that is induced at the transformation stress is estimated from Equation 2.25 to be -715 MPa. The overall residual stress of -278 MPa is therefore given by the sum of these two residual stress components. This compressive stress level will be shown in the next section to be small with respect to the compressive strength of the TZ-0Y composite. This may explain the apparently low levels of damage (dislocations/cracks) that was observed in the TEM images of this materials (Figures 2.4a and 2.4b).

In the case of the TZ-2Y composite, the zirconia particles retain their tetragonal structure from the fabrication temperature (1400 °C) to 920 °C (the transus temperature) where the transformation from tetragonal to monoclinic phase begins. Subsequent X-ray analysis revealed that 65% of the zirconia particles in the bulk were tetragonal at room temperature phase, i.e., a volume fraction of 0.13 in the bulk composite which contains 20 volume percent of reinforcement. The overall residual stress may now be estimated from the thermal mismatch and volumetric expansion components of residual stress, as in the earlier analysis of residual stresses in the TZ-0Y composite. The tensile residual stress induced as a result of thermal expansion mismatch during cooling from the fabrication temperature to room temperature is 460 MPa. The compressive residual stress induced as a result of the volume expansion that occurs during phase transformation is thus estimated from Equation 2.25 to be -56 MPa since only about 7 vol. % of the available 20 vol. % of reinforcement in the composite transforms from tetragonal to monoclinic phase. The overall residual stress in TZ-2Y composite is therefore 414 MPa. This is a relatively high value of tensile residual stress. The high levels of matrix and interfacial damage (dislocations and microcracks) observed in the TZ-2Y composite (Figure 2.4c) may therefore be attributed partly to the effects of high tensile residual stress.

Similarly, the residual stresses are tensile in both the TZ-4Y and TZ-6Y composites. However, no residual stress components are induced as a result of volume expansion during phase transformation in these composites which retain their high temperature tetragonal structure down to room temperature. The overall residual stresses and the thermal mismatch residual

stress values are therefore identical in the TZ-4Y and TZ-6Y composites, as shown in Figure 2.7b. Also, since the residual stresses are tensile in these composites, the matrices in these composites are subjected to considerable levels of damage due to interfacial dislocation emission and matrix cracking phenomena. This is illustrated in Figure 2.4d for the TZ-4Y composite. Note that the dislocation and microcrack densities are much less in this composite than those observed in the TZ-2Y composite where the overall residual stress level is greater (Figure 2.7b). The results obtained from the residual stress analysis therefore appear to be consistent with the visual evidence of matrix and interfacial damage revealed by the TEM analysis (Figures 2.4a-d). Further evidence of the effects of residual stress on compression strength and fracture toughness are presented in the next two sections.

2.4.5 Compression Strength

The 0.2% compressive yield strengths are compared with those obtained for MoSi_2 in Table 2.2. However, compressive rupture strength data is presented for the compression specimens that were crushed before a strain of 0.2% was reached. The data obtained from these specimens are marked with asterisks in Table 2.2. At 1000°C, the TZ-0Y composite has a much higher compressive strength than all the other materials that were examined in this study. This is attributed to the moderate compressive residual stress (approx. -715 MPa) that is induced in this composite due to the volume change that occurs during phase transformation at approx. 1200°C [81]. Similar improvements in compression strength are not observed in the TZ-2Y composite, the other composite which also undergoes a phase transformation during cooling. However, a much lower compressive residual stress (approx. -56 MPa) is induced in this composite after phase transformation from tetragonal to monoclinic phase.

At 1200 and 1300°C, the different composites have comparable strengths to monolithic MoSi_2 which was tested as a "control" material. This, again, is consistent with the residual stress arguments proposed earlier. The residual stresses are much lower at these temperatures which are above the phase transformation temperatures for the different composites [81]. There are, therefore, no residual stresses induced as a result of phase transformations. Also, the thermal residual stresses induced as a result of thermal expansion mismatch during prior cooling to room temperature may be relaxed during thermal exposure at 1200 and 1300°C. The overall levels of residual stress in the different composites should therefore be very small at 1200 and 1300°C, and the composite strengths should be comparable to those of monolithic MoSi_2 in this temperature regime.

Residual stress arguments can also be used to explain the similarities between the compression strengths of the different composites that were tested at 1400°C. Since the composites were processed at this temperature, the thermal mismatch stresses should be

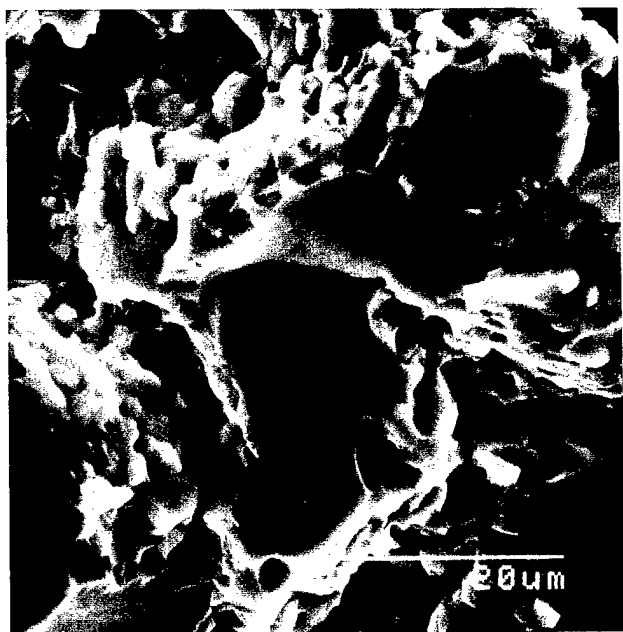
completely relaxed at this temperature. However, the zirconia-reinforced composites are much weaker than monolithic MoSi_2 at this temperature, presumably as a result of the relatively low (when compared to monolithic MoSi_2) strengths of the zirconia particles. Finally in this section, it is of interest to note here that the ductile-to-brittle-transition-temperature (DBTT) was approx. 1300°C in all the different materials. The DBTT is defined in this study, as the temperature at which the upper shelf strength of the material (at 1000°C) is reduced by a factor of about one half. The measured DBTT is therefore comparable to values reported in previous studies by Soboyejo et al. [21,24] on monolithic and ductile phase reinforced MoSi_2 . However, the zirconia reinforced composites do not have the same inherent oxidation problems as the ductile phase reinforced composites at elevated temperature.

2.4.6 Fracture and Toughening Mechanisms

Fracture in the different composites occurred predominantly by cleavage of the MoSi_2 matrix and intergranular fracture of the zirconia particles, as shown in Figures 2.8a-d. However, some evidence of secondary cracking was observed, especially in the TZ-4Y and TZ-6Y composites (Figures 2.8c and d). The fracture toughness values obtained for the different composites are compared with those obtained for monolithic MoSi_2 in Table 2.3. Since the amount of material available for testing was very limited, the values of K_{Q} listed in Table 2.3 are average numbers from duplicate tests. The error ranges shown in Table 2.3 therefore correspond only to deviations from the mean of two data points. Nevertheless, the data shows clearly that the fracture toughness of MoSi_2 is improved by the addition of zirconia particles, although the degree of toughening was very limited in all the composites. The highest level of toughening was obtained from the TZ-0Y composite which had a fracture toughness of $5.7 \text{ MPa}\sqrt{\text{m}}$ compared to a matrix toughness of $3.8 \text{ MPa}\sqrt{\text{m}}$. However, this composite did not undergo transformation toughening since all the high temperature tetragonal phase transformed to monoclinic phase during cooling from the processing temperature. Similarly, transformation toughening was not observed in the TZ-4Y and TZ-6Y composites, although their fracture toughness values were higher than those of the matrix. Possible toughening mechanisms in these materials will be identified later after a discussion of transformation toughening in the TZ-2Y composite.

The Raman spectroscopy analysis of the sides of the TZ-2Y fracture specimen revealed an increase in the volume fraction of monoclinic phase from bulk average values (away from the fracture surface) to higher levels within the transformation zone. A typical plot of the volume fraction of monoclinic phase against distance from the crack face is presented in Figure 2.9. This shows that the maximum volume fraction of monoclinic phase occurs in the region that is closest to the fracture surface. A discernible drop in the volume fraction of monoclinic phase is then

(a)



(b)



(c)



(d)

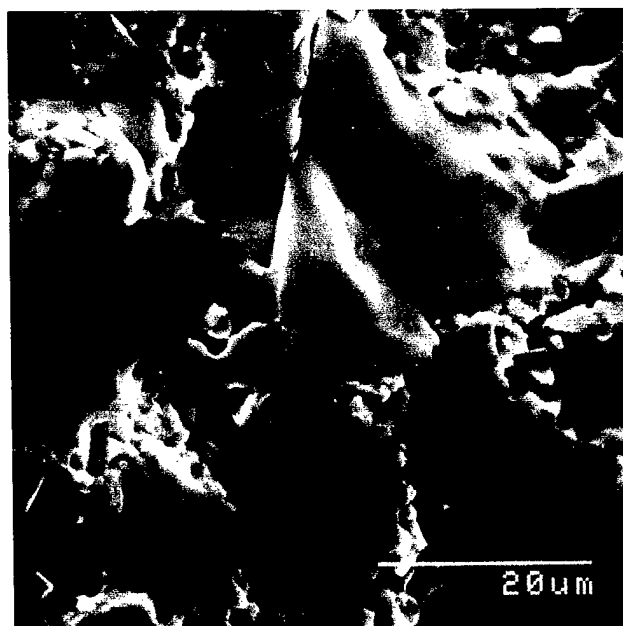


Figure 2.8 Typical Fracture Surface Morphologies of Fracture Toughness Specimens
(a) TZ-0Y and (b) TZ-2Y (c) TZ-4Y (d) TZ-6Y

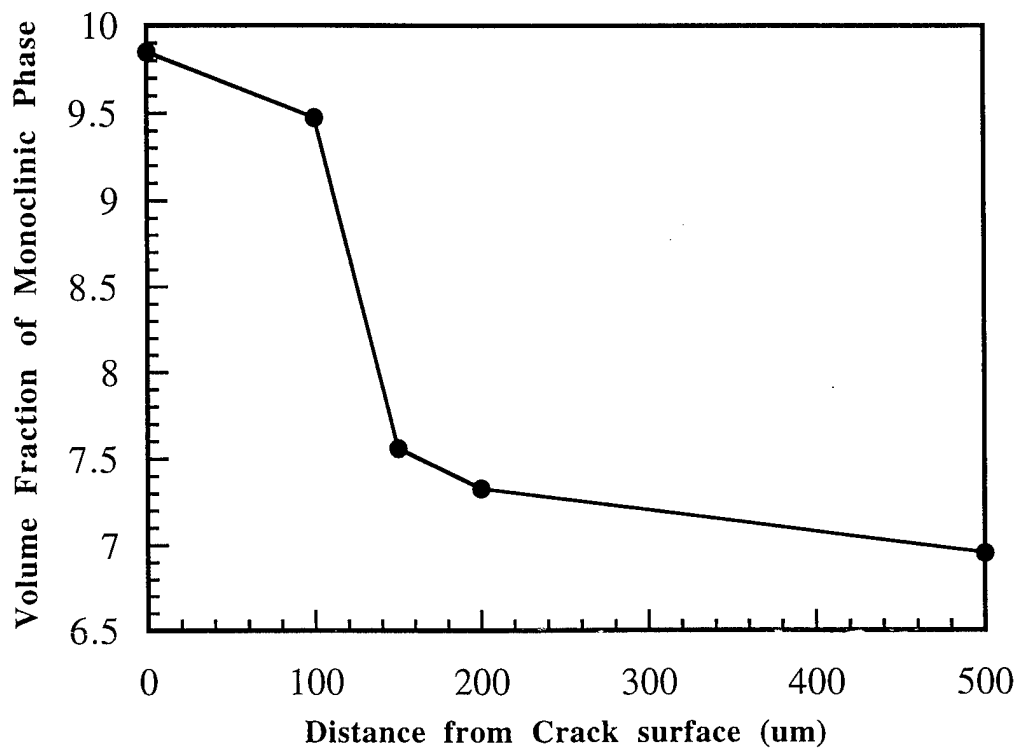


Figure 2.9 Volume Fraction of Monoclinic Zirconia as a Function of Distance from the Crack-Tip in MoSi₂ + 20 vol. % TZ-2Y Composite

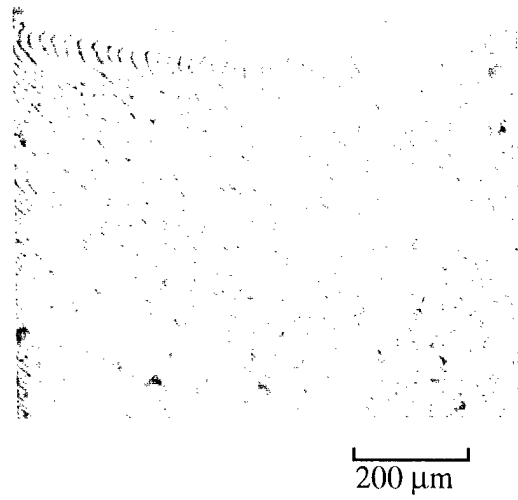
observed with increasing distance from the crack face, presumably as a result of lower stress concentrations. The volume fraction of monoclinic phase reduces to an asymptotic value that corresponds to the average volume fraction of monoclinic phase in the bulk. This occurs at a distance of approximately 120-125 μm from the fracture surface, which is consistent with the zone size inferred from the points where the optical interference fringes deviate from linearity (Figures 2.10a). The optical interference transformation zone size measurements are therefore in good agreement with those obtained from the LRS analysis (120 μm) of the TZ-2Y specimen.

The volume fraction of monoclinic phase is therefore not constant, as is often assumed in many of the studies on transformation toughening [61-64]. There is therefore a need to estimate the average volume fraction of transformed tetragonal zirconia within the transformation zone. This was estimated by subtracting the bulk average monoclinic zirconia levels from those within the transformation zone. The average amount of monoclinic zirconia in the transformation zone was thus estimated by integration to be approx. 3 vol. %. The degree of transformation toughening may thus be estimated to be $1.2 \text{ MPa}\sqrt{\text{m}}$ by substitution of V_t and h into the Equation 2.2. Other parameters required for the estimation of the level of transformation toughening are listed in Table 2.1. Hence, for a matrix toughness of approx. $3.8 \text{ MPa}\sqrt{\text{m}}$, the fracture toughness of the TZ-2Y composite is estimated to be approx. $5.0 \text{ MPa}\sqrt{\text{m}}$. This is in exact agreement with the fracture toughness data obtained from the experimental fracture toughness measurements.

The model by Budiansky et al. [55] therefore appears to provide very good estimates of the degree of transformation toughening in the TZ-2Y composite. This is in spite of the fact that it neglects to effects of shear in its formulation, i.e., it assumes that the transformations are induced purely by dilatational stresses. Similar agreement between theoretical estimates obtained from the analysis of Budiansky et al. [55] and measured fracture toughness values have also been obtained by Marshall et al. [51] in recent studies on transformation toughened ceramics. The role of shear stresses in the stress-induced martensitic transformation processes therefore appear to be relatively small. However, shear stresses may become important when unsymmetric deformation-induced twinning mechanisms occur along with the stress-induced phase changes [55,58]. Such twinning phenomena were not observed in the composites that were examined in this study (Figures 2.3 and 2.4).

Finally in this section, it is important to consider the possible toughening mechanisms in the composites that did not undergo transformation toughening, i.e., the TZ-0Y, TZ-4Y and TZ-6Y composites. The optical interference fringes do not deviate from linearity in these composites. This is illustrated in Figure 2.10b, in which the fringes on the side of a TZ-4Y fracture specimen are shown to remain linear even in the vicinity of the fracture surface. The other shielding mechanisms that may play a role include crack deflection and microcrack shielding. The role of crack deflection is not considered here since it has been shown in previous work [49] to result

(a)



(b)

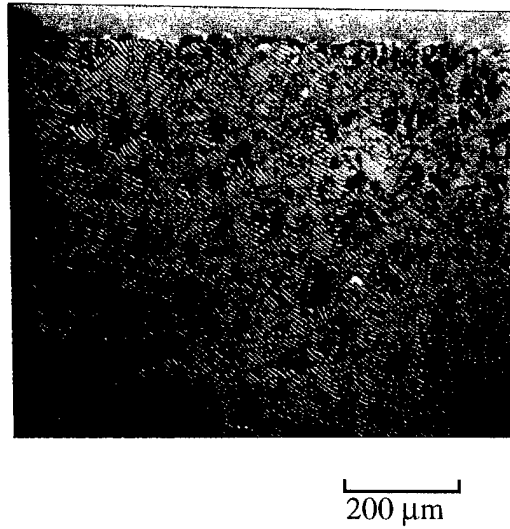


Figure 2.10 Typical Optical Interference Micrograph Showing Fringes Near the Fracture Surfaces of (a) TZ-2Y Composite; (b) TZ-4Y

only in very small improvements in the fracture toughness of $\text{MoSi}_2/\text{zirconia}$ composites (approx. $0.1 \text{ MPa}\sqrt{\text{m}}$ in all the composites examined in this study). The current discussion will therefore focus on shielding/anti-shielding effects due to microcracking and residual stress distributions.

Microcrack shielding/anti-shielding mechanisms may affect the fracture toughness values in the different composites [78-80]. Evidence of microcracking was obtained from the TEM photomicrographs which showed fine microcrack distributions within the MoSi_2 matrix of the TZ-2Y, TZ-4Y and TZ-6Y composites after processing (Figures 2.4c and 2.4d). Such microcracks were not observed in the TZ-0Y composite, and the dislocation density was very low in the latter (Figures 2.4a and 2.4b), i.e., the levels of imperfections were lower in the TZ-0Y composites. Secondary cracks were also observed on the fracture surfaces of the TZ-2Y, TZ-4Y and TZ-6Y composite specimen (Figures 2.4b-d). However, detailed micromechanics analyses of the microcrack shielding/anti-shielding components is not possible at present since the precise nature of the distributions of microcracks with respect to the dominant crack orientation is known. Nevertheless, it is important to note that previous work on similar brittle matrix composites [29,30] have shown that the toughening contributions from microcrack shielding/anti-shielding are generally small (generally less than 25%). However, such toughening levels may be sufficient to account for the higher fracture toughness values of the TZ-4Y and TZ-6Y, two composites in which significant levels of microcracking were observed (Figures 2.4 and 2.8).

Since microcracks were not generally observed in the TZ-0Y composite, the most probable cause of toughening in this material is shielding due to compressive residual stress (Figure 2.7b). The overall effects of compressive residual stress on crack-tip stresses are difficult to quantify. However, it is clear that the compressive residual stresses in the TZ-0Y composite may reduce the effective crack-tip stresses. The overall tensile residual stresses in the other composites may also promote anti-shielding effects. The residual stress levels may also affect the critical stress levels and energies required for transformation (Equation 2.25) [60]. However, the energy change associated with transformation may also vary significantly with the degree of yttria stabilization. Hence, in the case of the TZ-4Y and TZ-6Y composites, the critical transformation stresses are apparently higher than the fracture stresses. The specimens therefore fail by brittle fracture before the critical transformation stress is reached. However, in the case of the TZ-2Y composite, which also has similar levels of tensile residual stress (Figure 2.7b) but lower levels of stabilization, the critical transformation stress is reached before the onset of catastrophic fracture.

2.5. CONCLUSIONS

1. Almost linear X-ray and laser Raman spectroscopy calibration curves have been developed for the estimation of the volume fraction of monoclinic phase in $\text{MoSi}_2/\text{zirconia}$ mixtures. These calibration curves neglects the differences in the mass/laser absorption coefficients between the monoclinic and tetragonal zirconia phase. Nevertheless, estimates of phase content in powder mixtures with known compositions are consistent with predictions obtained from the calibration.
2. An analytical model has been developed for the estimation of residual mean stresses at the reinforcement/matrix interfaces in particulate-reinforced composite materials. The residual stress due to thermal expansion mismatch is predicted by the model to be sum of the self stresses of the individual particles and the contributions of surrounding particles to the residual mean stresses at the reinforcement/matrix interface of the individual particles. The model predicts that thermal mismatch residual stresses in the $\text{MoSi}_2/\text{zirconia}$ composites are tensile.
3. The overall residual stress in the composites that undergo phase transformations during processing can be estimated from the sum of the thermal mismatch residual stresses and the residual stress components induced as a result of the volume expansion (3-5%) that occurs as a result of the transformation from tetragonal to monoclinic phase during cooling from the processing temperature. The sign of the overall residual stress in the TZ-0Y composite is therefore compressive since a large compressive residual stress is induced as a result of the phase transformation that occurs in this material during cooling.
4. Transformation toughening occurs only in the TZ-2Y composite. The modest level of transformation toughening ($1.2 \text{ MPa}\sqrt{\text{m}}$) is predicted by existing theoretical mechanics models in which stress-induced transformations are assumed to occur only as a result of dilatational stresses. Toughening in the TZ-0Y composite occurs mainly as a result of the shielding effects of compressive residual stresses that are induced during processing, while toughening in the TZ-4Y and TZ-6Y composites is attributed to the shielding effects of observed microcrack distributions.

Chapter 3

Synergistic Toughening

3.1. Introduction

The synergistic toughening concept was first proposed by Amazigo and Budiansky [86]. In their original paper, they studied the combined toughening due to crack-bridging by ductile particles and transforming toughening by particles that undergo purely dilational stress-induced phase transformations in a brittle matrix. In their studies, they found that interactions between transformation toughening and crack bridging mechanisms may promote synergy in certain parametric ranges of constituents. Under such conditions, they predicted that the overall toughening is greater than the sum of the individual toughening components.

The objective of this section was to develop synergistically toughened MoSi_2 composites reinforced with transforming partially stabilized zirconia particles and bridging Nb reinforcements. Synergy was engineered by promoting interactions between crack bridging and transformation toughening. Since the results from the earlier studies showed that transformation toughening occurred only in the composite reinforced with TZ-2Y particles, i.e., 2 mole% yttria particles with an average particle size of $\sim 0.7 \mu\text{m}$ [49]. TZ-2Y particles were used as reinforcements in the synergistically toughened composites. Also, since the Nb laminates were also observed to have the higher fracture toughness levels ($\sim 18\text{-}20 \text{ MPa}\sqrt{\text{m}}$) than Nb fiber-reinforced ($9\text{-}15 \text{ MPa}\sqrt{\text{m}}$) and Nb particulate-reinforced ($\sim 5\text{-}6 \text{ MPa}\sqrt{\text{m}}$) composite containing 20 vol.% of Nb reinforcement, the Nb layer geometry was, therefore, selected for use in the hybrid/synergistically toughened composites that were examined in this phase of the program. Nb layers are shown to promote significant toughening via crack bridging and crack-tip blunting in the composites reinforced with 20 vol.% Nb layers and 20 vol.% TZ-2Y particles with an average sizes of $\sim 0.7 \mu\text{m}$. A limited amount of transformation toughening was also shown to occur, especially in the regions of high stress concentration near the interface between Nb and MoSi_2 .

3.2. Experimental

3.2.1 Material

In order to study the effects synergistic toughening, MoSi_2 composites reinforced with 20 vol.% of Nb layers and 20 vol.% zirconia particles stabilized with 2 mole% yttria (TZ-2Y) were fabricated. Nb foils ($200 \mu\text{m}$) were procured from G & S Titanium, Worcester, OH. The MoSi_2

powder, -325 mesh (approx. 44 μm average diameter), and TZ-2Y ($\sim 0.7 \mu\text{m}$) were purchased from Cerac, Milwaukee, WI. MoSi_2 and TZ-2Y are baked and ball milled for 48 hours. The Nb layers and MoSi_2 -TZ-2Y were manually deposited into Nb cans that were vacuum (10^{-4} Pa) sealed by electron beam welding prior to hot isostatic pressing (HIPing) at 1400°C under a pressure of 207 MPa. The microstructure of the resulting composite is shown in Figures 3.1a and 3.1b. These show the uniform distribution of TZ-2Y grains in MoSi_2 , and the structure of the Nb layers very clearly. A layered interfacial structure consisting of $(\text{Mo}, \text{Nb})_5\text{Si}_3$ and Nb_5Si_3 layers is also observed in the higher magnification photomicrograph shown in Figure 1b. Similar structures have been reported in the earlier studies on MoSi_2/Nb laminates. The morphology of the TZ-2Y particles is also comparable to that of the MoSi_2 composites reinforced only with 20 vol.% of TZ-2Y particles.

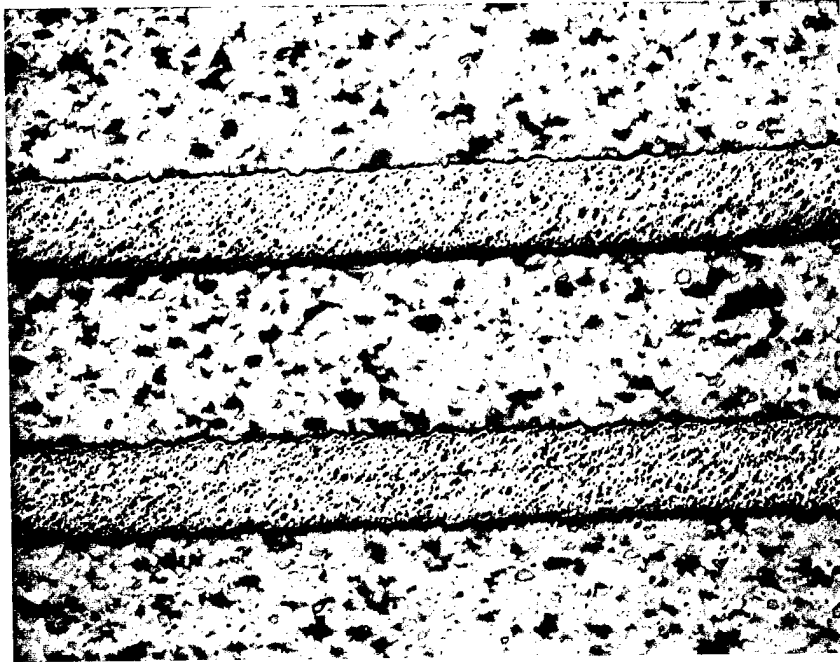
3.2.2 Fracture Toughness

Single Edge Notched (SEN) bend specimens with a square cross sections ($6.02 \times 6.02 \text{ mm}$) and a length of $\sim 38 \text{ mm}$ were fabricated by electro-discharge machining (EDM) techniques. The specimens had initial notch-length-to-width ratios of ~ 0.4 . The SEN specimens were deformed continuously to failure under monotonic loading at a ramp rate that corresponded to a stress intensity factor increase rate of $\sim 0.92 \text{ MPa}\sqrt{\text{m}}\cdot\text{s}^{-1}$. The fractured specimens were then examined under a scanning electron microscope to determine the failure modes in the composite.

The fracture toughness of the as-fabricated synergistically toughened composite ($\sim 21 \pm 1.0 \text{ MPa}\sqrt{\text{m}}$) is compared with previously reported data toughness data for MoSi_2 ($\sim 3.6 \text{ MPa}\sqrt{\text{m}}$) and MoSi_2 composites ($\sim 4\text{--}18 \text{ MPa}\sqrt{\text{m}}$) in Figure 3.2. Also included in Figure 3.2 is the range of fracture toughness data that is typically obtained from structural aluminum alloy [4] which have typical toughness values between 20 and 25 $\text{MPa}\sqrt{\text{m}}$ [26]. The synergistically toughened composites therefore have fracture toughness levels that are comparable to those of structural aluminum alloys.

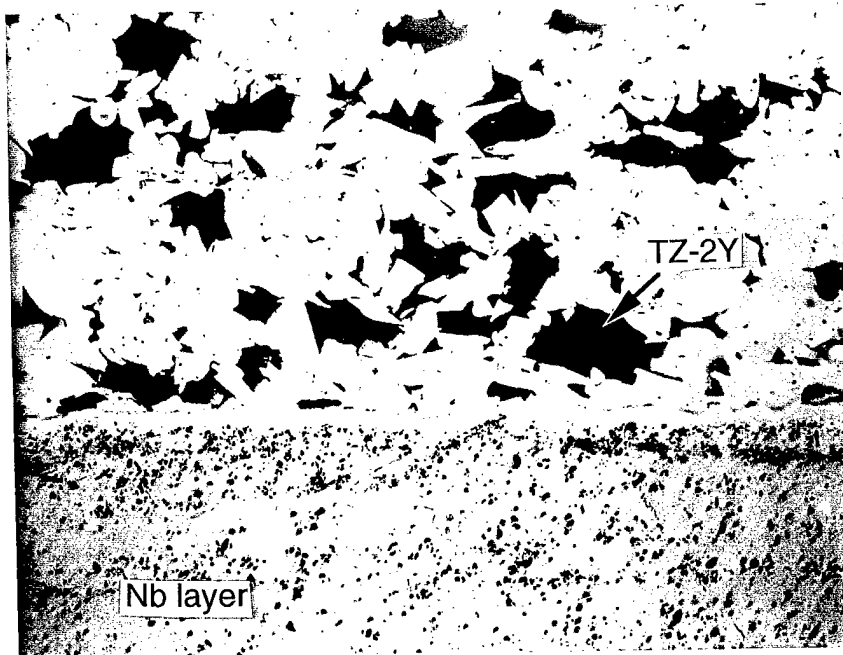
However, it is important to note that the measured fracture toughness values correspond to an instability point along a rising resistance curve. The initiation toughness values of the synergistically toughened are thus likely to correspond to the toughness levels of $\sim 5 \text{ MPa}\sqrt{\text{m}}$ obtained from previous studies of TZ-2Y reinforced MoSi_2 [49]. The synergistically toughness may, therefore, have relatively low initiation fracture toughnesses compared to existing structural aluminum alloys [26]. Nevertheless, the measured fracture toughness of $21 \pm 1.0 \text{ MPa}\sqrt{\text{m}}$ is clearly remarkable. It is clearly the highest fracture toughness that has been reported for any MoSi_2 composite. It is also encouraging to note that further improvements in fracture toughness may be achieved via optimization of the structure of the synergistically toughened composite.

(a)



200μm

(b)



200μm

Figure 3.1 Microstructure of Synergistically Toughened Composite $\text{MoSi}_2 + 20 \text{ Vol. \% Nb}_1 + 20 \text{ Vol. \% TZ-2Y}_p$:

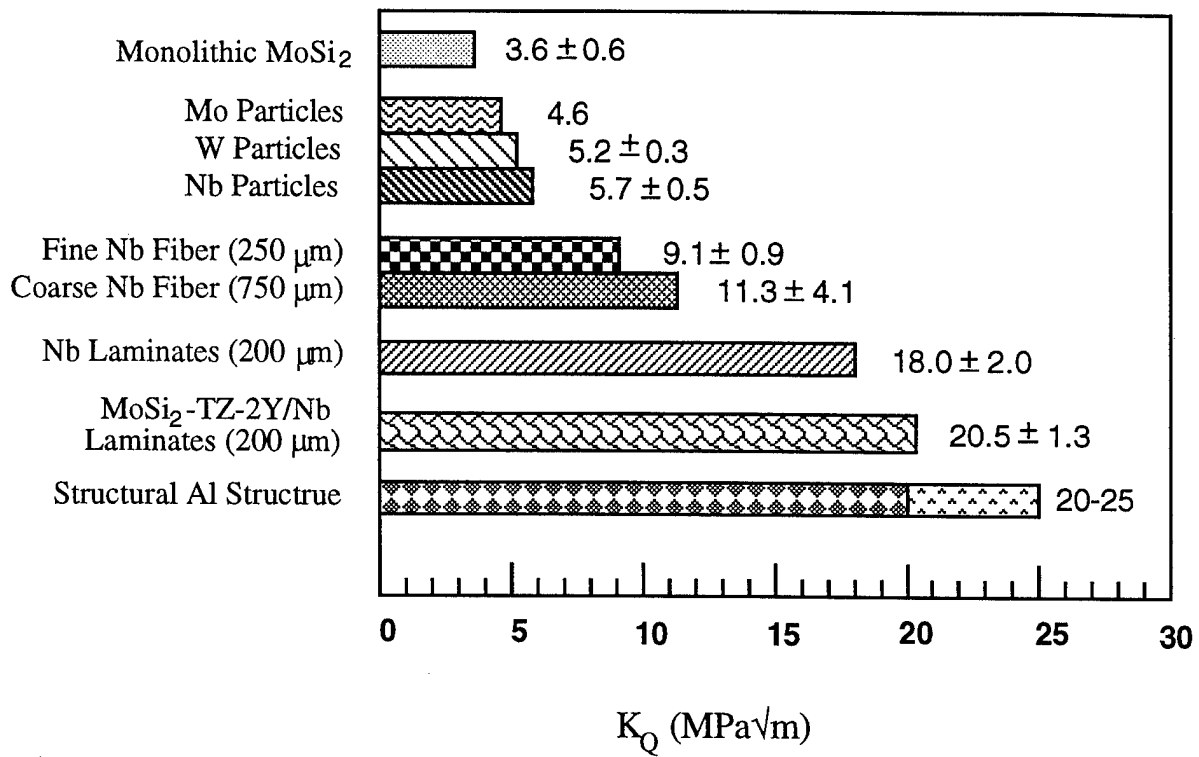


Figure 3.2 Fracture Toughness Data

Fracture of the MoSi₂ occurred a combination of intergranular and cleavage fracture (Figure 3.3). A flat featureless fracture surface was also observed in the zirconia grains, while the Nb layers failed by a combination of cleavage and ductile dimpled fracture modes. A limited amount of debonding was also observed to occur between the Nb layers and the MoSi₂/TZ-2Y layers. Such debonding may be associated with crack-tip blunting mechanisms observed in earlier studies on layered MoSi₂/Nb composites.

After fracture testing, laser Raman spectroscopy analysis was performed on the sides of the fractured specimens to determine the volume fraction of monoclinic/tetragonal phase as a function of distance from the crack faces and distance from the Nb layer. The results are illustrated in Figure 3.5. Note that a typical Raman spectrum of deformed and undeformed materials is also shown in Figure 3.4. Higher levels of transformation from tetragonal to monoclinic phase were observed in the regions close to crack and the Nb laminate. The latter are attributed to the higher interfacial strains/stresses in the regions close to the Nb layer. By careful analysis of Raman data, the transformation zone size was estimated to be 150 μm . Also the Raman analysis revealed that approx. 4.5% of the TZ-2Y particles transformed. The toughening due to transformation in this composite was thus estimated to be about 0.4 $\text{MPa}\sqrt{\text{m}}$ (using Equation 2.3).

For comparison, toughening due to crack bridging and crack-tip blunting can be estimated from Equations 1.5 and 1.6, respectively. The toughening due to crack bridging was thus estimated to be $\sim 7.8 \text{ MPa}\sqrt{\text{m}}$. The toughening due to crack-tip blunting was thus estimated to be $\sim 4.5 \text{ MPa}\sqrt{\text{m}}$. Hence, by applying the principle of linear superposition, the toughness of MoSi₂/Nb-TZ-2Y composite was estimated to be about 16.3 $\text{MPa}\sqrt{\text{m}}$. This is lower than the experimental value of $\sim 21 \text{ MPa}\sqrt{\text{m}}$.

3.2.3 Fatigue Crack Growth

The fatigue crack growth rates in the Nb fiber-reinforced composites are compared with corresponding fatigue crack growth rate data obtained from pure monolithic Nb in Figure 3.5. Note that the monolithic Nb was processed under the same conditions as the composites. Fatigue crack growth rate data reported for monolithic MoSi₂ [23] is also included in Figure 3.5 for comparison. Such data is very difficult to obtain at room-temperature due to the very brittle nature of monolithic MoSi₂. In any case, the slopes of the da/dN versus ΔK plots obtained for monolithic MoSi₂ in the Paris regime are very high. However, the fatigue crack growth rates in monolithic MoSi₂ are slower or comparable to those in the composites in the low ΔK regime.

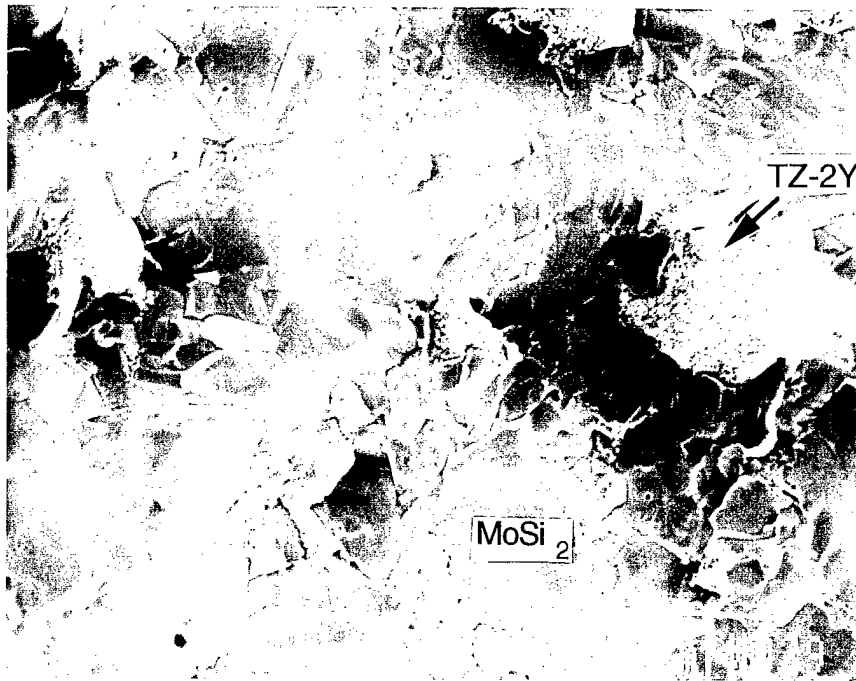
Unlike monolithic MoSi₂, in which stable fatigue crack growth was difficult to obtain at stress intensity factor levels below the fracture toughness [5,6,10,23], stable fatigue crack growth occurred readily in the MoSi₂/Nb composites that were examined in this study. However, the

initial crack growth rates were high in all the composites. Stable crack growth in the MoSi₂/Nb composites was intermittent due to the interactions of the fatigue cracks with the Nb layers. Furthermore, stable fatigue crack growth in the MoSi₂ matrix occurred predominantly by transgranular cleavage. Similar to the MoSi₂ composite reinforced with Nb layers, the Nb layer did not fail by ductile dimpled fracture. Instead, fracture of the Nb layer occurred by cleavage fracture modes (Figures 3.6), presumably as a result of the high strain rates associated with reversed plasticity under cyclic loading [17].

3.3 Conclusions

1. Higher fracture toughness levels were observed in the MoSi₂ composite reinforced with 20 vol. Nb and 20 vol. TZ-2Y. The improved toughness is attributed to the combined effects of shielding due to crack-tip blunting, bridging and transformation toughening.
2. Higher levels of transformation in the regions close to the Nb layers are attributed to the effects of higher interfacial stresses. However, the overall contribution from transformation toughening is less significant than the contributions from crack-tip blunting and crack bridging.
3. Stable fatigue crack growth was observed in the synergistically toughened composite. However, fatigue crack growth was intermittent due to crack interactions with the Nb layer.
4. Fracture of the Nb layer occurs by a mixture of cleavage and ductile fracture under monotonic loading. However, failure of the Nb layer occurred solely by cleavage. The higher incidence of cleavage, observed under cyclic loading, is attributed to the higher strain rates that occur under cyclic loading.

(a)



(b)

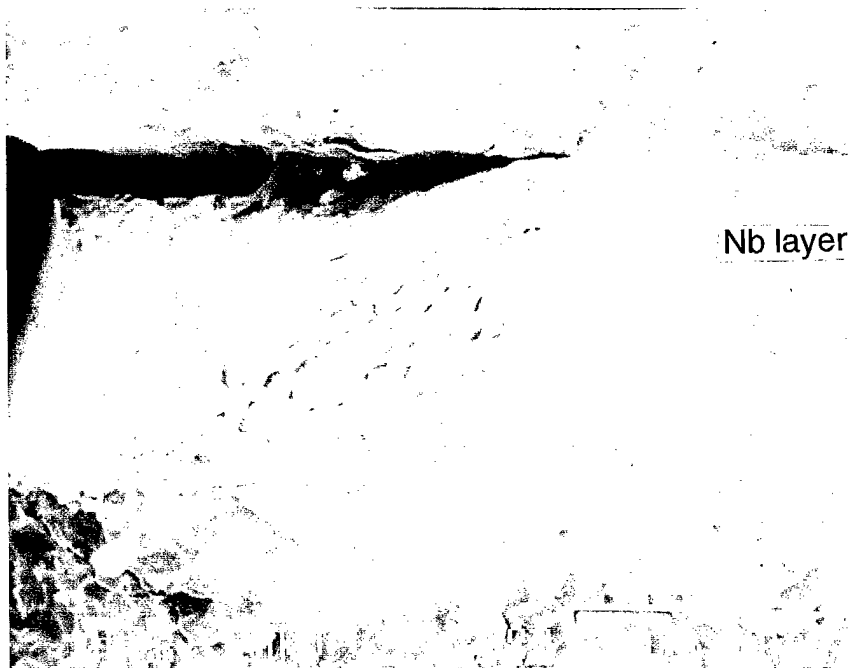
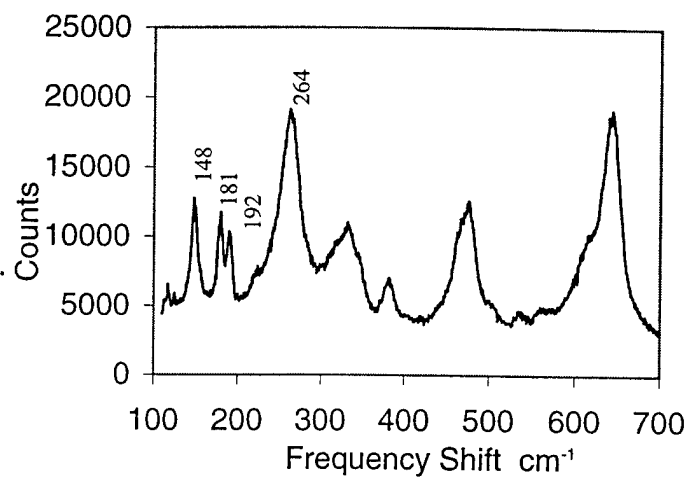


Figure 3.3 Typical Fracture Mode of Fracture Toughness Specimens
(a) Matrix and (b) Nb Layer.

(a)



(b)

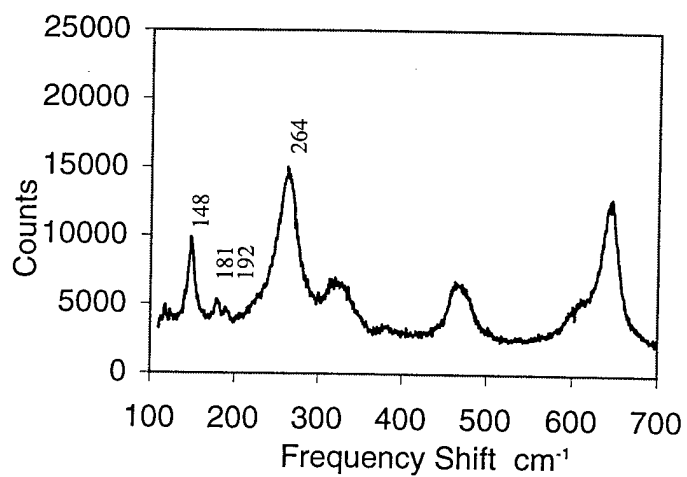


Figure 3.4 Typical Raman Spectrum Observed
(a) Transformed (b) Untransformed (As-Received)

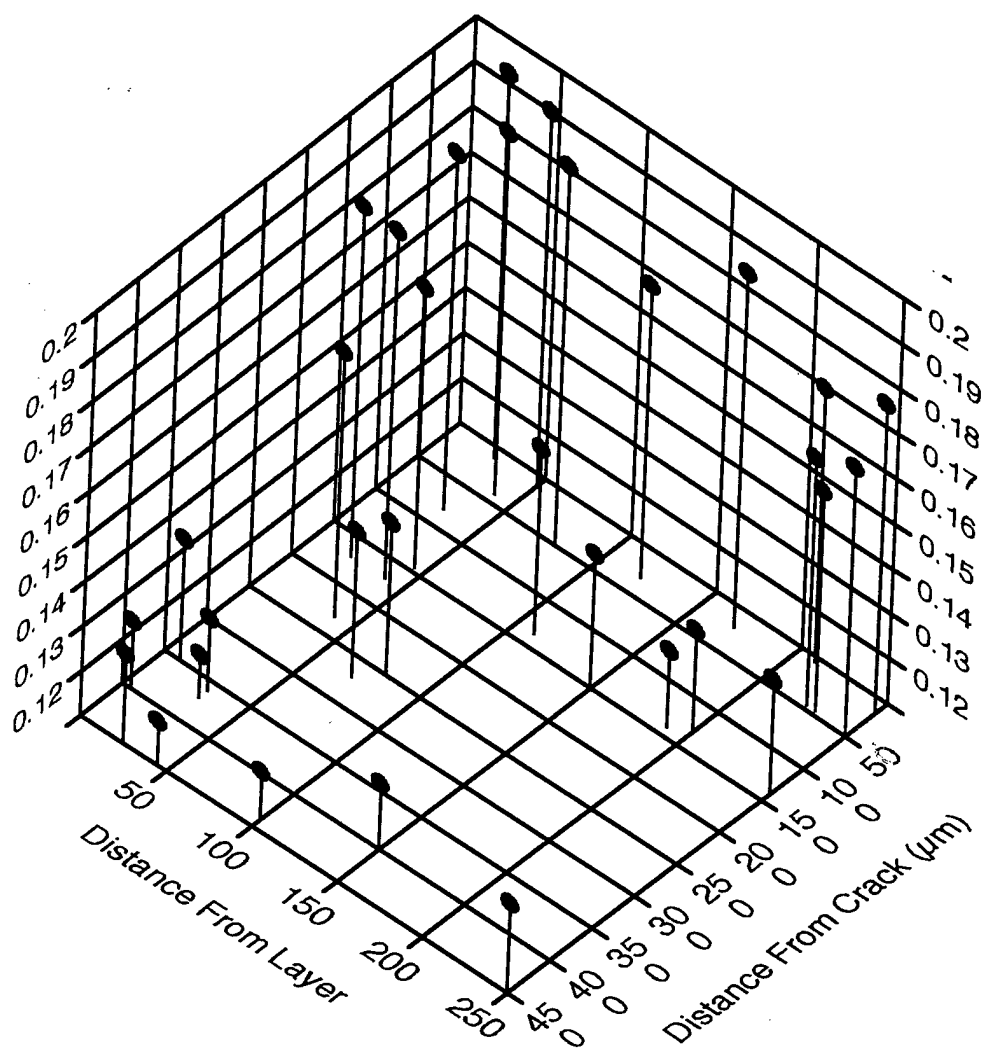


Figure 3.5 Volume Percentage of Monoclinic Phase

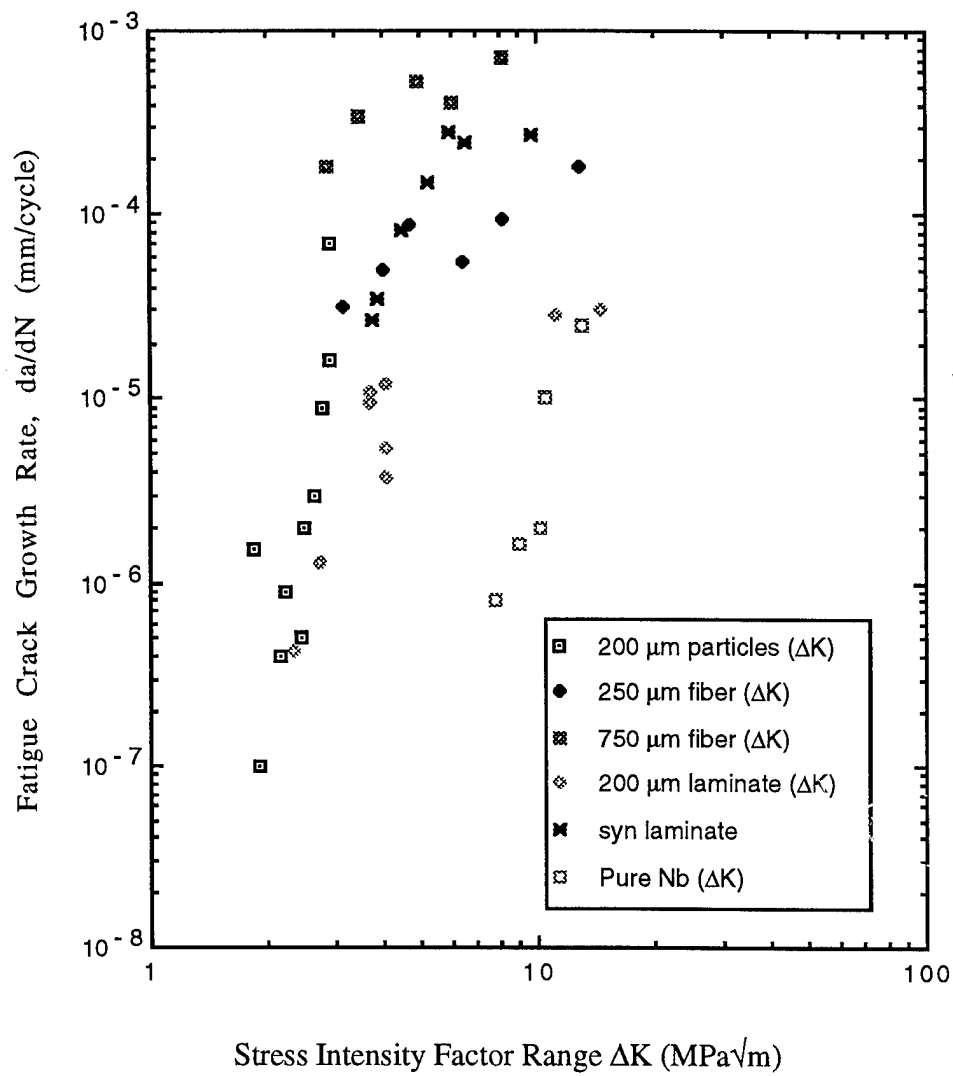


Figure 3.6 Summary of Fatigue Crack Growth Rate Data

(a)



(b)

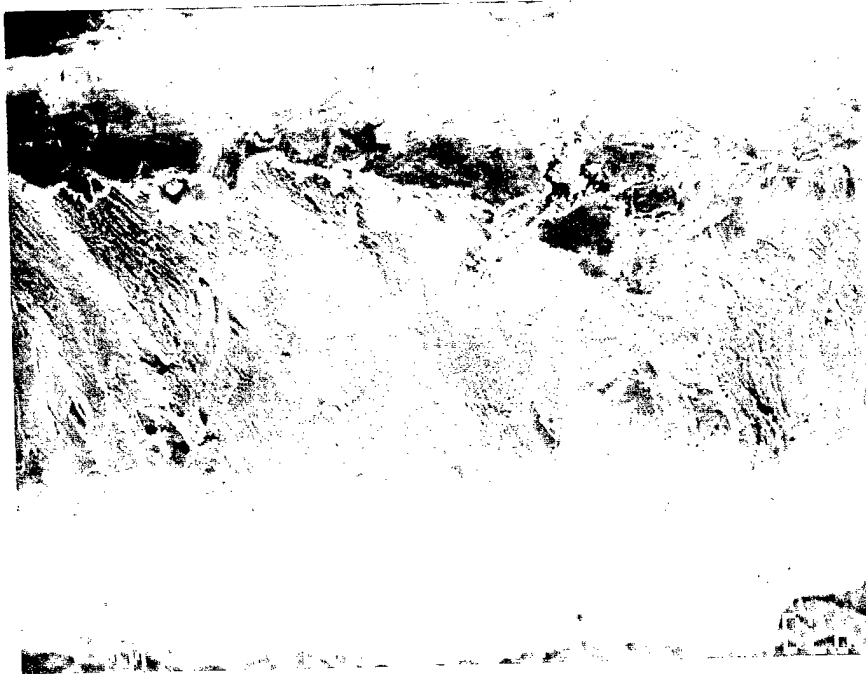


Figure 3.7 Typical Fatigue Fracture Mode
(a) Matrix and (b) Nb Layer

Chapter 4

Fatigue and Fracture of Brittle-Reinforced Molybdenum Disilicide Composites at Elevated Temperature

4.1. Introduction

Mixed results have been obtained from the efforts designed to improve the damage tolerance of MoSi_2 . Although significant improvements (from $4 \text{ MPa}\sqrt{\text{m}}$ in MoSi_2 to $\sim 18\text{-}24 \text{ MPa}\sqrt{\text{m}}$ in MoSi_2/Nb laminates) have been achieved by reinforcement with thermodynamically compatible W, Mo and Nb ductile phase reinforcements [12-16], there are great concerns about the concomitant effects of ductile phases on the elevated-temperature oxidation resistance of MoSi_2 . There have also been significant efforts to toughen MoSi_2 by the incorporation of more oxidation resistant brittle phases such as SiC whiskers and ZrO_2 particles [44-49]. Unfortunately, however, these efforts have resulted only in limited improvements in the room-temperature toughness of MoSi_2 (approx. $\sim 4 \text{ MPa}\sqrt{\text{m}}$). Efforts to toughen MoSi_2 by solid solution alloying with WSi_2 have also been largely unsuccessful [47]. There is, therefore, a need for further efforts to engineer improved damage tolerance in MoSi_2 -based systems. There is also a need for careful studies of the elevated-temperature damage tolerance of MoSi_2 in the potential service temperature regime ($1200\text{-}1300^\circ\text{C}$).

Elevated-temperature (1200°C) fatigue and fracture mechanisms in MoSi_2 and two brittle-reinforced MoSi_2 composites ($\text{MoSi}_2 + 20 \text{ vol.}\% \text{ SiC}_w$ and $\text{MoSi}_2 + 20 \text{ vol.}\% \text{ ZrO}_2$ stabilized with 2 mole % Y_2O_3) are elucidated in this chapter. Elevated temperature fracture toughness levels in MoSi_2 and the two composites are shown to be lower than those in the corresponding materials tested at room-temperature. The lower elevated-temperature fracture toughness levels are attributed to the embrittling effects of amorphous glass phases that are produced at the grain boundaries of the MoSi_2 grains during elevated-temperature exposure at 1200°C . As in previous work [33,85,86], creep-fatigue crack growth mechanisms are postulated for MoSi_2 and the MoSi_2 composites. Creep-fatigue components of crack growth are shown to involve microvoid formation via the viscous flow of amorphous glass phases and possible glass phase pull-out mechanisms. Mechanical fatigue crack growth components are attributed to kinematic irreversibility due to partially irreversible slip mechanisms (dislocation-induced plasticity) and crack-tip chemical reactions. The crack growth rates are compared with previously reported data obtained from MoSi_2 -based materials [22].

4.2. Experimental Procedure

4.2.1 Material Processing and Microstructures

Fatigue crack growth and fracture toughness tests were conducted on monolithic MoSi_2 , SiC whisker-reinforced and ZrO_2 particle-reinforced MoSi_2 composites. The tests were conducted in laboratory air at 1200°C . The monolithic and composite materials were produced from constituents that were procured from various suppliers. MoSi_2 powder (-325 mesh /44 μm average particle diameter) with 99.5% purity was procured from Cerac, Milwaukee, WI. Silicon carbide whiskers (1- μm in diameter with an average aspect ratio of ~ 10) were obtained from Advanced Refractory Technologies, Inc., Buffalo, NY. Zirconia powder (0.7 μm average particle diameter) stabilized with 2 mole % of yttria (99% purity) was supplied by The Tosoh Corporation, Bound Brook, NY. Mixtures consisting of 80 vol. % MoSi_2 and 20 vol. % zirconia particles or 80 vol. % MoSi_2 and 20 vol. % SiC whisker were then produced by dry phase blending/ball milling for 24 hours. The dry phase blended powders were then poured into Nb cans, vacuum sealed by electron beam welding and hot isostatically pressing (HIPing) at 1400°C (207 MPa pressure for 4 hours). Monolithic MoSi_2 was also fabricated by HIPing of MoSi_2 powders under the same processing conditions that were used for the processing of the MoSi_2 composites.

Microstructures of the MoSi_2 and MoSi_2 composites (SiC_w and TZ-2Y) were examined after annealing at 1200°C for 30 minutes to simulate the possible microstructural changes that can occur during elevated-temperature mechanical testing. The microstructures of the as-received and heat treated materials were studied using TEM and SEM techniques. Foils for TEM examination were prepared from circular discs of heat treated materials that were 3 mm in diameter. The slices, which were 150 μm thick, were produced by electro-discharge machining (EDM), prior to the grinding of both sides to a thickness of about 80 μm . The ground specimens were then dimpled to a final thickness of about 30 μm . Finally, the foils were ion milled to produce thinned regions for TEM examination. The TEM examination was conducted to identify the dislocation substructures, the microcrack distributions, and the possible formation of amorphous glass phases in the annealed materials. SEM was also used to study the microstructural features in the as-received and annealed materials.

4.2.2 Cyclic Fatigue Crack Growth at 1200°C

Fatigue crack growth tests were conducted on the MoSi_2 , SiC whisker-reinforced and ZrO_2 particle-reinforced MoSi_2 composites. The composites were reinforced with 20 vol.% of SiC or ZrO_2 particles. The tests were conducted in laboratory air at 1200°C . Fatigue testing was conducted under four-point bend loading (with an inner span of 8 mm and an outer span of 16

mm) using single edge notched (SEN) bend bars with rectangular ($6\text{ mm} \times 3\text{ mm}$) cross sections. Notches that were 1.5 mm in depth were introduced by electro-discharge machining. Fatigue crack growth testing was conducted on as-received materials that were polished to a mirror surface finish prior to fatigue testing. Both sides of the SEN specimens were ground with emery paper and diamond polished to a surface of $1\mu\text{m}$ prior to testing. This was done to facilitate crack length measurement and microstructural observation during fatigue crack growth testing.

The SEN specimens were pre-cracked in air under uniaxial compression-compression loads at 1200°C . Pre-cracking was conducted in a servohydraulic testing machine with a mounted electric resistance furnace. The cyclic compression pre-cracking frequency was 10 Hz and the pre-cracking wave form was sinusoidal. During each compression pre-cracking stage, if no pre-crack was observed, the loads were increased in incremental stages of 10% until a pre-crack was obtained. The polished sides of the SEN specimens were checked under an optical microscope in between each incremental loading stage.

The pre-cracked SEN specimens were “soaked” in laboratory air at 1200°C for 30 minutes prior to fatigue testing at elevated temperature. The pre-cracked SEN specimens were then loaded under four-point bending using SiC rams and SiC rollers that were 3 mm in diameter. A load ratio (minimum load to maximum load) of 0.2 was employed in the fatigue tests which were conducted at a cyclic frequency of 10 Hz. The fatigue crack growth rate tests were conducted at 1200°C in air using an Instron servohydraulic testing machine. Fatigue crack growth was monitored and measured with an optical microscope. If no crack growth rate was detected after 10^4 cycles, the load range was increased by 10% until the crack growth was detected. It is important to note that the SEN specimens were not loaded during the thermal excursions associated with heating up to the test temperature and cooling down to the room temperature.

4.2.3 Fracture Toughness at 1200°C

Fracture toughness data were also obtained by testing SEN specimen at 1200°C in air. The tests were performed under three point bending using an Instron servohydraulic testing machine. The three point bend specimens were fabricated using an electro-discharge machine with $100\mu\text{m}$ thick diameter wire. Specimens with rectangular cross-sections ($6\text{ mm} \times 6\text{ mm}$) and length of 32 mm were produced via EDM. The initial ratio of crack length to specimen width was ~ 0.42 . The specimens were loaded monotonically to failure at a loading rate that corresponded to a stress intensity factor increase rate of $0.92\text{ MPa}\sqrt{\text{m}}\cdot\text{s}^{-1}$. The fracture surfaces of the failed specimens were then examined under a scanning electron microscope.

4.3. Results And Discussion

4.3.1 Microstructures and Substructure

Scanning electron photomicrographs of the HIPing material are presented in Figures 4.1a-3.1c. These show clearly that ZrO_2 grains and SiC whiskers were present mainly at the grain boundaries of the MoSi_2 grains. The presence of both the ZrO_2 particles (0.7 μm diameter) and the SiC whiskers (1 μm diameter with an aspect ratio of up to 10) at the MoSi_2 grains boundaries is attributed to the relatively small size of the reinforcements which were much smaller than the MoSi_2 (44 μm average diameter) particles that were employed in this study. The ZrO_2 particles and SiC whiskers were thus distributed within the interstices of the MoSi_2 powders after dry phase blending. Hence, the reinforcement phases were distributed predominantly along the MoSi_2 grain boundaries after subsequent HIPing (Figures 4.1a-4.1c).

TEM examination of the HIPed MoSi_2 and MoSi_2 composites was conducted on material annealed at 1200°C for ~ 30 minutes. The material was annealed to simulate the effects of potential thermal exposures during mechanical testing. The TEM analysis revealed clear evidence of the presence of intergranular amorphous glass phases and dislocation networks in the MoSi_2 matrix (Figures 4.2a-4.2f). The amorphous glass phases were observed at the grain boundaries of the MoSi_2 and TZ-2Y composite after annealing of 1200°C for ~ 30 minutes (Figures 4.2a and Figure 4.2e). Extensive networks of dislocations were also observed during the TEM analysis of MoSi_2 and the TZ-2Y composite. Typical dislocation configurations are presented in Figure 4.2b (MoSi_2) and Figure 4.2f (TZ-2Y). Dislocation networks were also found in the SiC_w composite, as shown in Figures 4.2c and 4.2d. However, the dislocation densities in the SiC_w composite were not as high as those in the other materials. Also, no obvious amorphous glass phase was detected in the SiC_w composite.

4.3.2 Fracture Toughness

Fracture toughness data obtained from three-point bending tests conducted at 1200°C in air are compared with room-temperature toughness data in Table 4.1. The fracture toughness values are approximately 40~70% lower than those at room temperature. The degradation in fracture toughness is attributed to the effects of the amorphous glass phases that were formed during elevated-temperature thermal exposure. However, it is important to note here that the fracture toughness of the SiC_w composite was less degraded at elevated-temperature, presumably as a result of the absence of amorphous glass phase in this material. Nevertheless, the elevated-temperature fracture toughness levels were lower than the room-temperature fracture toughness values in all the materials that were examined in this study. This is contrary to the limited results

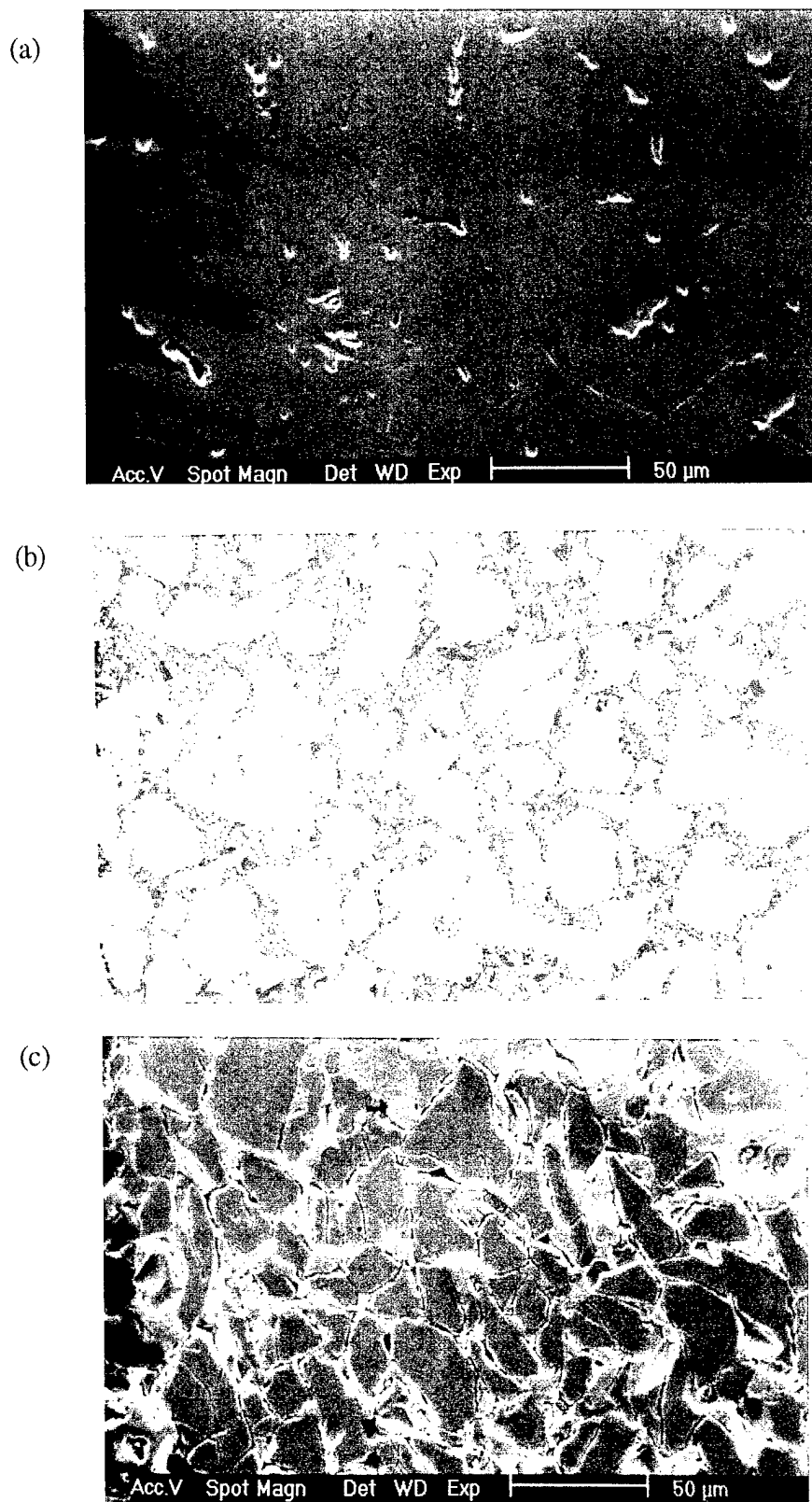


Figure 4.1 SEM Photomicrographs Showing Microstructural Features of MoSi_2 and Brittle Reinforced MoSi_2 Composites: (a) MoSi_2 ; (b) $\text{MoSi}_2 + 20 \text{ vol.}\% \text{ SiC}_w$, and (c) $\text{MoSi}_2 + 20 \text{ vol.}\% \text{ TZ-2Y}$

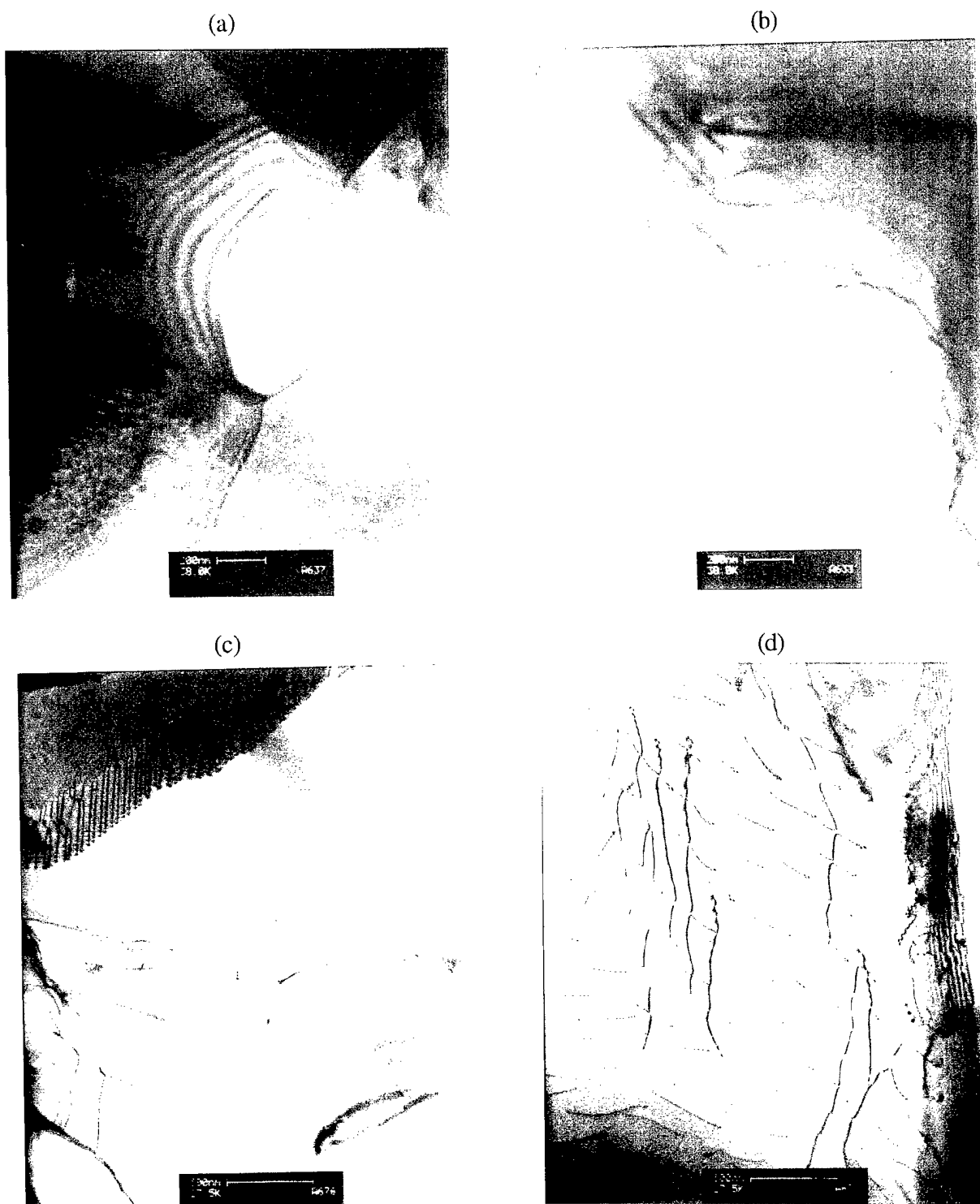


Figure 4.2 TEM Photomicrographes of MoSi₂ and Brittle Reinforced MoSi₂ Composites
 (a) MoSi₂ (1200 °C/0.5h/AC); (b) MoSi₂ (1200 °C/0.5h/AC); (c) MoSi₂ + 20
 vol.% SiC_w (1200 °C/0.5h/AC); (d) MoSi₂ + 20 vol.% SiC_w (1200 °C/0.5h/AC);

(a)

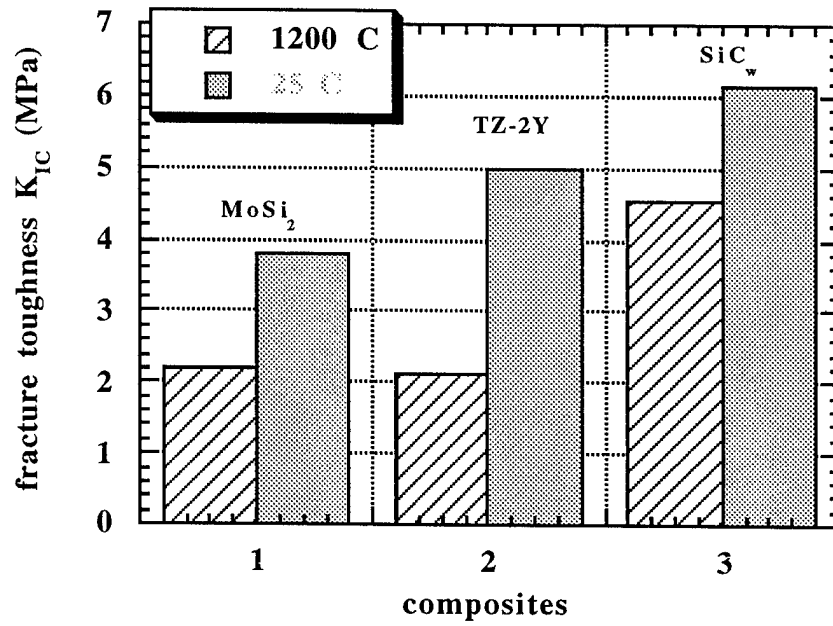


(b)



Figure 4.2 TEM Photomicrographes of MoSi_2 and Brittle Reinforced MoSi_2 Composites
(e) $\text{MoSi}_2 + 20 \text{ vol. \% TZ-2Y}$ ($1200^\circ\text{C}/0.5\text{h}/\text{AC}$);
(f) $\text{MoSi}_2 + 20 \text{ vol. \% TZ-2Y}$ ($1200^\circ\text{C}/0.5\text{h}/\text{AC}$)

Table 3.1 Summary of Fracture Toughness Data



presented for MoSi₂-based systems in the literature [33,85,86]. However, reasons for the observed trends in the fracture toughness data are not well understood at present.

4.3.3 Fatigue Crack Growth Mechanism

Subcritical fatigue crack growth was observed in the MoSi₂ and MoSi₂ composites at 1200°C. However, stable subcritical crack growth was only observed within a narrow stress intensity factor range. Stable fatigue crack growth was not observed in monolithic MoSi₂ at room-temperature under tensile/bending loading. However, under well-controlled compression pre-cracking conditions, it was possible to obtain stable fatigue crack growth data from the MoSi₂-based systems examined in this study. The elevated-temperature fatigue crack growth rate data obtained for monolithic MoSi₂ and the TZ-2Y and SiC_w composites are summarized in Figure 4.3a. The fatigue thresholds obtained for the three different materials were approx. 1 MPa√m at 1200°C. These are comparable to fatigue thresholds obtained from previous studies [17,22,43] on ductile Nb particulate-reinforced MoSi₂ (Figure 4.3b). However, the fatigue thresholds are lower than those reported by Ramamurthy et al. [33] for MoSi₂-based systems alloyed with small amounts of carbon that are known to improve the deformation and fracture behavior of MoSi₂ (Table 4.2). It is also of interest to note that the fatigue crack growth rates obtained from this study were considerably faster than those reported previously in creep-fatigue studies by Ramamurthy et al.[33].

Typical Paris constants m (According Paris's law, crack growth rate $da/dN=C(\Delta K)^m$, where ΔK is the stress intensity and C and m are known as Paris constants) from both studies are summarized in Table 4.2. The differences between the fatigue crack growth rates are attributed to differences in composition (the effects of carbon addition discussed earlier) and different processing methods (dry phase blending in this study versus slurry-based mixing with sintering aids [33]) that were used in the different studies. Therefore, as discussed, the addition of C and sintering aids, and the use of slurry-based processing methods in the previous studies [33,84,85] appears to result in MoSi₂-based materials with improved fatigue and fracture behavior. However, further analysis is needed to explain the crack-tip deformation mechanisms and fracture modes that are associated with the observed differences.

4.3.4 Fracture Modes

Typical fracture modes observed under monotonic and cyclic loading are presented in Figures 4.4-4.6 for the three materials that were examined in this study. Brittle fracture modes were observed in all the materials that were tested under monotonic loading at room-temperature (Figure 4.4). Fracture of MoSi₂ occurred predominantly via transgranular cleavage mechanisms.

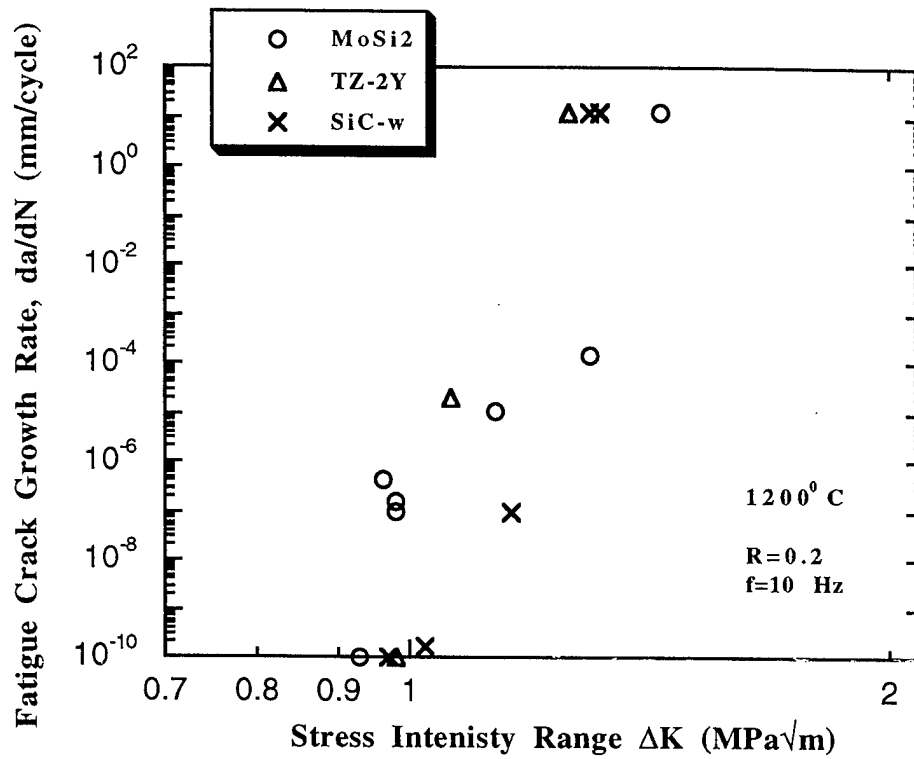


Figure 4.3 Plot of Fatigue Crack Growth Rate vs Stress Intensity Factor Range
(a) Comparison of MoSi₂ and SiCw/TZ-2Y Composites Data.

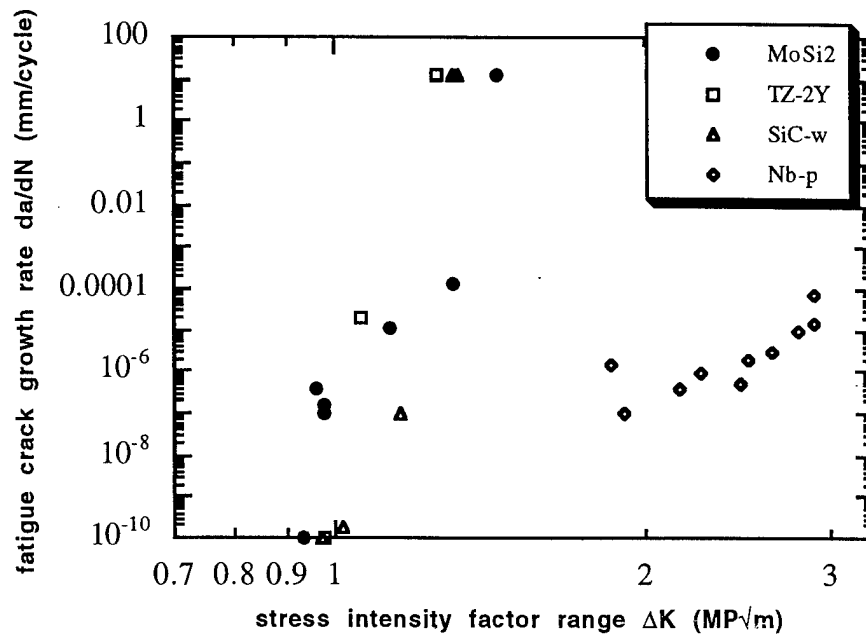


Figure 4.3 Plot of Fatigue Crack Growth Rate vs Stress Intensity Factor Range
(b) Comparison of MoSi₂ and Fatigue Crack Growth Data from Ref.[22].

Table 3.2 Fatigue Crack Growth Parameters at 1200 °C (n=10 Hz, R=0.2)

| Materials | C (mm/cycle)· (MPa√m) ^{-m} | m | ΔK Range (MPa√m) | Temperature °C | Reference |
|---|---|-------|-----------------------------|-------------------|-----------------|
| monolithic MoSi ₂ | 9.1×10 ⁻⁸ | 32.1 | 0.9 -1.4 | 1200 | present work |
| MoSi ₂ +20 vol.%SiC _w | 2.3×10 ⁻⁹ | 155.6 | 0.98 -1.3 | 1200 | present work |
| MoSi ₂ +20 vol.%TZ-2Y | 1.8×10 ⁻¹⁰ | 40.8 | 1.0 -1.3 | 1200 | present work |
| MoSi ₂ +20 vol.% SiC _p | 3.3×10 ⁻⁹ | 3.9 | 4.1-8.0 | 1200 | [26] |
| MoSi ₂ +20 vol.% SiC _p | 2.3×10 ⁻⁷ | 6.0 | 2.1-4.7 | 1300 | [26] |
| MoSi ₂ + 20 vol.% SiC _p +2 wt.% C | 1.8×10 ⁻⁸ | 3.8 | 4.6 -7.0 | 1300 | [28] |

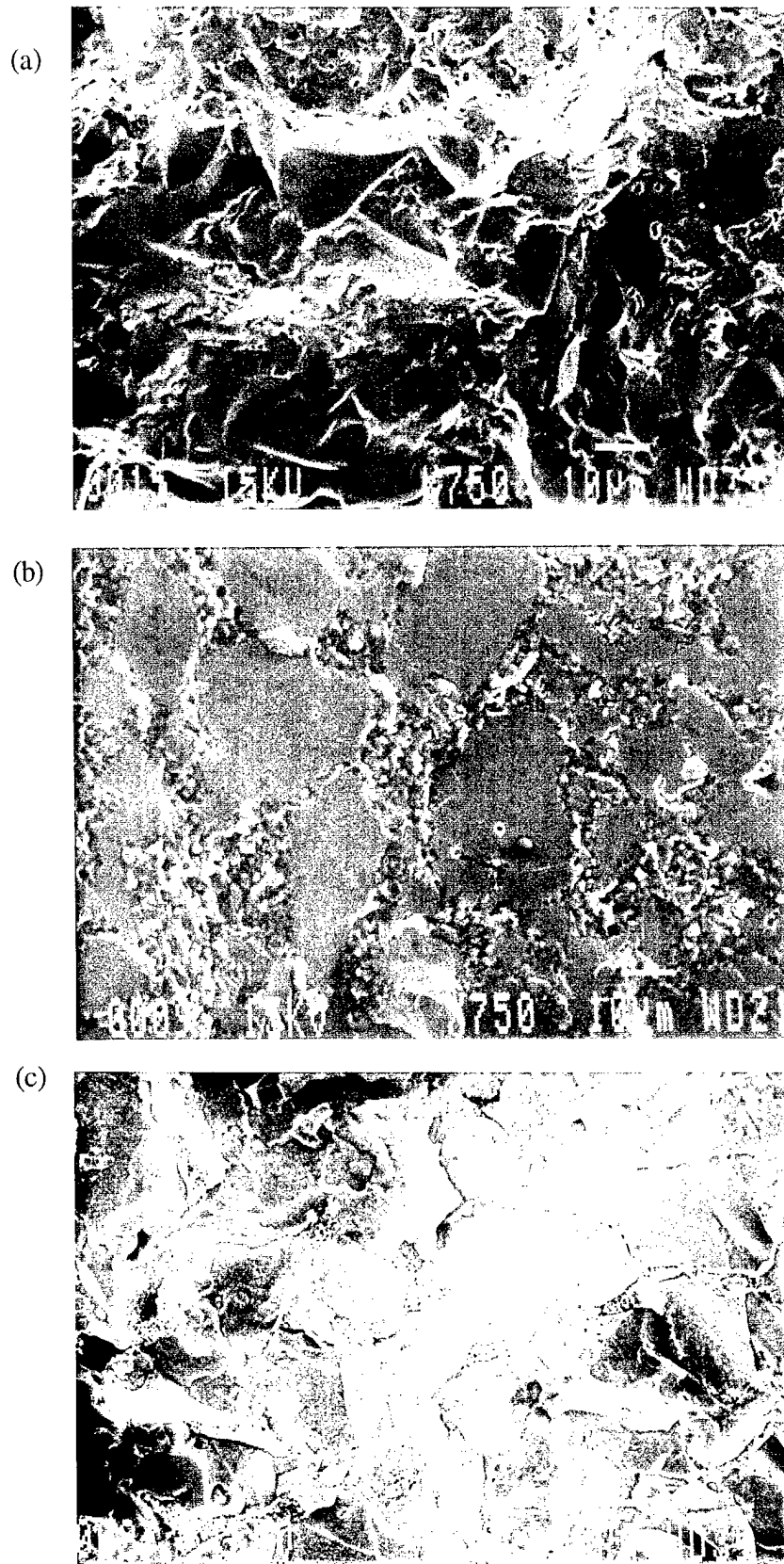


Figure 4.4 Typical Fracture Surface Morphologies of MoSi_2 and Brittle Reinforced MoSi_2 Composites at Room Temperature

(a) MoSi_2 ; (b) $\text{MoSi}_2 + 20 \text{ vol.}\% \text{ SiC}_w$, and (c) $\text{MoSi}_2 + 20 \text{ vol.}\% \text{ TZ-2Y}$

This is consistent with characteristic “clam-shell” markings and “river lines” that are associated typically with this mode of failure. However, some incidence of intergranular fracture was also observed on the fracture surfaces of SEN fracture toughness specimens. Indirect evidence of crack deflection was also observed on the fracture surfaces of the composites which were generally rougher than the fracture surfaces of monolithic MoSi_2 after fracture toughness testing at room-temperature (Figures 4.4a-4.4c).

The fracture modes observed in MoSi_2 and MoSi_2 composites at 1200°C were similar to those observed in the same materials at room-temperature (Figures 4.5a-4.5c). However, there was some evidence of enhanced intergranular porosity within the reinforcement phases that were distributed primarily along the MoSi_2 grain boundaries of the TZ-2Y composite (Figure 4.5c). A much lower incidence of intergranular porosity was also observed in the SiC_w composite specimen which retained a higher fracture toughness level of $4.5 \text{ MPa}\sqrt{\text{m}}$ at elevated-temperature (Table 4.1). The enhanced porosity levels in the TZ-2Y composite are attributed mainly to the fracture susceptibility of the amorphous glass phase that is formed during elevated-temperature exposure at 1200°C (Figures 4.2c).

Stronger evidence of crack-tip environmental interactions is apparent on the fracture surfaces of the elevated-temperature fatigue crack growth specimens. The fracture surfaces of these specimens were highly oxidized, presumably as a result of crack-tip chemical reactions that occur during fatigue crack growth testing in laboratory air at 1200°C (Figures 4.6a-4.6c). Clear evidence of transgranular and intergranular cavitation was also observed on the fracture surface of the monolithic MoSi_2 fatigue specimen. The microvoids may be associated with viscous flow process and other time dependent creep-fatigue phenomena that have been suggested in previous studies by Ramamurthy et al.[33,84,85]

The fatigue fracture modes of MoSi_2 composites are shown in Figure 4.6b and 4.6c. Matrix (MoSi_2) failure occurred via flat transgranular cleavage fracture modes and there was very little evidence of transgranular porosity. However, extensive intergranular porosity was observed at the boundaries of the MoSi_2 grains (Figure 4.6c). The amount of porosity is much higher than they should have with 98-99% density. They may due to viscous flow of the amorphous glass phases formed as a result of the reaction of silicon (within MoSi_2) with oxygen at elevated temperature. The predominance of intergranular porosity suggests that Si diffuses to grain boundaries prior to oxidation reactions that lead to the formation of amorphous silica (SiO_2). The amorphous silica may also contain other elements due to the interdiffusion of other elements that are present in the MoSi_2 and composite constituent phases. The differences in the observed intergranular porosity modes are, therefore, attributed to the different grain boundary diffusion couples that are induced in the MoSi_2 -based systems examined in this study.

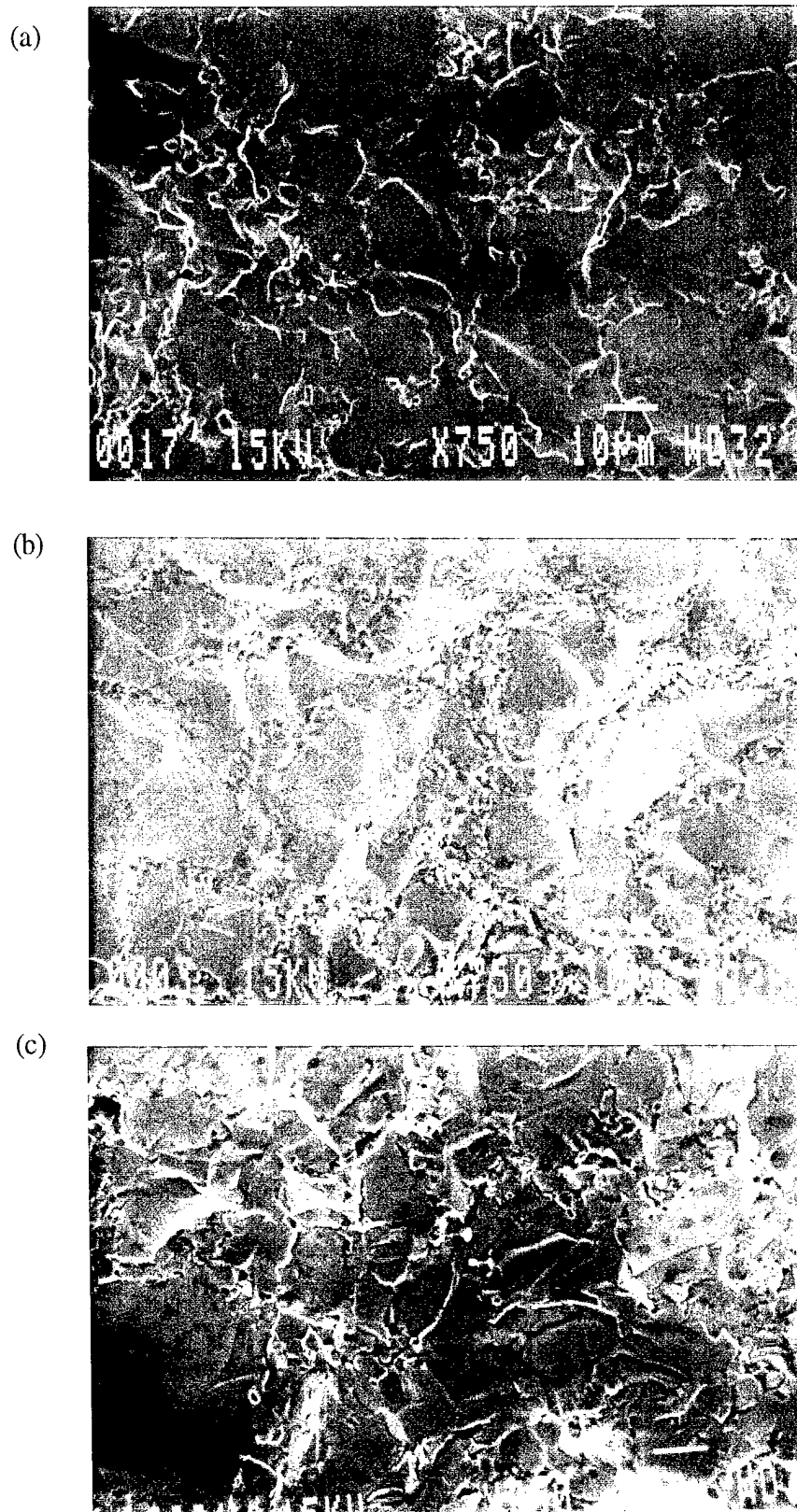


Figure 4.5 Typical Fracture Surface Morphologies of MoSi_2 and Brittle Reinforced MoSi_2 Composites at 1200°C

(a) MoSi_2 ; (b) $\text{MoSi}_2 + 20 \text{ vol.}\% \text{ SiC}_w$, and (c) $\text{MoSi}_2 + 20 \text{ vol.}\% \text{ TZ-2Y}$

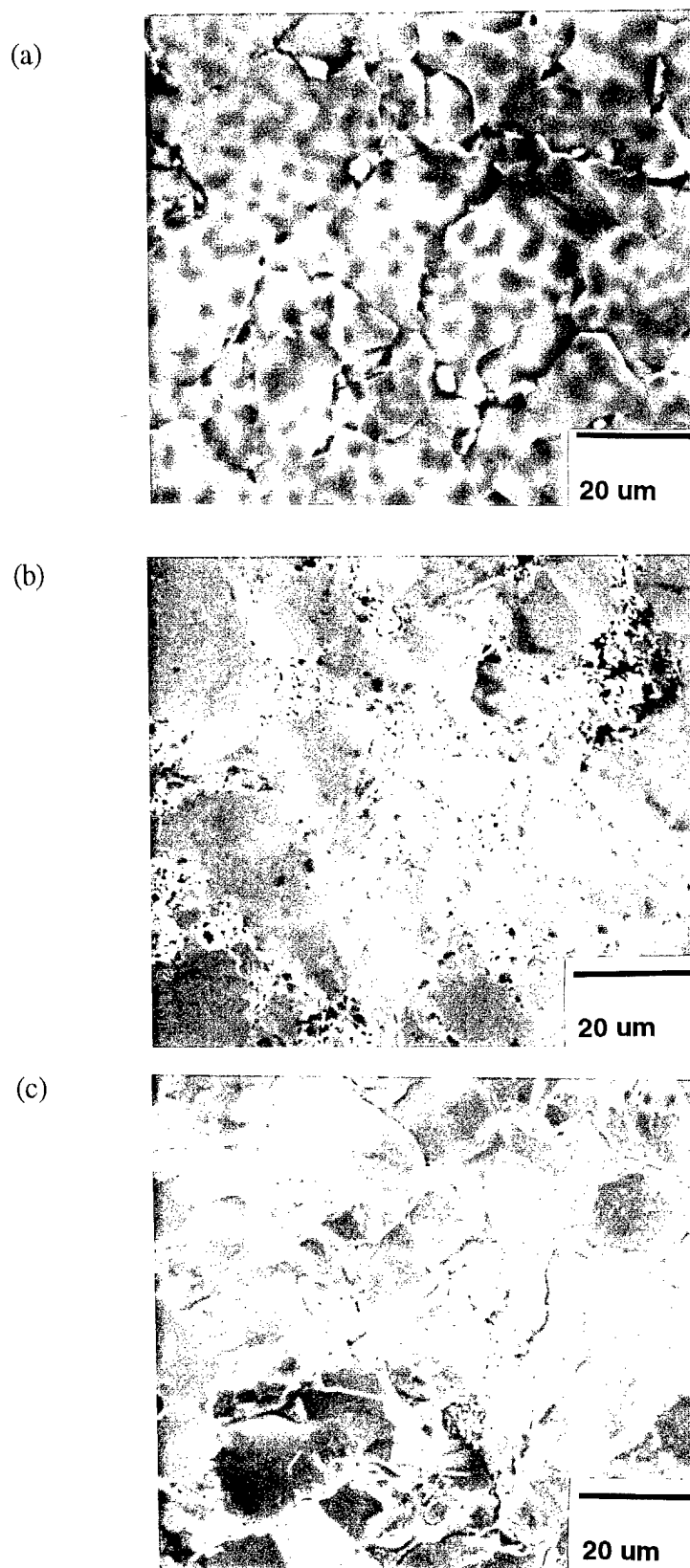


Figure 4.6 Fatigue Fracture Surface Morphologies of MoSi_2 and Brittle Reinforced MoSi_2 Composites at 1200 °C

(a) MoSi_2 ; (b) $\text{MoSi}_2 + 20 \text{ vol.}\% \text{ SiC}_w$, and (c) $\text{MoSi}_2 + 20 \text{ vol.}\% \text{ TZ-2Y}$

4.3.5 Crack-Tip Deformation Mechanisms

The deformed microstructure of MoSi_2 and its composites are shown on Figures 4.7a-4.7f. The dislocation densities in the crack-tip TEM foils were consistently higher than those in the undeformed materials that were heat treated to simulate the effects of thermal exposure at 1200°C . Dislocation networks structures were formed in the of MoSi_2 and MoSi_2 composites. Most of the deformation was concentrated within the MoSi_2 matrix, and there was some evidence of slip occurring from the interfaces between the boundaries of MoSi_2 and reinforcement phases (Figures 4.7b and 4.7d). Some evidence of slip was also observed within the SiC whiskers (Figure 4.7c). However, no evidence of slip was observed in the TZ-2Y particles.

As discussed earlier, amorphous glass phase was observed in the monolithic MoSi_2 and the TZ-2Y composite (Figures 4.7a and 4.7e). No evidence of amorphous glass phase was observed in the SiC_w composite (Figures 4.7c and 4.7d). Cyclic crack-tip deformation in the monolithic MoSi_2 and the TZ-2Y composite was, therefore, affected by the presence of amorphous glass phase. Since the amorphous glass phase can exhibit time dependent flow at elevated-temperature [33,84,85], elevated-temperature fatigue crack growth in MoSi_2 can occur by a combination of creep and fatigue mechanisms, as suggested by Ramamurthy et al. [33,84,85].

4.4. Conclusions

The elevated-temperature fatigue and fracture behavior of MoSi_2 and brittle-reinforced MoSi_2 composites (MoSi_2+20 vol. % SiC_w and MoSi_2+20 vol. % TZ-2Y) has been studied at 1200°C . The following conclusions have been reached based on the results of careful experimental studies of crack-tip deformation mechanisms and fracture modes:

1. The fracture toughness values of MoSi_2 and the composite at elevated-temperature (1200°C) in air examined in this study are significantly (40-70%) lower than the room-temperature fracture toughness values. The reduction in fracture toughness is greatest in monolithic MoSi_2 and the TZ-2Y composite in which amorphous glass phases are formed at the boundaries of the MoSi_2 grains after annealing at 1200°C .
2. Fracture of MoSi_2 occurs predominantly by a relatively flat cleavage mode and some incidence of intergranular fracture under monotonic and cyclic loading conditions. Rougher fracture modes are generally observed within the reinforcement phases distributed along the grain boundaries of the MoSi_2 grains. Evidence of pull-out or viscous flow of grain boundary glass phases is also apparent on the fracture surfaces of monolithic MoSi_2 and TZ-2Y composite.

3. Stable creep-fatigue crack growth occurs at 1200°C in all the materials that were examined in this study. It occurs within a narrow range of ΔK values between ~ 0.9 and $1.4 \text{ MPa}\sqrt{\text{m}}$. However, the crack growth rates are very fast when compared to those in the other brittle materials. Typical Paris experiment constants, m and C are respectively between approx. 32 and 156, and between 1.8×10^{-10} and $9.1 \times 10^{-8} (\text{mm/cycle})(\text{MPa}\sqrt{\text{m}})^{-m}$ during fatigue crack growth at 1200°C.

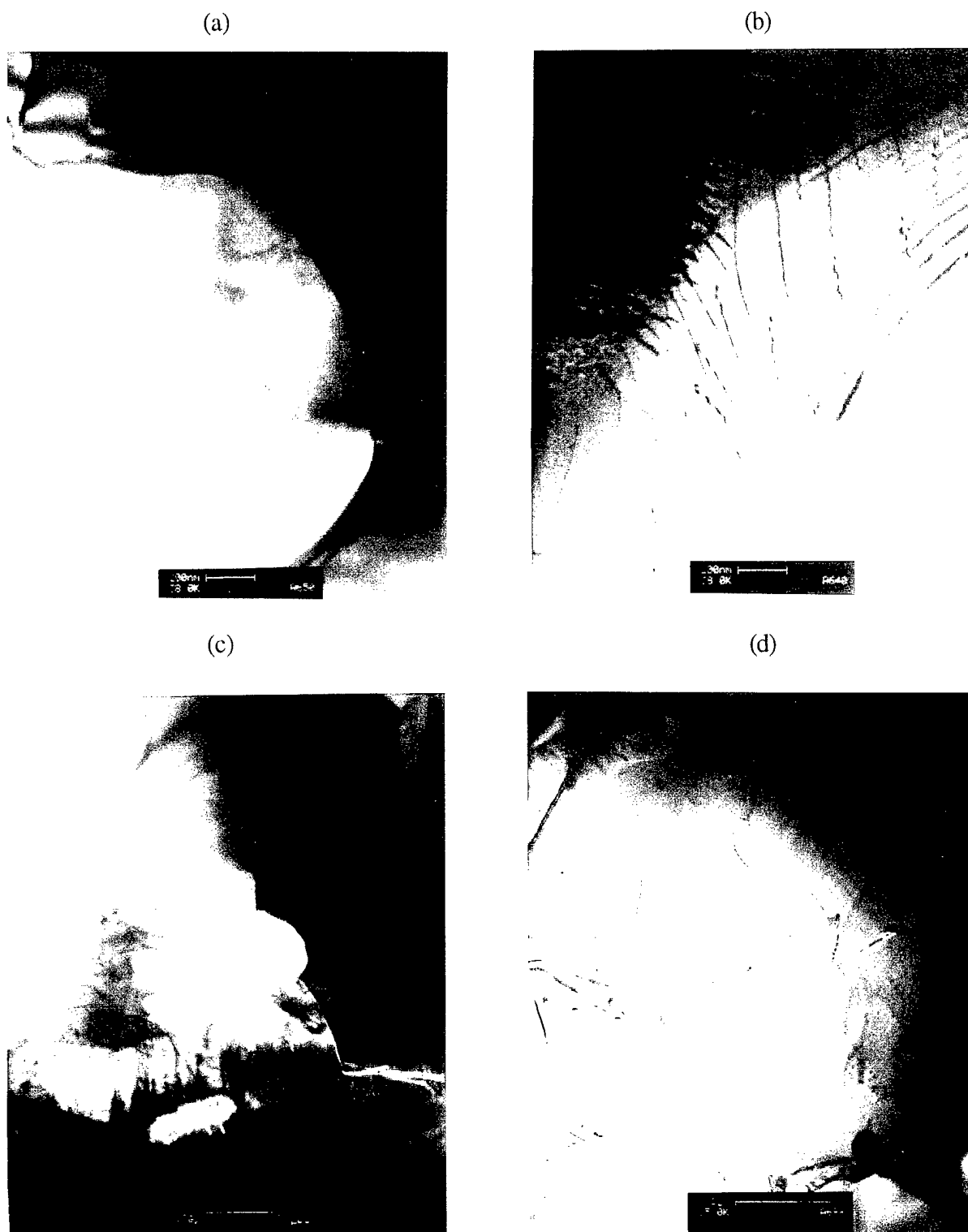


Figure 4.7 Typical TEM Images of Crack Tip Regions of MoSi_2 and Brittle Reinforced MoSi_2 Composites Deformed Under Cyclic Loading at 1200 °C
 (a) MoSi_2 ; (b) MoSi_2 ; (c) MoSi_2 + 20 vol.% SiC_w ; (d) MoSi_2 + 20 vol.% SiC_w ;

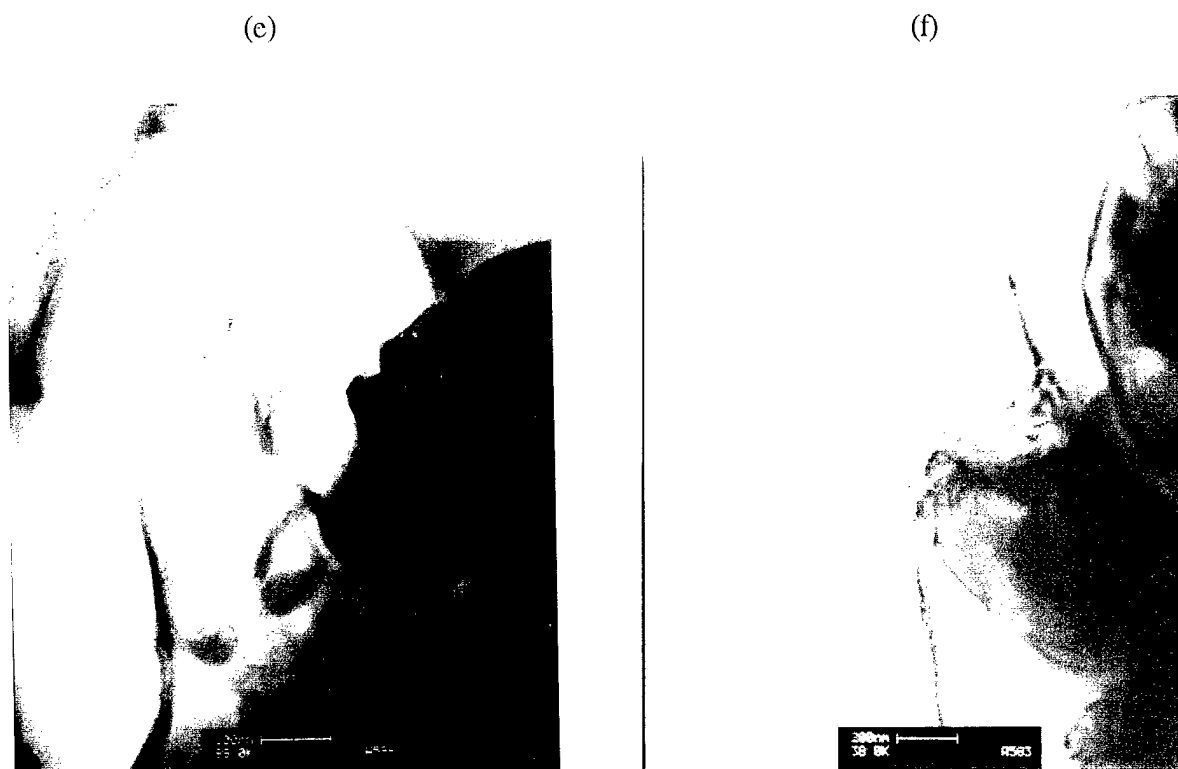


Figure 4.7 Typical TEM Images of Crack Tip Regions of MoSi₂ and Brittle Reinforced MoSi₂ Composites Deformed Under Cyclic Loading at 1200 °C
(e) MoSi₂ + 20 vol.%TZ-2Y, and (f) MoSi₂ + 20 vol.%TZ-2Y;

5. References

1. V.D. Krstic and A.K. Khaund: in *Advances in Fracture Research, Proc. Fifth Int. Conf. of Fracture*, D. Francois, C. Bathias, and B. Bilby, eds., Pergamon Press, Oxford, 1980, pp. 1577-85.
2. V.D. Krstic, P.S. Nicholson, and R.G. Hoagland: *J. Am. Ceram. Soc.*, 1981, vol. 64, pp. 499-504.
3. V.D. Krstic: *Phil. Mag.*, 1983, vol. 48, pp. 695-708.
4. D.E. Alman, K.G. Shaw, N.S. Stoloff and K. Rajan, *Mater. Sci. Eng.*, 1992, vol. A155, pp. 85-93.
5. C.K. Elliot, G.R. Odette, G.E. Lucas, and J.W. Sheckherd: in *High-Temperature/High-Performance Composites*, MRS Symp. Proc., F.D. Lemkey, A.G. Evans, S.G. Fishman, and J.R. Strife, eds., MRS, Pittsburg, PA, 1988, vol. 120, p. 95.
6. H.E. Dève, A.G. Evans, G.R. Odette, R. Mehrabian, M.L. Emiliani, and R.J. Hecht: *Acta Metall. Mater.*, 1990, vol. 38, p. 1491.
7. G.R. Odette, H.E. Dève, C.K. Elliot, A. Hasigowa, and G.E. Lucas: in *Interfaces in Ceramic Metal Composites*, R.J. Arsenault, R.Y. Lin., G.P. Martins, and S.G. Fishman, eds., TMS-AIME, Warrendale, PA, 1990, p. 443.
8. H.C. Cao, B.J. Dalgleish, H.E. Dève, C. Elliott, A.G. Evans, R. Mehrabian, and G.R. Odette: *Acta Metall.*, 1989, vol. 37, p. 2969.
9. T.C. Lu, A.G. Evans, R.J. Hecht, and R. Mehrabian: *Acta Metall. Mater.*, 1991, vol. 39, p. 1853.
10. B.D. Flinn, M. Ruhle, and A.G. Evans: *Acta Metall.*, 1989, vol. 37, p. 3001.
11. V.V. Krstic and D.S. Nicholson: *J. Am. Ceram. Soc.*, 1981, vol. 64, p. 499.
12. D. Brooks, R.J. Lederich and W.O. Soboyejo, An Investigation of The Effects of Brittle and Ductile Reinforcement on The Fatigue and Fracture Behavior of Molybdenum Disilicide Composites, *Proceedings of The Symposium on the Fatigue and Fracture of Ordered Intermetallic Materials*, W.O. Soboyejo, T.S. Srivatsan and D.L. Davidson, eds., TMS, Warrendale, PA, 1994, pp. 55-74.
13. L-C. Chen, D. Brooks, R.J. Lederich and W.O. Soboyejo, Ductile Phase Toughening of MoSi₂: Effects of Reinforcement Morphology, *Proceedings of The Symposium on Intermetallic Composites III*, J.A. Graves, D.B. Miracle and R.R. Bowman, eds., MRS, Pittsburgh, PA, 1994, vol. 350, pp. 183-188.
14. M. Mendiratta, J. J. Lewandowski and D. M. Dimiduk, *Metall. Trans.*, 1991, pp. 1573-1583.
15. H. Dève and M.J. Maloney: *Acta Metall. Mater.*, 1991, vol. 39, pp. 2275-84.
16. L. Shaw and R. Abbaschian, *Acta Metall. Mater.*, 1994, vol. 42, pp. 213-223.
17. L. Xiao and R. Abbaschian, *Metall. Trans.*, 1992, vol. 24A, p. 403.
18. E. Smith, *Int. J. Fract.*, 1989, vol. 40, pp. R27-R30.
19. K.T. Venkateswara Rao, G.R. Odette, and R.O. Ritchie: in *Fatigue of Advanced Materials*, R.O. Ritchie, R.H. Dauskardt, and B.N. Cox, eds., Materials and Component Engineering Publications Ltd., Birmingham, United Kingdom, 1991, pp. 429-37.
20. M. Maloney and R. Hecht: *Mater. Sci. Eng.*, 1991, vol. A155, pp. 19-31.
21. W.O. Soboyejo and S.M.L. Sastry: *Mater. Sci. Eng.*, 1992, vol. A171, pp. 95-104.
22. K.T. Venkateswara-Rao, W.O. Soboyejo and R.O. Ritchie, *Metall. Trans.*, 1992, vol. 23A, pp. 2249-2257.
23. J. Kajuch, J. D. Rigney and J. J. Lewandowski, *Mater. Sci. Eng.*, 1992, vol. A155, pp. 59-65.
24. W.O. Soboyejo, K.T. Venkateswara-Rao, S.M.L. Sastry and R.O. Ritchie, *Metall. Trans.*, 1993, vol. 24A, pp. 585-600.
25. D.E. Alman and N.S. Stoloff, *Metall. Mater. Trans.*, 1995, vol. 26A, pp. 289-303.
26. *Metals Handbook*, 10th Edition, ASM INTERNATIONAL, Metals Park, 1990, Vol. 2.

27. B. Budiansky, J.C. Amazigo, and A.G. Evans: *J. Mech. Phys. Solids*, 1988, vol. 36, pp. 167-88.
28. R.M. McMeeking and A.G. Evans: *Mech. Mater.*, vol. 9, pp. 217-27.
29. K.S. Chan, *Metall. Trans.*, 1992, vol. 23A, pp. 183-199.
30. W.O. Soboyejo, *Metall. Trans.*, 1992, vol. 23A, pp. 1737-1750.
31. K.T. Faber and A.G. Evans: *Acta Metall.*, 1982, vol. 31, pp. 565-76.
32. M.F. Ashby, F.J. Blunt and M. Bannister: *Acta Metall.*, 1989, vol. 37, p. 1847.
33. U. Ramamurthy, A.S. Kim, S. Suresh and J.J. Petrovic, *J. Am. Ceram. Soc.*, 1993, vol. 76, pp. 1953-1964.
34. R.O. Ritchie: *Int. Met. Rev.*, 1979, vol. 20, pp. 205-30.
35. R.H. Dauskardt and R.O. Ritchie: *Closed Loop*, 1989, vol. 27, pp. 7-17.
36. R.H. Dauskardt, D.B. Marshall, and R.O. Ritchie: *J. Am. Ceram. Soc.*, 1990, vol. 73, pp. 893-903.
37. L. X. Han and S. Suresh, *J. Am. Ceram. Soc.*, 1989, vol. 72, pp. 1233-1238.
38. M. J. Reece, F. Guiu and M. F. R. Sammur, 1989, *J. Am. Ceram. Soc.*, vol. 72, pp. 348-352.
39. A.K. Vasudāvan and J.J. Petrovic, "A Comparative Overview of Molybdenum Disilicide Composites" *Mater. Sci. Eng.*, A155, 1-17 (1992).
40. E. Fitzner and W. Remmele, "Possibilities and Limits of Metal Reinforced Refractory Silicides, Especially Molybdenum Disilicide," ICCM, Proc. Int. Conf. Comps. Mater., 5, 515-30 (1985).
41. P.J. Meschter, "Low-Temperature Oxidation of Molybdenum Disilicide," *Metall. Trans.*, A23 (1992) 1763-72.
42. D.A. Bertziss, R.R. Cerchiara, E.A. Gulbransen, F.S. Pettit and G.H. Merier, "Oxidation of MoSi₂ and Comparison with Other Silicide Materials," *Mater. Sci. Eng.*, A155 (1992) 165-81.
43. W.O. Soboyejo, F. Ye, , L.C. Chen, N. Bahtishi, D.S. Schwartz and R.J. Lederich, "Effects of Reinforcement Morphology on the Fatigue and Fracture Behavior of MoSi₂/Nb Composites," *Acta Metall. et Mater.* 44 [5] 2027-41 (1996).
44. D. H. Carter and G. F. Hurley, *J. Am. Ceram. Soc.*, 1987, vol. 70, pp. 79-81.
45. D. H. Carter, J. J. Petrovic, R. E. Honnell and W. S. Gibbs, *Ceram. Eng. Sci. Proc.*, 1989, Vol. 10, pp. 1121-1129.
46. C. L. Hom, P. A. Mataga and R. M. McMeeking, *Int. J. Num. Meth. Eng.*, 1989, vol. 27, pp. 233-255.
47. J. J. Petrovic and R. E. Honnell, *J. Mater. Sci.*, 1990, pp. 4453-4456.
48. J. J. Petrovic, R. E. Honnell and T. E. Mitchell, *J. Mater. Sci.*, 1991, vol. 12, pp. 1633-1642.
49. W. O. Soboyejo, D. Brooks, L. C. Chen and R. Lederich, "Transformation Toughening and Fracture Behavior of Molybdenum Disilicide Composites Reinforced with Partially Stabilized Zirconia," *J. Am. Ceram. Soc.*, , Vol. 78, pp. 1481-1488, 1995.
50. D. B. Marshall, M. C. Shaw, R. H. Dauskardt and R. O. Ritchie, *J. Am. Ceram. Soc.*, 1990, vol. 73, pp. 2659-2666.
51. D. B. Marshall, A. G. Evans and M. Drory, "Transformation Toughening of Ceramics," *Fracture Mechanics of Ceramics*, pp. 289-307, Vol. 6, R.C. Bradt, A.G. Evans, D.P.H. Hasselman and F.F. Lange, eds., Plenum Press, New York, NY, (1983).
52. P. F. Becher, *Acta Metall.*, 1986, vol. 34, pp. 1885-1891.
53. A. G. Evans and R. M. Cannon, *Acta Metall.*, 1986, vol. 34, pp. 761-800.
54. J. C. Lambropoulos, *Int. J. Solids Structures*, 1986, vol. 22, pp. 1083-1106.
55. R. M. McMeeking and A. G. Evans, *J. Am. Ceram. Soc.*, 1982, vol. 65, pp. 242-246.
56. B. Budiansky, J. W. Hutchinson and J. C. Lambropoulos, *Int. J. Solids Structure*, 1983, vol. 19, pp. 337-355.
57. B. Budiansky and L. Truskinovski, *J. Mech. Phys. Solids*, 1993, vol. 41, pp. 1445-1459.
58. N. Claussen and M. Rühle, "Design of Transformation-Toughened Ceramics," *Advances in Ceramics*, pp. 137-163, Vol. 3, A.H. Heuer and L.W. Hobbs, eds., Am. Ceram. Soc., Columbus, OH, (1982).

59. G. Stam, A Micromechanical Approach to Transformation Toughening in Ceramics, Ph.D. Thesis, Delft University of Technology, Faculty of Mechanical Engineering and Marine Technology, Netherlands, 1994.
60. F. F. Lange, *J. Mater. Sci.*, 1982, vol. 17, pp. 225-234.
61. A.G. Evans and A.H. Heuer, *J. Am. Ceram. Soc.*, 1980, vol. 63, p. 241.
62. I.W. Chen and P.E. Reyes Morel, *J. Am. Ceram. Soc.*, 1986, vol. 69, pp. 181-189.
63. I.W. Chen, *J. Am. Ceram. Soc.*, 1986, vol. 69, pp. 189-194.
64. P.E. Reyes Morel and I.W. Chen, *J. Am. Ceram. Soc.*, 1988, vol. 71, pp. 343-353.
65. J. Selsing, *J. Am. Ceram. Soc.*, 1961, vol. 44, p. 419.
66. M. He and A. G. Evans, *Acta Metall. Mater.*, 1994, vol. XX, pp. xx-yy.
67. Popov
68. B. C. Gravie and P. S. Nicholson, *J. Am. Ceram. Soc.*, 1972, vol. 55, pp. 303-305.
69. P. L. Porter and A. H. Heuer, *J. Am. Ceram. Soc.*, 1979, vol. 62, pp. 298-305.
70. J. Adams and B. Cox, *J. Nucl. Energy, Part A*, 1959, vol. 11, pp. 31-33.
71. P. A. Evans, R. Stevens and J. G. P. Binner, *Br. Ceram. Trans. J.*, 1984, vol. 83, pp. 39-43.
72. E. D. Whitney, *Trans. Faraday Soc.*, 1965, 61, p. 1191.
73. H. P. Klug and L. E. Alexander, *X-Ray Diffraction Procedures for Polycrystalline and Amorphous Materials*, John Wiley & Sons, Inc., 1954.
74. B. D. Cullity, "Elements of X-Ray Diffraction", Addison Wesley Publishing Company, Inc., 1978.
75. ASTM E-399-90 Code, "Standard Test Method for Plane Strain Fracture Toughness of Metallic Materials," *Annual Book of ASTM Standards*, ASTM, Philadelphia, PA. 1992, vol. 03.01, pp. 506-536.
76. W. O. Soboyejo and C. Mercer, *Scr. Metall. Mater.*, 1994, vol. 30, pp. 1515-1520.
77. S. Maloy, A. Heuer, J. J. Lewandowski and J. Petrovic, *J. Amer. Ceram. Soc.*, 1991, vol. 74, pp. 2704-2706.
78. M. Rühle, A. G. Evans, R. M. McMeeking, P. G. Charalambides and J. W. Hutchinson, *Acta Metall.*, 1987, vol. 35, pp. 2701-2710.
79. A. G. Evans and Y. Fu, *Acta Metall.*, 1985, vol. 33, pp. 1525-1531.
80. L. R. F. Rose, *Int. J. Fract.*, 1986, vol. 31, pp. 233-242.
81. R. Stevens, *Zirconia and Zirconia Ceramics*, Magnesium Elektron Ltd., Twickenham, UK, 1986.
82. A. Muller, G. Wang and R.A. Rapp, "Deposition and Cyclic Oxidation Behavior of a Protective (Mo,W)(Si,Ge)₂ Coating on Nb-Base Alloys," *J. Electrochem. Soc.*, 139 [5] 1266-75 (1992).
83. Gui-Ying Lu, R.J. Lederich and W.O. Soboyejo, "Residual Stresses and Transformation Toughening in MoSi₂ Composites Reinforced with Partially Stabilized Zirconia," *Mater. Sci. Eng.*, A210, (1996) 25-41.
84. U. Ramamurty, T. Hansson and S. Suresh, "High-Temperature Crack Growth in Monoclinic and SiC_w-Reinforced Silicon Nitride under Static Cyclic Loads," *J. Am. Ceram. Soc.*, 77 [11] 2985-95 (1994).
85. U. Ramamurty, S. Suresh and J.J. Petrovic, "The Effect of Carbon Addition on Elevated Temperature Crack Growth Resistance in (Mo, W) Si- SiC_p Composites," *J. Am. Ceram. Soc.*, 77 [10] 2681-90 (1994).
86. J. C. Amazigo and B. Budiansky, "Interaction of Particulate and Transformation Toughening," *J. Mech. Phys. Solids*, Vol. 36, 1988, pp. 581-595.
87. S. Suresh and J.R. Brockenbrough, *Acta Metall. Mater.* 1988, Vol. 36, pp.1444-1470.

6. PUBLICATIONS

1. W. O. Soboyejo, F. Ye, L-C. Chen, N. Bahtishi, D. S. Schwartz and R. J. Lederich, Investigation of The Effects of Reinforcement Architecture on The Fatigue and Fracture Behavior of MoSi₂/Nb Composites, *Acta Metallurgica et Materialia*, Vol. 44, pp. 2027-2041, 1996.
2. W. O. Soboyejo, F. Ye and D. S. Schwartz, Fatigue and Fracture Behavior of Nb Fiber-Reinforced Composites, *Metallurgical and Materials Transactions*, Vol. 26A, pp. 2263-2273.
3. G-Y. Lu and W. O. Soboyejo, Residual Stress and Transformation Toughening in MoSi₂ Composites Reinforced With Partially Stabilized Zirconia, *Materials Science and Engineering*, Vol. A210, pp. 25-41, 1996.
4. G-Y. Lu, R. J. Lederich and W. O. Soboyejo, Elevated-Temperature Fatigue Crack Growth in MoSi₂ and Brittle-Reinforced MoSi₂ Composites, *Journal of The American Ceramic Society*, 1996 (submitted).
5. G-Y. Lu, R. J. Lederich and W. O. Soboyejo, An Investigation of Residual Stress and Transformation Toughening in MoSi₂ Composites Reinforced With Partially Stabilized Zirconia, *Proceedings of The TMS Symposium on Processing and Fabrication of Advanced Materials*,
5. G-Y. Lu, R. J. Lederich and W. O. Soboyejo, Elevated-Temperature Fatigue Crack Growth in Brittle-Reinforced MoSi₂ Composites, *Proceedings of The Symposium on The Deformation and Fracture of Ordered Intermetallic Materials*, W. O. Soboyejo, T. S. Srivatsan and H. L. Fraser, Editors, pp. 507-539, 1996.
6. W. O. Soboyejo, F. Ye and D. S. Schwartz, An Investigation of Fatigue and Fracture in MoSi₂/Nb Fiber-Reinforced Composites, *Proceedings of ASME Materials Division, Symposium on Processing, Design and Performance of Composite Materials*, ASME, New York, NY, Vol.1, pp.661-694, 1995.
9. G-Y. Lu, R. J. Lederich and W. O. Soboyejo, Elevated-Temperature Fatigue Crack Growth in Brittle-Reinforced MoSi₂ Composites, *Proceedings of The Symposium on The Deformation and Fracture of Ordered Intermetallic Materials*, W. O. Soboyejo, T. S. Srivatsan and H. L. Fraser, Editors, pp. 395-430, 1996.
12. W. O. Soboyejo, F. Ye, L-C. Chen, N. Bahtishi, D. S. Schwartz and R. J. Lederich, Effects Ductile Phase Reinforcement Morphology on The Fatigue and Fracture Behavior of MoSi₂ Composites, *Symposium on The Fatigue and Fracture of Ordered Intermetallic Materials II*, W. O. Soboyejo, T. S. Srivatsan and R. O. Ritchie, Editors, TMS, Warrendale, PA, pp. 359-390. 1995

7. PRESENTATIONS (UNPUBLISHED)

1. G-Y. Lu, R. J. Lederich and W. O. Soboyejo, An Investigation of Residual Stress and Transformation Toughening in MoSi₂ Composites Reinforced With Partially Stabilized Zirconia, Presented at The TMS Symposium on Processing and Fabrication of Advanced Materials, TMS Fall Meeting, Cleveland, OH, October, 1995.
3. G-Y. Lu, F. Ye, R. J. Lederich and W. O. Soboyejo, Cyclic Crack Growth and Fracture of MoSi₂ Composites, Presented at The Symposium on The Fatigue and Reliability of Structural Ceramics and Composites, 98th Annual Meeting of The Ceramics Society, April, 1996.
4. W. O. Soboyejo, F. Ye, D. S. Schwartz and R. J. Lederich, Microstructure Design of Molybdenum Disilicide Composites, Presented at The 19th Annual Conference on Composites, Materials and Structures, Cocoa Beach, FL, January 9-10, 1995
5. W. O. Soboyejo, F. Ye and R. J. Lederich, Fatigue and Fracture of Laminated MoSi₂/Nb Composites, Presented at The Mechanical Behavior Symposium, 97 th Annual Meeting of The American Ceramic Society, Cincinnati, OH, April 30-May 3, 1995.
6. W. O. Soboyejo, F. Ye and R. J. Lederich, Fatigue and Fracture in a Layered MoSi₂/Nb Composite, Presented at The Symposium on Layered Materials, MRS Spring Meeting, San Francisco, CA, April 7-11, 1996.
7. G-Y. Lu, F. Ye, R. J. Lederich and W. O. Soboyejo, Cyclic Crack Growth and Fracture of MoSi₂ Composites, Symposium on The Fatigue and Reliability of Structural Ceramics and Composites, 98th Annual Meeting of The Ceramics Society, April 14-17, 1996.
8. F. Ye, G-Y. Lu, P. Ramasundaram and W.O. Soboyejo, Micromechanisms of Crack-tip Deformation in Zirconia Toughened Intermetallics, Presented the 126th TMS Annual Meeting, Orlando, FL, February 9-13, 1997.
9. F. Ye, Y. Li, R.J. Lederich and W.O. Soboyejo, "Micromechanisms of Fatigue Crack Growth in MoSi₂-Based Composites", Presented on the 1997 Materials Week, TMS Fall Meeting, Indianapolis, Sept. 14-18, 1997.

8. HONORS

1. W.O. Soboyejo received The Lumky Research Award of The College of Engineering of The Ohio State University. The Award is given in recognition of exceptional research accomplishments to Professors in the College of Engineering at The Ohio State University.
2. W.O. Soboyejo received The National Young Investigator Award from The Division of Materials Research of The National Science Foundation in 1994.
3. W.O. Soboyejo received the Young Investigator Award from The Division of Materials Research of The Office of Naval Research in 1994.

